

# Synthesis and Characterization of Multidimensional Co and Fe based Ferromagnetic Nanostructures



Submitted by

**Suleman Khan**

**PhD Thesis**

(24-FBAS/PHDPHY/F13)

Supervised by

**Dr. Naeem Ahmad**

Assistant Professor

**Department of Physics**

**Faculty of Basic and Applied Sciences**

**International Islamic University**

**Islamabad**

Co-Supervised by

**Dr. Javed Iqbal**

Associate Professor

**Department of Physics**

**Quaid-i-Azam University**

**Islamabad**



2019

Accession No 71423364

PhD  
620.5  
SUS



I Nanostructured materials

II Nanoscience

III Microphysics

**Synthesis and Characterization of Multidimensional Co and Fe based  
Ferromagnetic Nanostructures**

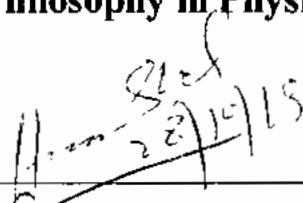
By

**Suleman Khan**  
24-FBAS/PHDPHY/F13

This thesis is submitted to the Department of Physics, International Islamic  
University Islamabad

For the award of degree of

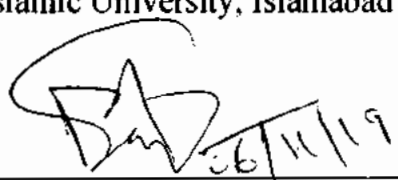
**Doctor of Philosophy in Physics**

  
Handwritten signature and date: 28/11/15

---

Chairman, Department of Physics

International Islamic University, Islamabad

  
Handwritten signature and date: 26/11/19

---

Dean, Faculty of Basic and Applied Sciences,

International Islamic University, Islamabad

**Department of Physics**  
**Faculty of Basic and Applied Sciences**  
**International Islamic University, Islamabad**

**(2019)**

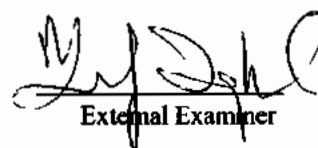
Date: Sep12, 2019

## FINAL APPROVAL

It is certified that the work presented in this thesis entitled "Synthesis and Characterization of Multidimensional Co and Fe based Ferromagnetic Nanostructures" by Suleman Khan, Registration No. 24-FBAS/PHDPHY/F13 is of sufficient standard in scope and quality for award of degree of PhD Physics from the Department of Physics, International Islamic University, Islamabad, Pakistan.

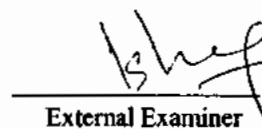
## COMMITTEE

**Prof. Dr. Zafar Iqbal**  
Head of the Department of Physics  
Riphah International University  
Islamabad



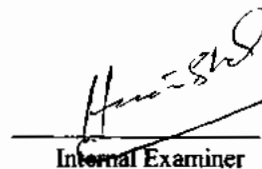
External Examiner

**Dr. Ishaq Ahmad**  
Director (Accelerator)  
National Center for Physics (NCP)  
Islamabad



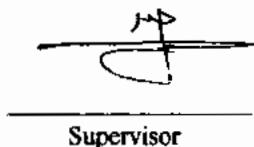
External Examiner

**Dr. Wiqar Hussain Shah**  
Associate Professor  
Department of Physics  
International Islamic University,  
Islamabad



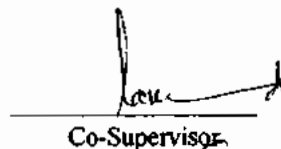
Internal Examiner

**Dr. Naeem Ahmad**  
Assistant Professor  
Department of Physics  
International Islamic University,  
Islamabad



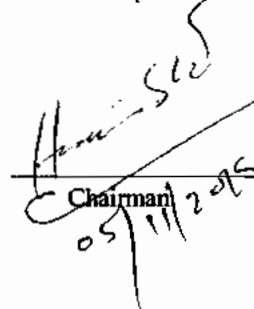
Supervisor

**Dr. Javed Iqbal**  
Associate Professor  
Department of Physics  
Quaid-i-Azam University,  
Islamabad



Co-Supervisor

**Dr. Wiqar Hussain Shah**  
Associate Professor  
Department of Physics  
International Islamic University, Islamabad

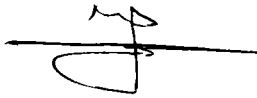


Chairman  
05/11/2019

Date: Sep12, 2019

**Certificate**

The thesis entitled “**Synthesis and Characterization of Multidimensional Co and Fe based Ferromagnetic Nanostructures**” submitted by **Suleman Khan** (Registration # 24-FBAS/PHDPHY/F13) in partial fulfilment of PhD degree in Physics has been completed under my guidance and supervision. I am satisfied with the quality of his research work and allow him to submit this thesis for further process to graduate with Doctor of Philosophy degree from Department of Physics, as per IIUI rules and regulations



**Supervisor**

Dr. Naeem Ahmad  
Assistant Professor  
Department of Physics  
International Islamic University  
Islamabad




**Co-Supervisor**

Dr. Javed Iqbal  
Associate Professor  
Department of Physics  
Quaid-i-Azam University  
Islamabad

## Declaration of Originality

I hereby declare and affirm that this thesis “**Synthesis and Characterization of Multidimensional Co and Fe based Ferromagnetic Nanostructures**” neither as a part nor as whole, has been copied out from any source. It is further declared that I have completed this thesis entirely on the basis of my personal effort, made under the sincere guidance of my supervisors **Dr. Naeem Ahmad**. If any part of this report is proven to be copied or found to be a reproduction of some other, I shall stand by the consequences. No portion of the work presented in this report has been submitted in support of an application for other degree or qualification of this or any other university or institute of learning. If any part of this project is proved to be copied from any source or found to be reproduction of some other project, I (Mr. Suleman Khan) shall be legally responsible for punishment under the plagiarism rules of Higher Education Commission (HEC), Pakistan. The plagiarism test has been carried out using Turnitin via ID: **1104391289**. The similarity index lies in permissible range.



Suleman Khan

24-FBAS/PHDPHY/F13

Dated: 12-9-2019



*Dedicated*  
*To*  
*My Beloved*  
*Parents and My*  
*Uncle M. Kabut Khan*  
*(Late)*



## Acknowledgement

All Praises to Allah Almighty, the Sustainer of the whole universe. He makes Laws for the evaluations of things and sets them on the path of perfection. Allah Almighty who bestows and blesses knowledge, technology and scientific ingenuity to man through experimental research and remarkable deduction to ponder over the forces of nature. First, I express my utmost thanks to Allah Almighty the omnipresent and creator of universe. He gave me strength to complete this thesis. I offer my best gratitude to the last Prophet Hazrat Muhammad (S.A.W.W). The messenger of Allah Almighty, given the lesson of altruism, seeking knowledge

The successful completion of this dissertation involved continuous support and feedback of several individuals, and it is my pleasure to thank all of them. I consider myself to be very fortunate to get the chance of working under **Dr. Naeem Ahmed** supervision. The moment of working under his brilliant supervision that was really pleasurable, his dedicated and tenacious effects are appreciable. I enjoyed the trust, confidence and liberty that he provides me during the whole research process. His unconditional kindness, patience and guidance with precious knowledge have always amazed me. Beside, my co-supervisor **Dr. Javed Iqbal** (Department of Physics, Quaid-i-Azam University, Islamabad, Pakistan) enlightened my vision deepening the direction for achieving the task.

A very special thanks to the Chairman Department of Physics IIUI, **Dr. Wiqar Hussain Shah**, who is undaunted and easing protection made it possible to work successfully in safe, sound and unmatched environment for the research students.

Moreover, I would like to express my sincere thanks to **all the faculty members, Department of Physics IIU Islamabad**, whose admirable cooperation and coordination supported me a lot. Moreover, I would like to express my sincere thanks to **Prof. Dr. Zafar Iqbal** (HOD Physics; Riphah International University, Islamabad) and **Dr. Ishaq Ahmad** (Director; Accelerator NCP, Islamabad) for valuable discussion. I shall express my heartiest thanks to **Dr. Ather Hassan** (Assistant Professor AIQUI) and **Prof. Dr. Syed Zafar Ilyas** (Chairman and Dean F/O Sciences AIQUI) for their moral support as well as for providing the characterization facilities. I would also like to acknowledge Prof. **Dr. Xiufeng Han** at Institute

of Physics, University of Chinese Academy of Sciences, China and **Mr. Kifayat Niazi**, MS student at Xi'an Jiaotong University, China who provide me a platform for characterization. I can't forget to thank **Dr. Nisar Ahmed** (Assistant Professor in Department of Physics and applied Mathematics PIEAS) for providing the tools of Density functional Theory (DFT).

I shall express my heartiest thanks to all of my research colleagues; Muhammad Jamil, Mohammad Asim, Mohammad Kashif, Abdul Wahab, Shahid Khan, Adnan Gulab, Muhammad Miraj, Mohammad Afzal, Tahzin Kanwal. I cannot forget to thank my friend Mr. Imran Ullah Khan for providing help in English grammatical support.

Special acknowledgement goes to some lab mates; Mr. Affan Safeer, Mr. Liaqat Ali Azam, Danyal Bashir and Abdul Qadir for their best cooperation, great help and support and their pleasant, enjoyable company made the research easier.

I extend heartiest gratitude to my beloved parents and all my family members for their tremendous support. You all were the pillars of my strength during this long journey of PhD. I wouldn't make it without your understanding.

Experimental work always demands the help of many people. I want to say thanks to all those who helped me in one way or other, and I forgot to mention them here.

**Suleman Khan**  
**24-FBAS/PHDPHY/F13**

## List of Publications

1. **Suleman khan**, Naeem Ahmad, Nisar Ahmed, X.F. Han “Analysis of Electronic, Magnetic and Half-Metallic Properties of  $L2_1$ -type ( $\text{Co}_2\text{Mn}_{0.5}\text{Fe}_{0.5}\text{Sn}$ ) Heusler alloy Nanowires synthesized by AC-electrodeposition in AAO templates” *J. Magn. Magn. Mater*, **460** 120–127(2018). **I.F : 3.06**
2. **Suleman Khan**, Naeem Ahmad, Nisar Ahmed, Affan Safeer, Javed Iqbal, X.F. Han “Structural, Magnetic and Transport Properties of Fe-based Full Heusler alloy  $\text{Fe}_2\text{CoSn}$  Nanowires Prepared by Template-based Electrodeposition” *J. Magn. Magn. Mater*, **465**, 462–470 (2018). **I.F: 3.06**
3. **Suleman Khan**, Naeem Ahmad, Affan Safeer, Javed Iqbal “Compositional dependent morphology, structural and magnetic properties of  $\text{Fe}_{100-x}\text{Cu}_x$  alloy nanowires via electrodeposition in AAO templates”.*Appl. Phys. A*.**124**, 678 (2018). **I.F : 1.67**
4. **Suleman Khan**, Naeem Ahmad, Affan Safeer, Javed Iqbal “Magnetic, Electronic and Structural investigations of  $\text{Fe}_{1-x}\text{Mn}_x$  ( $0.01 \leq x \leq 0.04$ ) alloy nanowires via electrodeposition in AAO templates. *Manuscript under-review* in *Material Research Express*” **I.F : 1.47**
5. Affan Safeer, Naeem Ahmad, **Suleman Khan**, Liaqat Ali Azam, Danyal Bashir, “Magnetization Behavior of Electrochemically Synthesized  $\text{Co}_2\text{MnSn}$  full Heusler alloy Nanowire Arrays.” *J. Appl. Phys*, **115**, (2019) **I.F: 2.1**
6. Naeem Ahmad, Abdul Majid, Saira Parveen, Wiqar Hussain Shah, Faryal Mughal, Suleman Khan, Imran Murtaza “Structural and Uniaxial Magnetic Anisotropy of  $\text{Co}_{1-x}\text{Mg}_x$  ( $X = 0.04-0.12$ ) Nanowires in Alumina Templates”, *J. Supercond Nov Magn*. **30**,469–473 (2019). **I.F: 1.1**
7. Muhammad Awais, Naeem Ahmad, **Suleman khan**, Affan safeer, Khalid Javed, Imran Murtaza, Abdul Majid, “Voltage Dependent Physical, Dielectric and Magnetic Properties of Electrodeposited  $\text{Co}_{1-x}\text{Mn}_x$  Alloy Nanowires.” *J. Magn. Magn. Mater*, **474**, 207–214 (2018) **I.F : 3.06**
8. Naeem Ahmad, Fahad Hassan, **Suleman Khan**, Abdul Majid, Affan Safeer, Ahmad Saeed, Imran Murtaza, S. Ahmed, X.F. Han “Mobility and perpendicular magnetic anisotropy in electrodeposited  $\text{Co}_{32}\text{Fe}_{67}\text{B}_1$  thin films using boric acid as boron source” *J. Magn. Magn. Mater*, **458**, 156–163 (2018). **I.F: 3.06**

9. Naeem Ahmad, Tian Yu, **Suleman Khan**, Abdul Majid, Javed Iqbal, Saqlain A. Shah, S. U. Awan, X. F. Han "Ferromagnetic Relaxation and Magnetic Properties of  $\text{Co}_{40}\text{Fe}_{40}\text{B}_{20}$  Thin Films", *J. Supercond Nov Magn.* **30**,469–473 (2017). **I.F: 1.14**
10. Naeem Ahmad, Sajid Tanweer · **Suleman Khan**, Javed Iqbal, Abdul Majid, Saqlain A. Shah· M. S. Awan, Muhammad Moazzam Naseer, "Magnetization Reversal and Surface Spins in Electrodeposited  $\text{Co}_{90}\text{Mn}_{10}$  Alloy Nanowires" *J Supercond Nov Magn*, **30**, 505-509 (2017). **I.F : 1.14**
11. Naeem Ahmad, **Suleman khan**, M. Arman liaqat, Muhammad Awais, Saqlain A. Shah Ishfaq Ahmed, Nyla Jabeen , Abdul Majid, Javed Iqbal, "Influence of voltage variation on structure and magnetic properties of  $\text{Co}_{1-x}\text{Sn}_x$  ( $x$  5 0.3–0.7) nanowire alloys in alumina by electrochemical deposition", *Appl. Phys. A.* **123**:65(2017). **I.F : 1.67**
12. Naeem Ahmad, **Suleman Khan**, W. J. Li, Muhammad Siddique , Saqlain A. Shah, Javed Iqbal, Abdul Majid, X. F. Han "Potential dependent Tuning of magnetic and structural properties of electrodeposited NiZn nanowires in  $\text{Al}_2\text{O}_3$  templates" *J. Magn. Magn. Mater*, **441**, 696-701 (2017). **I.F : 3.06**
13. Naeem Ahmad, Ahmad Saeed , **Suleman Khan** , Fahad Hassan, W.J. Li, Saqlain A. Shah, Abdul Majid, X.F. Han, "Investigation of easy axis transition and magnetodynamics in  $\text{Ni}_{76}\text{Fe}_{24}$  nanowires and  $\text{Ni}_{77}\text{Fe}_{23}$  nanotubes synthesized by DC electrodeposition " *J Alloys Compd*, **725**,123-128 (2017). **I.F: 3.77**
14. Naeem Ahmad, Amna Jaral, Gulbahar Bano, Sidrah Batool, Hira Dilpazir, Muhammad Jameel **Suleman Khan**, Javed Iqbal, Abdul Majid, Muhammad Moazzam Naseer, Saqlain A. Shah, "AC Potential-Dependent Concentration Variation and Domain Wall Pinning in  $\text{Co}_{1-x}\text{Zn}_x$  ( $x = 0.4 - 0.5$ ) Nanorods", *J Supercond Nov Magn*, **29**, 509–513 (2016). **I.F : 1.14**
15. Affan Safeer, Liaqat Ali Azam, Danyal Bashir, **Suleman Khan**, Naeem Ahmad\* "Effect of Mn (12 at%) Substitution on Magnetic Anisotropy and Magnetization Reversal of Equiatomic CoFe Alloy Nanorod arrays" *Manuscript under-review in Physica B* (**I.F. 1.8**)

# Table of Contents

Abstract.....	1
<b>Chapter No. 1</b> .....	<b>5</b>
<b>Introduction</b> .....	<b>6</b>
1.1. Introduction to Nano .....	6
1.2. Factors Affect during Anodization of Aluminum .....	7
1.2.1. Various Shape of Different Materials Synthesized from AAO Templates.....	8
1.2.2. Some Fundamental Features of Anodic Porous Alumina .....	9
1.2.3. Applications of Porous Aluminum Oxide Templates .....	9
1.2.4. Importance of Template-based NWs via Different Deposition Technique.....	10
1.3. Brief Survey of Nanowires Applications .....	10
1.3.1. Biomedical Applications of Magnetic Nanowires .....	11
1.3.2. Use of Single and Multi-functional Magnetic Nanowires in the Field of Biomedicines .....	11
1.3.2.1. Biomolecular Manipulation .....	12
1.4. Spintronics .....	13
1.5 Nanotechnology Based on Nanowires in the Present and Future Prospectus .....	14
1.5.2. Use of Multi-layer NWs in Diverse Areas of Nanotechnology .....	16
1.6. Present Research on Electronic Devices based on Magnetic Nanowires.....	16
1.7. History of Heusler Alloys .....	17
1.7.1. Structural Properties of Heusler Alloys .....	18
1.7.2. Half-Metallic Ferromagnetism.....	19
1.7.3. Origin of the Band Gap in Heusler Alloys.....	20
1.8. Factors Affecting on Disrupting Half-Metallic Ferromagnetism.....	21
1.8.1. Structural Disorders .....	21
1.8.2. Temperature Effect .....	22
1.9. Magnetic Properties of Full Heusler Alloys.....	22
1.9.1. Slater-Pauling Rule .....	23
1.9.2 Magnetocrystalline Anisotropy .....	24
1.9.3 Shape anisotropy .....	24
1.9.4 Magnetic Anisotropy in Nanowire Arrays.....	25
1.10. Density Functional Theory.....	25
1.11. Motivation of the Thesis .....	27
<b>Chapter No. 2</b> .....	<b>30</b>
<b>Literature Review</b> .....	<b>31</b>
2.1. Anodic Aluminum Oxide (AAO) Templates.....	31

2.1.1 Basic Stages for the Two Steps of Anodization.....	31
2.1.2. Three-Steps of Anodization .....	31
2.2.1. Patermarakis and Colleagues Proposed the Growth Models of AAO Templates:.....	32
2.3. Synthesis of Nanowires (NWs).....	33
2.3.1. Single Component NWs.....	33
2.3.2. Binary Alloys NWs.....	34
2.4. Heusler Alloy.....	34
2.4.1. Cobalt-Based Full Heusler alloy Nanostructures.....	34
<b>Chapter No. 3 .....</b>	<b>36</b>
<b>Synthesis Techniques.....</b>	<b>37</b>
3.1. Effect of Applied Conditions on Geometry of Anodized Aluminum Oxide (AAO) Templates ...	37
3.1.1. Pore Diameter of AAO Templates.....	38
3.1.2. Interpore Distance of AAO Templates .....	39
3.1.3. The Wall Thickness of AAO Templates.....	40
3.1.4. Thickness of the Barrier Layer of AAO Templates .....	40
3.1.5. Porosity .....	40
3.1.6. The Pore Density of AAO Templates'.....	41
3.2. Pre-Treatment of Aluminum Foil before to Start Anodization Process.....	41
3.2.1. Pre-Treatment of Aluminum Foil .....	41
3.2.2. Heat (Annealing) treatment.....	42
3.2.3. Degreasing of the Aluminum Foil .....	42
3.2.4. Electrochemical Polishing of the Surface of Aluminum Foil .....	42
3.3. Brief Survey to Synthesize AAO Templates using Two Steps of Anodization Technique .....	42
3.3.1. First step of anodization.....	42
3.3.2. Heat Treatment.....	43
3.3.3. Second step of anodization.....	43
3.4. Factors Determining the Morphology of PAA Structures .....	44
3.5. Removal of the Aluminum Base.....	45
3.5.1. Extraction of the Barrier Layer and Pore Widening .....	45
3.6. Anodization and Potential/Current-Time Transient.....	46
3.6.1 Current-Time Graph.....	47
3.6.2. Linearly Growth of Anodic Alumina Oxide (Porous) .....	47
3.6.3. The Mechanism Using Field-Assisted to Grow AAO Templates.....	49
3.7. Y-Branch Shape Multi-segmented AAO Templates.....	49
3.8. Electrodeposition .....	51

3.9. Sample Preparation for Characterization .....	52
<b>Chapter No. 4</b> .....	<b>53</b>
<b>Characterization Techniques</b> .....	<b>54</b>
4.1. Morphological Analysis.....	54
4.1.1. Scanning Electron Microscopy (SEM) .....	54
4.1.2. Energy Dispersive Spectroscopy (EDS) .....	56
4.2. Structural Analysis.....	58
4.2.1. X-ray diffraction (XRD) .....	58
4.2.2. Fourier Transform Infrared Spectroscopy (FTIR) .....	60
4.3. Magnetic Measurements .....	61
4.3.1. Vibrating Sample Magnetometer (VSM).....	61
4.4 Two Point Probe Hall Technique:.....	62
4.4.1. Four Probe Method .....	64
<b>Chapter No. 5</b> .....	<b>65</b>
<b>Electronic, Magnetic and Half-Metallic Properties of <math>L2_1</math>-type <math>\text{Co}_2\text{Mn}_{0.5}\text{Fe}_{0.5}\text{Sn}</math> Heusler alloy Nanowires</b> .....	<b>66</b>
5.1. Introduction.....	66
5.2. Results and Discussions .....	67
5.2.1. Synthesis and Morphology of AAO Templates .....	67
5.2.2. Morphology of Nanowires .....	68
5.2.3. Molecular Analysis .....	68
5.2.4. Structure Analysis .....	69
5.2.5. Compositional Analysis .....	70
5.2.6. Magnetic Measurements .....	71
5.2.7. Electrical Measurements .....	72
5.2.8. Computational Studies .....	74
5.2.9. Spintronics Properties .....	75
<b>Chapter No. 6</b> .....	<b>77</b>
<b>Structural, Magnetic and Transport Properties of Fe-based Full Heusler alloy <math>\text{Fe}_2\text{CoSn}</math> Nanowires</b> .....	<b>78</b>
6.1. Introduction.....	78
6.2. Results and Discussions .....	78
6.2.1. Synthesis of AAO Templates.....	78
6.2.2. Morphology analysis.....	79
6.2.3. Surface Analysis .....	81
6.2.4. Structure Analysis.....	82

6.2.5. Compositional analysis .....	83
6.2.6. Magnetic Properties .....	84
6.2.7. Computational Results .....	86
6.2.8. Electrical Properties .....	88
<b>Chapter No. 7 .....</b>	<b>92</b>
<b>Morphology, structural and magnetic properties of Fe<sub>100-x</sub>Cu<sub>x</sub> alloy nanowires .....</b>	<b>93</b>
7.1. Introduction .....	93
7.2. Results and discussion .....	94
7.2.1. Morphology of AAO templates .....	94
7.2.2. Morphology of FeCu Alloy NWs .....	95
7.2.3. Surface Analysis .....	95
7.2.4 Structural Analysis of FeCu Alloy NWs: .....	96
7.2.5. Magnetic Properties of FeCu Alloy NWs .....	98
<b>Chapter No. 8 .....</b>	<b>102</b>
<b>Structural, Magnetic and Electrical investigations of Fe<sub>1-x</sub>Mn<sub>x</sub> (0 ≤ x ≤ 0.39) alloy Nanowires via Electrodeposition in AAO templates .....</b>	<b>103</b>
8.1. Introduction .....	103
8.2. Results and Discussions .....	104
Conclusion .....	110



## List of Figures

<b>Figure 1. 1:</b> A scheme of ideally arranged nanoporous: (a) top view and (b) cross section.....	8
<b>Figure 1. 2:</b> The shape inherent anisotropy functionalization of NWs (a) Single-component NWs; (b) Double-component NWs, that has aspect ratio of each segment is larger than one; (c) multilayer of double-component NWs, that has the aspect ratio of every segment is smaller than one; (d) double-components of functionalization of the NWs. In the figure, ligands L and L' selectively bind to the two components, and thus the functional groups R and R', corresponding to L and L' respectively that have been spatially separated.....	12
<b>Figure 1. 3:</b> The concept of spintronics .....	13
<b>Figure 1. 4:</b> Development of spintronic devices .....	14
<b>Figure 1. 5:</b> Spin-polarized current generation .....	15
<b>Figure 1. 6:</b> Scheme of a multi-input NOR logic gate with current-drive DW motion .....	17
<b>Figure 1. 7:</b> Periodic table belong to Heusler family; $X_2YZ$ & $XYZ$ .....	18
<b>Figure 1. 8:</b> Full Heusler Structure ( $L2_1$ ) and Half Heusler Structure ( $C1b$ ) respectively.....	19
<b>Figure 1. 9:</b> Calculated spin density of states for various Co-based Heusler alloys as described .....	20
<b>Figure 1. 10:</b> shows the Full Heusler order structure ( $L2_1$ ), partially disorder with Y-Z ( $B2$ ) atoms and full disorder with X-Y & X-Z ( $A2$ ) atoms .....	22
<b>Figure 1. 11:</b> Schematics prolate spheroid's for shape anisotropy .....	24
<b>Figure 1. 12:</b> Schematics diagram for Kohn–Sham equations.....	26
<b>Figure 3. 1:</b> (A) Shows the systematically the porous of anodic alumina and (B) shows the side view of the complete structure of alumina.....	38
<b>Figure 3. 2:</b> Factor effect on the porous diameter of AAO templates.....	39
<b>Figure 3. 3:</b> The experimental procedure for a two-step self-organized anodization .....	43
<b>Figure 3. 4:</b> (A) Graphical representation of the anodizing growth of alumina in Galvanostatic condition and (B) Potentiostatic condition, (C) Overall stages through anodic alumina oxide established.....	45
<b>Figure 3. 5:</b> Schematic diagram with constant anodizing show overlapping process during the growth of AAO templates .....	46
<b>Figure 3. 6:</b> Schematic diagram shows the formations of $OH^-$ and $O^{2-}$ ions at the interface of oxide/electrolyte with $SO_4^{2-}$ anions adsorbed due to water interrelating .....	47

<b>Figure 3. 7:</b> Schematic diagrams illustrate the voids production in the porous layer of anodic alumina due to the condensation mechanism of vacancy .....	48
<b>Figure 3. 8:</b> Schematic representation of the formation of Y-branch AAO templates and deposition of material to synthesize NWs .....	50
<b>Figure 3. 9:</b> The schematic diagram shows the complete synthesis of NWs using electrochemical deposition after removal of the barrier layer.....	51
<b>Figure 4. 1:</b> Functional Block diagram of scanning electron microscope (SEM).....	54
<b>Figure 4. 2:</b> Schematic diagram of a Scanning electron microscope. ....	55
<b>Figure 4. 3:</b> Schematic of inner shell transitions and K, L and M series .....	56
<b>Figure 4. 4:</b> Energy Dispersive Spectrometers .....	57
<b>Figure 4. 5:</b> The Bragg's law determines the spacing of the crystal's lattice (straight black arrow) between the lattice planes surface (blue horizontal lines). The left side and right side Green arrows show incident and scattered X-rays respectively. Where $\theta$ is the diffraction angle between the incident and diffracted X-rays received through the detector.....	59
<b>Figure 4. 6:</b> The schematic diagram Fourier transform infrared spectroscopy (FTIR).....	60
<b>Figure 4. 7:</b> Schematic illustration of VSM .....	62
<b>Figure 4. 8:</b> Setting of two probe system .....	63
<b>Figure 4. 9:</b> Four point probe measurement scheme.....	64
<b>Figure 5. 1:</b> Typical top-view SEM image of AAO templates at 5 $\mu\text{m}$ scale, (b) Top-view SEM image of AAO templates at 1 $\mu\text{m}$ scale, (c) Top-view SEM image of AAO templates at 500 nm scale and (d) the cross-section SEM image of AAO templates.....	67
<b>Figure 5. 2:</b> The SEM images of NWs deposited at different voltages. (a) 12 V, (b) 14 V, (c) 18 V and (d) shows EDX of NWs. ....	68
<b>Figure 5. 3:</b> The FTIR results in Co-based ( $\text{Co}_2\text{Mn}_{0.5}\text{Fe}_{0.5}\text{Sn}$ ) full Heusler alloy NWs.....	69
<b>Figure 5. 4:</b> The X-Ray Diffraction results Co-based ( $\text{Co}_2\text{Mn}_{0.5}\text{Fe}_{0.5}\text{Sn}$ ) full Heusler alloy NWs. ....	70
<b>Figure 5. 5:</b> The dependences of Co, Mn, Fe & Sn deposition on different AC potential value. ....	71
<b>Figure 5. 6:</b> (a) The Hysteresis loops of the Co-based ( $\text{Co}_2\text{Mn}_{0.5}\text{Fe}_{0.5}\text{Sn}$ ) full Heusler alloy NWs (b) The Coercivity and Saturation magnetization against Voltage of Co-based Heusler alloy NWs.....	71
<b>Figure 5. 7:</b> (a) Two probe I-V curves show the resistance of Heusler alloys NWs (b) Shows the Resistance VS Deposition voltages of Heusler alloys NWs.....	73
<b>Figure 5. 8:</b> Hall measurement shows the variation of mobility, carrier concentration & resistivity w.r.t Deposition voltages of Heusler alloys NWs.....	72
<b>Figure 5. 9:</b> Calculation of DOS for Co-based ( $\text{Co}_2\text{Mn}_{0.5}\text{Fe}_{0.5}\text{Sn}$ ) full Heusler compound NWs.....	73
<b>Figure 5. 10:</b> Band structure of majority and minority spin states Co-based ( $\text{Co}_2\text{Mn}_{0.5}\text{Fe}_{0.5}\text{Sn}$ ) full Heusler alloy NWs.....	75

<b>Figure 6. 1:</b> Current VS. time graph using two-step anodization Prepared by 5% H <sub>3</sub> PO <sub>4</sub> .....	79
<b>Figure 6. 2:</b> (a-c) typical top view SEM micrograph of AAO templates and (d) show lateral view prepared by 5% H <sub>3</sub> PO <sub>4</sub> using two-step anodization with a high-density array of AAO templates.....	80
<b>Figure 6. 3:</b> (a-c) SEM images of Fe <sub>2</sub> CoSn Heusler alloy NWs and (d) show EDX, conformation of Fe <sub>2</sub> CoSn Heusler alloy NWs. ....	80
<b>Figure 6. 4:</b> The FTIR results of Fe <sub>2</sub> CoSn Heusler alloy NWs.....	81
<b>Figure 6. 5:</b> The XRD pattern of Fe <sub>2</sub> CoSn Heusler alloy NWs deposited at different AC-voltages. ..	82
<b>Figure 6. 6:</b> Shows EDX pattern of deposited Fe, Co and Sn in Heusler alloy (Fe <sub>2</sub> CoSn) NWs at different AC-voltages.....	84
<b>Figure 6. 7:</b> (a) The Hysteresis loops of the samples deposited at different AC voltages from 9 to 17 V in 60 sec (b) the dependence of coercivity and saturation magnetization of the deposited samples at different AC voltages.....	85
<b>Figure 6. 8:</b> The crystal structure of Fe <sub>2</sub> -based (Fe <sub>2</sub> CoSn) full Heusler compound NWs.....	86
<b>Figure 6. 9:</b> Calculation of TDOS for Fe <sub>2</sub> -based (Fe <sub>2</sub> CoSn) full Heusler compound NWs. ....	86
<b>Figure 6. 10:</b> Calculation of PDOS for Fe <sub>2</sub> -based (Fe <sub>2</sub> CoSn) full Heusler compound NWs. ....	87
<b>Figure 6. 11:</b> Band structure of majority and minority spin states Fe <sub>2</sub> -based (Fe <sub>2</sub> CoSn) full Heusler compound NWs. ....	88
<b>Figure 6. 12:</b> The variation of Current w.r.t deposition voltage. ....	89
<b>Figure 6. 13:</b> The variation of mobility, resistivity and carrier concentration w.r.t deposition voltages. ....	89
<b>Figure 6. 14:</b> The variation of sheet resistance, resistivity and conductivity w. r. t deposition voltages. ....	90
<b>Figure 7. 1:</b> SEM image of AAO template after second step anodization, (b)SEM image of AAO template after 30 min immersing in phosphoric acid and (c) the cross-section SEM image of AAO template (d) the EDX of templates. ....	94
<b>Figure 7. 2:</b> Shows the SEM images of FeCu NWs after removing the AAO templates, (a) SEM image of FeCu NWs at 5 μm scale, (b) SEM image of FeCu NWs at 2 μm scale, (c) SEM image of FeCu NWs at 1 μm scale and (d) Shows EDX of FeCu NWs. ....	95
<b>Figure 7. 3:</b> (a &b) The AFM images of AAO template after second step anodization and (c &d) the AFM images of FeCu NWs after removing the AAO templates. ....	96
<b>Figure 7. 4:</b> XRD spectra of FeCu NWs arrays of various content (at %) embedded into AAO templates. ....	97
<b>Figure 7. 5:</b> The variation of grain size and lattice strain of pure Fe and FeCu alloy NWs as a function of Fe <sub>100-x</sub> Cu <sub>x</sub> content (at %).....	98

<b>Figure 7. 6:</b> Hysteresis loops of electrodeposited pure Fe and FeCu NWs perpendicular to the plane of the membrane with different Fe <sub>100-x</sub> Cu <sub>x</sub> content (at %) at a constant voltage (16V).The inset shows an enlargement of the central part of the loop. ....	99
<b>Figure 7. 7:</b> Hysteresis loops of electrodeposited pure Fe and FeCu NWs parallel to the plane of the membrane with different Fe <sub>100-x</sub> Cu <sub>x</sub> content (at %) at a constant voltage (16V). The inset shows an enlargement of the central part of the loop. ....	100
<b>Figure 7. 8:</b> Behavior of coercivity and squareness (a) Parallel and (b) Perpendicular to NWs long axis as function of Fe and Cu content in NWs.....	101
<b>Figure 8. 1:</b> (a, b & c) A typical top view SEM results and (d).show EDX result of AAO templates Prepared by 5% H <sub>3</sub> PO <sub>4</sub> with a high-density array of Nanopores.....	104
<b>Figure 8. 2:</b> (a, b & c) The SEM analysis and (d) EDX result of FeMn alloy NWs.....	105
<b>Figure 8. 3:</b> XRD patterns of FeMn alloy NWs.....	106
<b>Figure 8. 4:</b> The Grain size and Dislocations of FeMn NWs w.r.t atomic % of Fe and Mn.....	107
<b>Figure 8. 5:</b> Four probe (Hall measurement) analysis show the variation of mobility, Conductivity & resistivity w.r.t at% of Fe and Mn in FeMn alloys NWs. ....	108
<b>Figure 8. 6:</b> Show the magnetic response of FeMn alloy NWs with the external magnetic field aligned parallel to the long axis. ....	109

## List of Tables

<b>Table 5. 1:</b> Different properties of Co-based ( $\text{Co}_2\text{Mn}_{0.5}\text{Fe}_{0.5}\text{Sn}$ ) full Heusler compound NWs.....	72
<b>Table 6. 1:</b> Show the different experimental results varies w.r.t deposition voltage. ....	85
<b>Table 7. 1:</b> Show chemical and structural parameters of electrodeposited FeCu NWs as a function of different composition contents (at %). ....	98
<b>Table 7. 2:</b> Show various magnetic parameters of electrodeposited FeCu NWs as a function of different composition contents (at %). ....	100
<b>Table 8. 1:</b> Present different results are taken from XRD and VSM technique comparison with concentration bath solution (EDX) of FeMn alloy NWs. ....	106

## Abstract

The spintronics is the developing and motivating research area that enhanced the efficiency of conventional electronics devices by the addition of spin degree of freedom such as; to decrease the consumption of electric power, improve the speed of data processing and enhance the integrated densities. This research focuses the physical and structural properties of quaternary full Heusler and binary (magnetic-nonmagnetic) alloys in the field of spintronics. As Heusler alloy nanowires (NWs) is a young research field, therefore the majority research focuses on their synthesis, magnetic properties and structural properties. The main issue is the size dependent structure, transition of phase, spin and magnetic related properties are open for the wide range of research. In the last few decades, Heusler (Half Heusler/full Heusler) family produced the revolutionary effect towards spintronics or magneto-electronics with large Curie temperature, especially at the nanoscale. The spin polarized current showed maximum value due to gap at Fermi level (100% spin-polarization) that increased the efficiency of magneto-electronic devices.

Among all, several alloys of Heusler family behave like half-metals. The shape anisotropy in the ferromagnetic nanostructure especially in Heusler alloys is required presently as well as in future spintronics devices. For such reason, the research has been directed towards the quaternary (full Heusler alloy) half-metallic ferromagnetism and binary alloy (Ferro-nonferro coupling) to open the new way to fulfill the requirements of present and future prospectus.

Full Heusler alloys, called quaternary i.e  $X_2YZ$  (2:1:1), where Z and (X & Y) belongs to transition and main group element respectively. And the structure of such a Heusler family is characterized through  $L2_1$  Presently, cobalt and iron-based full-Heusler alloys focus their attention in spintronics based devices such as magnetoresistance (MR), giant magnetoresistance (GMR) and tunneling magnetoresistance (TMR) and provide maximum stability due to half-metallic nature. The Co-based  $Co_2Mn_{0.5}Fe_{0.5}Sn$  full Heusler alloy NWs were synthesized through alternating current (AC) electrochemical deposition (ECD) in anodized aluminum oxide (AAO) templates. To approach the required results, homemade AAO templates were synthesized by two-step anodization in 5 %  $H_3PO_4$  solution using 60 V at constant DC source at temperature range 1 to 5 °C. Achieving the desired structure of full Heusler ( $L2_1$ ) alloys NWs became possible in electrochemically by changing the AC-

deposition potential from 10 to 18V by the 2V difference. The origin of band gap at Fermi level confirmed the half metallic character (100% spin polarization), that has been measured through density functional theory (DFT) by using WIEN2k programs of full potential linearized augmented plane wave (FP-LAPW) technique. The diameter of the AAO templates and NWs was found in the range of 55 to 65nm that is confirmed from scanning electron microscope (SEM) in all synthesized Heusler alloy and binary alloy NWs. The formation of partial disorder (B2-type), full disorder (A2-type) and full order ( $L2_1$ ) structure of  $\text{Co}_2\text{Mn}_{0.5}\text{Fe}_{0.5}\text{Sn}$  full Heusler alloy is confirmed through X-rays diffraction (XRD) analysis that has been measured in anodic alumina along with substrate of aluminum. Hence at 16V and 18V, the presence of fundamental, even and odd super lattice peaks confirmed the full order ( $L2_1$ ) structure of  $\text{Co}_2\text{Mn}_{0.5}\text{Fe}_{0.5}\text{Sn}$  full Heusler alloy NWs. The deposition of Co, Mn & Fe increases with increase in deposition voltage, whereas Sn shows decreasing order, which implies that each element has different reduction potential. The electrical measurement was examined without AAO templates, the resistivity shows decreasing order (from 160 to 40  $\Omega\text{-cm}$ ) to that of mobility shows opposite fashion (28 to 358  $\text{cm}^2/\text{Vs}$ ) with respect to increasing in deposition potential. It means that our sample is a metallic character which reduces the electron grain boundary dispersal and a boost of the grain size. The magnetic properties illustrate that coercivity shows sharp increment (from 65 to 245Oe) at 18V owing the formation of fully order ( $L2_1$ ) structure of  $\text{Co}_2\text{Mn}_{0.5}\text{Fe}_{0.5}\text{Sn}$  full Heusler alloy NWs.

Fe-based  $\text{Fe}_2\text{CoSn}$  full Heusler alloy NWs has been synthesized with the same approach, as AC- deposition potential has taken from 9 to 17V by the increment of 2V to achieve the desired results of  $L2_1$  structure with a combination of 2:1:1 ratio. The influence of deposition voltage on chemical composition, electric/magnetic properties, morphology and crystal structure is studied. The half-metallic ferromagnetism in  $\text{Fe}_2\text{CoSn}$  Heusler alloy NWs is investigated by using the FP-LAPW technique to resolve the Kohn-Sham equations executing WIEN2k program. Hence, the spin polarization, partial density of states (PDOS) shows that at Fermi level few states of Fe-3d exist. Though the states are very minor and contribute very minute in conduction, related to the minority channel. Secondly, such alloy obeys Slater-Pauling rule, in which total spin magnetic moment directly proportional to the electrons of valance shell in the unit cell of  $\text{Fe}_2\text{CoSn}$  Heusler alloy NWs. XRD measurement of such NWs reflects (311) peak through all samples that related to the substrate of aluminum. The peaks of fundamental, odd and even super lattice have been observed all together in 15V

and 17V. It confirmed the full order structure ( $L2_1$ ) of  $Fe_2CoSn$  Heusler alloy NWs. Below which, A2 and B2-type disorder structure have been synthesized. Besides these, variation and Shift are observed in the intensity of diffraction peaks, that shows the influence of deposition voltage on composition, the order of chemical structure and lattice constant. The increment of the grain size shows the maximum result with the formation of  $L2_1$  Heusler structure. With such specific structure of  $Fe_2CoSn$  Heusler alloy NWs, the M-H loops demonstrate that coercivity attained maximum value (484 Oe) at 17V by making some defects that divide such NWs into tiny magnetics, causing the rise in magneto-crystalline anisotropy and blocking the domain walls. The non-ohmic behavior is taken from two probes (I-V) technique whereas  $Fe_2CoSn$  Heusler alloy NWs with  $L2_1$  structure followed the excellent spin-dependent function.

Ferromagnetic NWs such as Fe or Co are precise class that can be used in long range application particularly, in data-storage devices, magneto-resistive sensors and spin dependent devices. The properties of such devices directly related to the morphology and composition parameters. Therefore, to enhance the function of such devices, the ferromagnetic (Fe or Co) make alloy NWs with nonmagnetic element such Cu or Mn to form Fe-Cu or Fe-Mn were also synthesized. The advantage of such alloy NWs is that it can tune the magnetic and transport parameters through morphology and composition ratio. Today the active research material i.e copper (Cu) has large surface activity, good biocompatibility and excellent conduction and physicochemical properties. To enhance the function of the magnetic, electronic and medical application, nonmagnetic-ferromagnetic is added such as incorporate FeCu in nanodevices. Hence, the  $Fe_{100-x}Cu_x$  alloy NWs have been synthesized with the same above approach. Only deposition potential (16V) remained constant and the concentration of Fe-Cu in the electrolyte solution is changed. The XRD pattern analysis confirms that initially, the peaks of Fe-*bcc* is observed due to the deposition of pure Fe-electrolyte solution. Hence, copper (Cu) concentration is added gradually with Fe-bath solution, then  $Fe_{100-x}Cu_x$  *bcc* peaks are observed in all remaining three samples through miller indices (200) and (110) planes and suppressed the Fe-*bcc* peaks completely. The value of the lattice parameter has increased that affects to decrease the lattice strain. Hence, such parameter influences on peaks (FeCu) shift towards lower angle. The grain size shows ascending order by the increment of Cu at%. From M-H loops, it is observed that squareness ( $M_R/M_S$ ) and coercivity ( $H_c$ ) both displays descending order with increment of Cu contents in  $Fe_{100-x}Cu_x$  alloy NWs, having Cu



(diamagnetic) with greater atomic radius relative to Fe, that effected to suppress the magnetic moment alignments of Fe.

Similarly, iron, which is ferromagnetic material coupling with non-ferromagnetic such as manganese at nanoscale shows interfacial exchange coupling. The Fe-Mn is a biologically (biodegradable) alloying element, as a high ratio of Mn is observed to be not toxic, especially in tiny mesh-like metallic tubular (stent), that increases its effectiveness in the narrow arteries. For such point of view, the last step of this research is directed to synthesize the  $Fe_{1-x}Mn_x$  alloy NWs, by using AC-electrochemical deposition in AAO templates through a similar approach as above. The analysis of X-ray diffraction (XRD) pattern shows that the aluminum peak are observed because of such NWs are characterized with the substrate. The XRD patterns exhibited the FeMn NWs were crystallized into body centered cubic (*bcc*) structure. Furthermore, the lattice parameter of FeMn NWs was decreased with addition of Mn content. The grain size shows the increasing order (from 38 to 53nm) w.r.t to increase the concentration of Mn in  $Fe_{1-x}Mn_x$  bath solution that effect to decrease the dislocation density and lattice strain of the FeMn alloy NWs. Using four-probe (Hall measurement) technique, it was found that resistivity has been decreased gradually (24 to 75.5  $\Omega.cm$ ) whereas conductivity declines with an increase in Mn contents by the effect of an increment of the grain size. Hence, behavior of such alloy moves toward the nonmetallic character. The M-H loops demonstrate that shape anisotropy is dominated in  $Fe_{1-x}Mn_x$  alloy NWs. The increase in Mn contents in such alloy, the coercivity and squareness both shows descending order, opposite to that of grain size. Therefore, it has attributed the motion of domain walls due to the decrease the magnetic grain boundaries.

---

---

# Chapter No. 1

---

---

## Chapter No. 1

### Introduction

#### 1.1. Introduction to Nano

The literature survey clears the meaning of nanostructure, which is defined as 'any structure with one or more dimensions lies in the range of less than a 100-nanometer scale'. Further modification of the above definition, that a nanostructure should have its characteristic dimension in size between a molecule and a bacterium (i.e. atomic to submicron size). Nanostructures comprise the structures in wide-range categories within nanometer ranges such as quantum dots, nanoparticles, nanowires, nanorods, thin films, and nanostripes, etc. These structures can be subdivided into zero-dimensional (quantum dots and nanoparticles), one dimensional (NWs and NTs) and two dimensional (such as thin films) nanostructures on the basis of their individual length to their preferred physical quantity. To reduce its dimensional structure such as from bulk to nano, which change their properties through quantum mechanical approach that appears in their structures. The technologies based on the nanostructures and their capability to enhance their efficiency are collectively called Nanotechnology. Nanotechnology has extensive applications and it is used in every field of life, such as in medicine, microelectronics, spin electronic devices, genetics, magnetic storage devices etc. Especially the introducing of microelectronics devices, nanotechnology has made the smaller devices in size that have cheaper, run fast and huge energy efficient. The nanotechnology concept was first time introduced by Dr. Richard Feynman at 'American Physical Society meeting' was held at Caltech on 29<sup>th</sup> December 1959 through his famous lecture, "There is Plenty of Room at the Bottom" [1]. Before 1980, no one had agreed with the hypothesis of Feynman in the scientific world. After the 80s, new technologies were discovered like Scanning Tunneling microscope in 1981 [2], that can analyze the surface morphology on the atomic level. After that scientific research was motivated to reduce the size of electronic devices less than 10 $\mu$ m. Knoedler *et al* were reported NWs first in 1990 [3]. The first carbon nanotubes (CNT), were discovered independently in 1993 by D. S. Bethune [4] and S. Ijima [5].

## 1.2. Factors Affect during Anodization of Aluminum

Anodization or Anodic oxidation of aluminum has been extensively used for many decades for the decorating and shielding on the desired surfaces [6]. The microstructure of the synthesized alumina films was observed through electron microscope techniques [7].

It was observed that two types of anodized aluminum oxide templates may exist that depends on the conditions of fabrication. If neutral or basic solutions ( $\text{pH} > 5$ ) are used for anodization, non-porous, flat and bland insulating “barrier” oxide film was formed. But if the anodization process was carried out in an acidic ( $\text{pH} < 5$ ) electrolyte, such as phosphoric acid ( $\text{H}_3\text{PO}_4$ ), sulphuric acid ( $\text{H}_2\text{SO}_4$ ) and oxalic acid ( $\text{CH}_3\text{COOH}$ ), that produced deep pores, having the diameters stretch from 5 to 100 nm and length exist in a few microns, depends on anodizing voltage and the time of anodization respectively. This oxide is referred to as anodizing aluminum oxide (AAO) templates or porous anodic alumina (PAA). 10-100 nm thick barrier layer or thin film was formed at the bottom of each porous depend upon the type and concentration of electrolyte as well as the time and anodization potential as well [7-11].

The anodization of aluminum (AAO) is synthesized in acidic electrolytes with approximately hexagonal pore structure, has been observed since 1960. First time, highly ordered and uniform AAO templates were synthesized through two-steps of anodization and it was reported by Fukuda and Masuda in 1995 [12]. During the first step of anodization, non-uniform and disorder AAO templates were formed. To align them, which is essential for the synthesis of NWs, mixed 1.8 wt% of chromic acid and 6 wt% of phosphoric acid together to form a yellow solution. The sample (AAO templates) was dipped in the yellow solution for 2-Hrs at  $60^\circ\text{C}$  to etch the irregular templates and leave the periodic curved topographies on the surface of the Aluminum host. The second step of anodization was carried out through the same conditions as in the first step, but it took longer time as compared to the first step. The concave topographies were acted as pore nucleation spots, which obtained a uniform and highly-ordered AAO templates. More homogenous, uniform and perfectly ordered arrays of nanopore over a huge area were synthesized through pre-patterning techniques, such as lithography nanoimprint [13].

The PAA membrane can be selectively dissolved in mercuric chloride ( $\text{HgCl}_2$ ) solution and the pores of PAA membrane can be increased in diameter (pore widening) as well as the

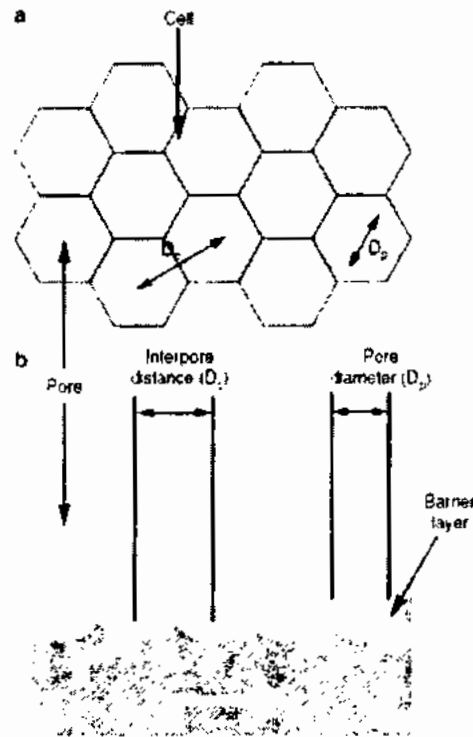


**Figure 1. 1:** A scheme of ideally arranged nanoporous: (a) top view and (b) cross section

removal of barrier layer at the bottom, when immersed in 5% phosphoric acid solution [14, 15], instead of ion-beam sputtering or wet etching [16, 17].

### 1.2.1. Various Shape of Different Materials Synthesized from AAO Templates

Anodic aluminum oxide (AAO) templates using two steps of anodization is one of the most common technique to synthesize nanostructured of different materials obtained by the electrochemical process. Due to its controllable synthesis technique, one can obtain the templates with desirable geometrical features. Hence, the variety of, nanotubes, nanorods and NWs has been synthesized with chemical, physical, and electrochemical techniques with desired material deposition into the pores of AAO templates. Such nanostructures of the deposited materials that enhance the electric, magnetic, sensing, optical, and catalytic properties due to its small size (less than 100 nm), high-aspect ratio and unique morphology related to the same material in bulk structure. Besides, Anodic oxidation of aluminum itself possesses various motivating and interesting properties like luminescence or surface chemistry.

### 1.2.2. Some Fundamental Features of Anodic Porous Alumina

It is clear from above that AAO templates are fabricated by anodizing aluminum in an acidic electrolyte. The nanoporous arrays can be in the order of the close-packed honeycomb structure as shown in Fig. 1.1. The diameter, length and interpore distance can be precisely controlled by varying the anodization conditions. The literature survey confirmed that the synthesis of anodizing aluminum oxide (AAO) templates can be traced back to 1950s, where they start from one-step of anodization [18]. It has a high pore density ( $\sim 10^{11}$  pores/cm<sup>2</sup>), that allows us to construct a large number of NWs simultaneously. The pore walls can be altered through a reaction using silane compounds, which is the exciting and motivating feature of the porous alumina template [19].

The precise and control synthesis of AAO templates by electrochemical anodization can be employed over a long range of diameter, length, and interpore distance. The Anodization process needs some basic parameters such as anodization current, voltage, chemical compositions, pH of electrolyte and temperature are all adjusted suitably to obtain the desired distribution of length, diameter and interpore distance [12]. The AAO template is stable at high temperature during the electrochemical deposition technique, NWs of different metals can be annealed inside the pores of AAO templates.

### 1.2.3. Applications of Porous Aluminum Oxide Templates

The key role of AAO templates in nanotechnology is the synthesis of NTs and NWs having better ordering, compared to the membranes of track-etched polycarbonate and macroporous silicon templates. The desired results can be achieved by changing the concentration of electrolyte and anodization voltage [20].

An additional PAA film is used in the production of nano-dot arrays on various substrates. These arrays can be synthesized from PAA films as masks; that gives us economical and low-cost alternate towards traditional lithography techniques [21-23].

In the last few decades, potential usage of highly ordered AAO templates and PAA films in magnetic recording devices [24] and optical sensors has attracted much attention [25, 26].

#### 1.2.4. Importance of Template-Based NWs via Different Deposition Technique

During the past 15-20 years, template-based NWs and NTs have been synthesized in a regular and order form which is the most important use of AAO templates [20, 24, 27]. The main techniques through AAO templates, synthesized from 1D nanostructures, are electrophoretic deposition, template wetting, and electrochemical deposition.

Under an electrical field, the motion of charged particles is oriented in a colloidal solution through Electrophoretic deposition. If the particles are charged negatively, the deposition takes place at the anode, otherwise, it occurs on the cathode. Synthesis of AAO templates is prepared through similar condition for both deposition techniques; electrochemical deposition and electrophoretic deposition [24]. Nanostructures were fabricated from perylene derivatives and phthalocyanines [28, 29] through electrophoretic deposition technique. In template wetting technique, NWs and NTs are synthesized via evaporation of desired material of molten state in AAO templates [30]. Such a technique has been useful to fabricate 1D nanostructures from both small organic molecules [31] and polymers [32]. The deposition in AAO templates through vacuum evaporation can also be introduced to synthesize nanostructures [24], from phenanthrene, cabazole, anthracene and naphthalene [33].

In electrochemical deposition technique, different types of reactive charge species in a solution were diffused through an external electric field. Such a technique is only useful for electrically conductive materials; electrically conductive polymers, metals alloys, Heusler alloys semiconductors, and their oxides. The templates can either be used as a free-standing membrane for the synthesis of NWs and NTs as well as it is also applicable for the synthesis of a thin film on conductive support [24, 34].

#### 1.3. Brief Survey of Nanowires Applications

Vaseashta *et al.* studied the use of NWs, NTs, and nanoparticles in a wide range of bio-compatibility, such as proteins, DNA, cells, RNA and extremely small molecules [35]. In addition with bio-medical, semiconductor QDs, NWs and NTs have been used as fluorescent probes, quantum-dot field-effect and memory devices [36]. Homogenous and uniform nanoporous materials have been effectively synthesized for the measurement of gas moisture, humidity sensors and electrochemical biosensors [37]. Shortly, templates based magnetic NWs that have been synthesized from the combination of different alloys used as a magneto-resistive

bridge sensor, single bit data memory storage devices (single-electron memory device). Shortly the main research in the literature that focus on various devices based on nano-porous structure, NTs and NWs have been reported [38].

### **1.3.1. Biomedical Applications of Magnetic Nanowires**

There are various materials and techniques which are used in nanotechnology for various biology and medical applications as briefly explained below.

#### **1.3.1.1. Nanotechnology for Cancer Cells**

Different techniques and materials are used in the nanotechnology for cancer cells to resolve their different complications. On the basis of research, the nanotechnology for cancer is divided into seven groups. First, to detect and premature imaging the cancer cells called pre-symptomatic. Secondly, in nanotechnology that develops such a technique to assist the effects of therapies. Third to invent such device that directly sends therapeutic mediators to the tumor position without the barrier biological tissues. Fourth, such agents were developed that can check and assists the changes in predictive molecules to avoid and prevent any issue related to the cell of pre-cancerous. Fifth for the mutations identification first to enhance the surveillance system function that causes and to detect the cancer genetic markers. Second last (Sixth) to develop such a technique that controls and resist the cancer symptoms that strongly affected the lifestyle of a human being. Last (seventh) but not the least to develop the methods or techniques to help the scientists to find the quick and rapid identification of cancer cells [39].

### **1.3.2. Use of Single and Multi-Functional Magnetic Nanowires in the Field of Biomedicines**

In biomedicines, almost magnetic NWs are used that are synthesized in the pores of AAO templates through electrochemical deposition. The diameter and radius of NWs are placed in 5 to 500 nm range, and the length was placed almost 60  $\mu\text{m}$  range. Fig. 1.2(b) and (c) show the structure of multi-segmented NWs. According to Chen *et al.* 2003 and Sun *et al.* 2005, observed that coupling between the layers of each segmented NWs must be accurately controlled, which provide the flexibilities to the NWs to affect and precisely decrease their magnetic properties. Fig. 1.2(d) shows the segments of multi-NWs are selectively bound for multiple functionalize observed by Reich *et al.* 2003 and the features of such NWs could affect to enhance the properties of magnetic NWs in the use of bio-magnetic applications.

The factors that affect the properties of magnetic NWs; such as, saturation field, remanence magnetization, coercivity, alignment of easy axis and Curie temperature could be



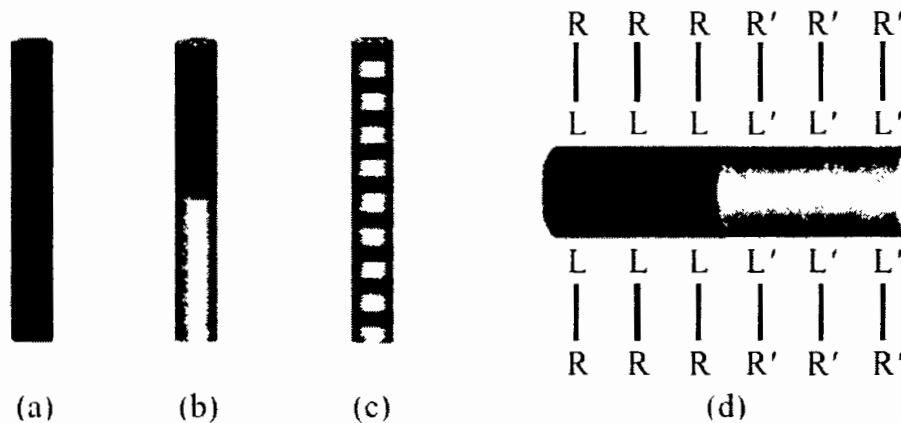


**Figure 1. 2:** The shape inherent anisotropy functionalization of NWs (a) Single-component NWs; (b) Double-component NWs, that has aspect ratio of each segment is larger than one; (c) multilayer of double-component NWs, that has the aspect ratio of every segment is smaller than one; (d) double-components of functionalization of the NWs. In the figure, ligands L and L' selectively bind to the two components, and thus the functional groups R and R', corresponding to L and L' respectively that have been spatially separated.

adjusted by varying thickness and diameter of the NWs, also affected the compositional concentration of the magnetic/non-magnetic multi-segmented and specially on the specific structure of Heusler alloy NWs (Sun *et al.* 2005).

#### 1.3.2.1. Biomolecular Manipulation

The Biomolecules can be analyzed through external magnetic field in a form of magnetic NWs that manipulate it for various medical applications.

#### 1.3.2.2 Spatial Organization of Cells

For several bio-medical usages, the capability that make to organize the living cells especially in biosensing and adhesion of biochemistry cell. Tanase *et al.* (2005) examined mammalian cells using ferromagnetic NWs that were spatially organized.

#### 1.3.2.3. Biomolecular Separation

Biomolecules can be separated at large scale using magnetic NWs. In such application (cell separations) both segmented (single and double) NWs have been used. In the separations of the cell, the magnetic NWs overtake instead of magnetic spherical beads.

#### 1.3.2.4. Gene Delivery

The gene delivery has not been controlled at the nanoscale due to conventional methods. According to Hurst *et al.* 2006, foreign DNA delivered into the target cell by their limited capacity of the system due to comparatively at their less transfection effectiveness. But more

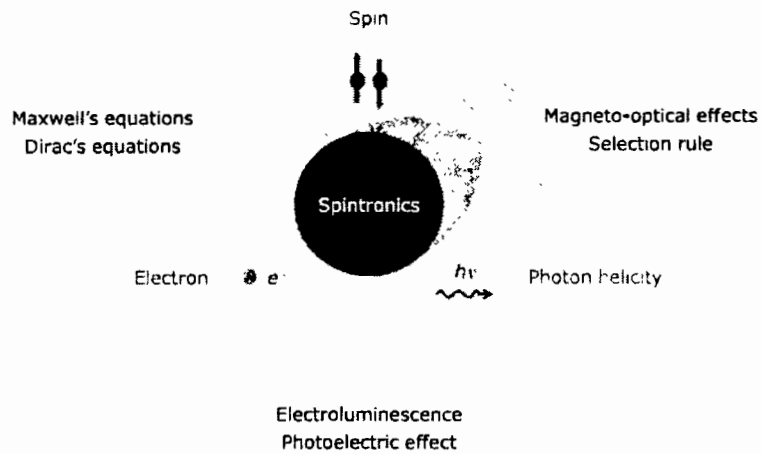


**Figure 1. 3:** The concept of spintronics

advantage and important to delivery of the gene, if magnetic NWs have been used. Since during the synthesis of such NWs, there must be more conscious to synthesize the desired length and diameter accurately.

#### 1.4. Spintronics

Spintronics is the recent emergent and devolving area in nanotechnology, which built on the arrangement of three conventional carriers; photons spin, electron spins, and charge on the electron as listed in Fig. 1.3 [43]. In information communications technology (ICT), those carriers cover three vital zones; data processing through transport of electron, storage data through the spins assembly and finally through optical conjunction data is then transferred. The electron having full spin-polarization called Spintronics that plays a key role in the present and in future technological applications; such as in recording data due to non-volatile and consume minute power result in the operation of refreshing data.

The importance of spin-dependent electrons (spintronics) was known after the discovery of giant magnetoresistance (GMR) in 1988. Such a system change the resistance, depends on the orientation of magnetic multilayers separated through a spacer of non-magnetic. Since the hard disk drives (HDD) was modified through 'GMR' in few years after this (GMR) discovery. Hence the revolutionary effect produced in information storage devices and the impact on their technology was presented for a Nobel Prize in the field of Physics 2007 [40].

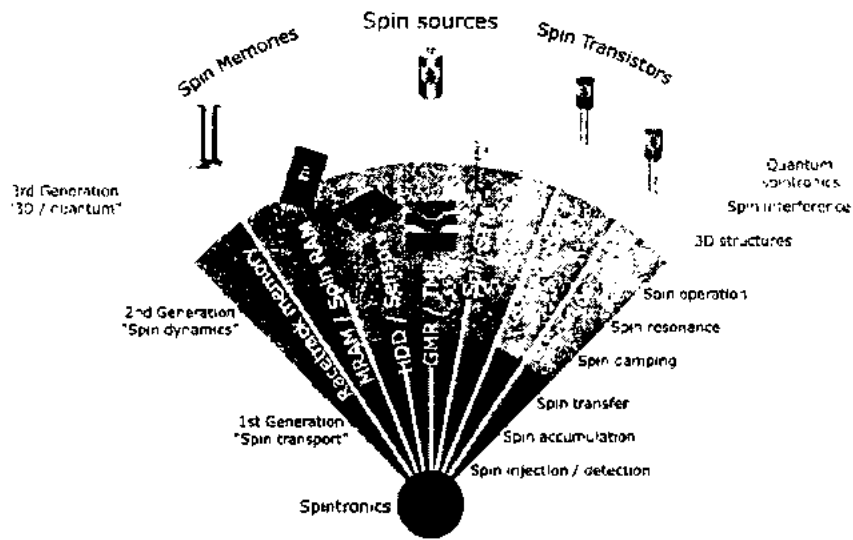


Figure 1. 4: Development of spintronic devices

In advancing spin memories major and significant steps have been taken, comprising the development of spin transistors and racetrack memory as schematically presented in Fig. 1.4 [41]. Such devices/technology can be classified according to their operation into three main types of generations; (a) spin transport, (b) spin dynamics and (c) 3- dimension (3D)/ quantum physics

Presently six (6) different techniques have been employed as listed in Fig. 1.5, that used to inject the spin-polarized electrons in non-magnetic materials; (1) magnetic fields, (2) circularly polarized photoexcitation (3) spin injection from a ferromagnetic (4) Zeeman splitting (5) thermal gradients and (6) electric fields. Hence the third is the most important and common technique for dilute magnetic semiconductors (DMS) and half-metallic ferromagnetism (HMF) [42]. In such technique, spins are injected into semiconductors or non-magnetic metal via tunnel barrier or an Ohmic contact and at the interface, it must minimize the conductance mismatch [43].

## 1.5 Nanotechnology Based on Nanowires in the Present and Future Prospectus

The researchers were succeeded to achieve new properties at mid of 20<sup>th</sup> century through the formation of thin film deposition. The properties of a thin film that were diverged from the

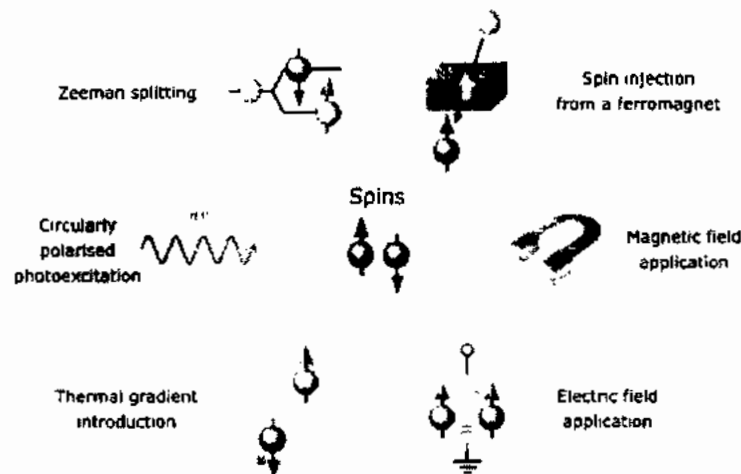


**Figure 1. 5: Spin-polarized current generation**

bulk complement due to their large aspect ratio, very small thickness that affects strongly on its electronic, transport and magnetic properties. The discovery of 2-dimensional (thin film) along with one-dimensional (NWs and NTs) that open the door of new technology.

For the last few decades, various NWs were grown with a different composition such as, to synthesize with a single element as well as through multi-composition called alloy NWs that have been comprehensively discussed in literature; metal [44], semiconductors [45] and oxides [46] NWs. These NWs can be synthesized either by chemical or physical technique, such as thermal evaporation technique [47], vapor-liquid-solid technique (VLS), focused ion beam (FIB) technique [48] and the most suitable, economical and easy to handle is the templates based electrochemical deposition technique (ECD) [49].

Carbon NTs are the most prominent specimen of the 1-dimensional nanostructure. Carbon NTs show peculiarly in electrical and mechanical behavior [50]. But the usages of NWs cover an extensive range of the various field of nanotechnology; like spin accumulation, field emission transistors, domain walls movement [51], spin-torque [52], and magnetoresistance (MR) [53].

### 1.5.1 Use of Single Elemental NWs in Diverse Areas of Nanotechnology

The single elemental magnetic NWs can be used to store the data in high-density magnetic devices. Since each individual NWs can store the information in a form of one or more bits,

and due to the anisotropic behavior of NWs, wherever the size of each individual bit is restricted through single magnetic domain size. In NWs the domain wall pinning is an important and of huge interest. In magnetic NWs, the properties of the domain wall was observed through micro-magnetic simulations [54]. Forster *et al.* observed that in NWs, the transverse walls and vortex walls are formed if the diameter  $d < 20$  nm and  $d > 20$  nm respectively [54]. The vortex and transverse walls energy are equal if the diameter of the NWs  $d = 20$  nm. They also observed that the transverse wall motion is almost 1.3 times less than the motion of the vortex wall. The experimental researcher observed that the wall of the Bloch point is located at the center of NWs between the walls of the vortex. In permalloy cylindrical shaped NWs the domain wall nucleation could be controlled by two methods that are currently reported by Da Col *et al.* The maximum average velocity of the magnetic domain wall in CoFeB ring-shaped NWs has been reported almost 550 m/s [55].

### 1.5.2. Use of Multi-layer NWs in Diverse Areas of Nanotechnology

The researchers gained a special interest in the multilayered NWs because of the discovery of GMR phenomena [56]. The resistance was taken by GMR that comprises a huge alteration in their structure through alternate layers of magnetic and non-magnetic materials. For the data storage applications, such NWs create a lot of attention for the coming generation in both field of research; theoretically and experimentally. Some researchers have been reported two different combinations of magnetic NWs; an alloy of CoNi NWs and the shape variations in FeCoCu and Co [57] that has been used in a similar application to control the domain wall motion.

### 1.6. Present Research on Electronic Devices Based on Magnetic Nanowires

Magnetic NWs have the capability that provides an alternative path that increases the efficiency of electronic devices, especially which were synthesized from traditional semiconductor bulk materials. The geometry that provides the complete logic design of the planar magnetic NWs that may be assembled through a single circuit. The spin-valve or piezoelectric NWs based devices by a hybrid method, using an external electric field that provides energy to the induced strain result in the making gates of magnetic domain wall. The racetrack memory can work on the same principle [58]. The gates of elementary domain wall that control by a proper voltage as shown in Fig.1.6 (multi-input NOR logic function). The domain wall has been driven to cause the current through 'Control A'. The  $B1$  and  $B0$  are the input controlled DW gates

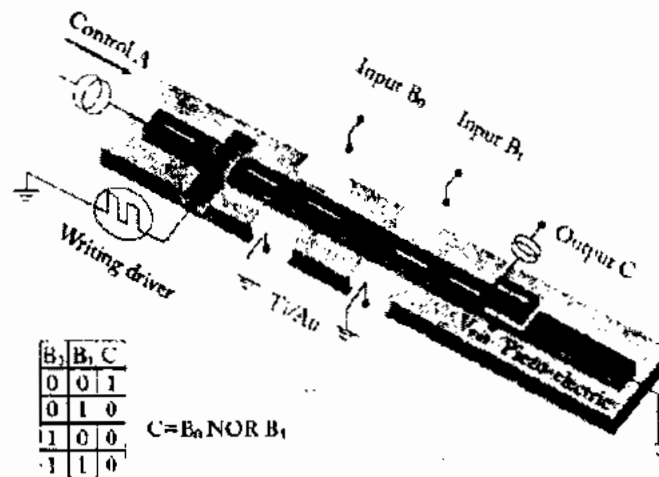


**Figure 1. 6:** Scheme of a multi-input NOR logic gate with current-drive DW motion

(piezoelectric). The TMR affected through the wire magnetization because of the reading result of output 'C'.

The above circuit is working according to the write line in which current moves that create Oersted field by means of domain wall (DW) in the wire is nucleated. The resultant (output) shows 0-state, either both  $B1$  and  $B0$  voltages or one is applied ( $I$ -state), due to piezoelectric layer induced the local stress as domain wall (DW) blocked which follow by them. Since the output show reverse behavior, in which domain wall (DW) move freely in the direction of wire forced through spin-polarized, if both inputs  $B1$  and  $B0$  are in 0-state. Hence at  $C$ , it shows reversal magnetization.

### 1.7. History of Heusler Alloys

In the backdate 1903, Fritz Heusler discovered that addition of *sp*-elements (In, Al, Bi, Sn or Bi) with Cu-Mn alloy change into ferromagnetic, although none of its elements has ferromagnetic material [59]. The basic and fundamental information of its composition and crystal structure of such alloys were unidentified for a long period of time. In 1929, Potter *et al* used X-rays technique to investigate the structure of Cu-Mn-Al alloy, that showed that all the elements of this alloy were in the order of face-centered cubic structure (fcc) superlattice [60]. The structure of the same alloy was examined in detail by Rodgers and Bradley using X-

**X<sub>2</sub>YZ Heusler compounds**

H 2.20																	He	
Li 0.98	Be 1.57											B 2.04	C 2.55	N 3.04	O 3.44	F 3.98	Ne	
Na 0.93	Mg 1.31											Al 1.61	Si 1.90	P 2.19	S 2.58	Cl 3.16	Ar	
K 0.82	Ca 1.00	Sc 1.30	Ti 1.54	V 1.63	Cr 1.66	Mn 1.55	Fe 1.83	Co 1.88	Ni 1.91	Cu 1.90	Zn 1.65	Ga 1.81	Ge 2.03	As 2.18	Se 2.55	Br 2.96	Kr 3.00	
Rb 0.82	Sr 0.95	Y 1.22	Zr 1.33	Nb 1.60	Mo 2.16	Tc 1.90	Ru 2.20	Rh 2.28	Pd 2.20	Ag 1.93	Cd 1.69	In 1.78	Sn 1.96	Sb 2.06	Te 2.10	I 2.66	Xe 2.60	
Cs 0.79	Ba 0.89			Hf 1.30	Ta 1.50	W 1.70	Re 1.90	Os 2.20	Ir 2.20	Pt 2.20	Au 2.40	Hg 1.90	Tl 1.80	Pb 1.80	Bi 1.90	Po 2.00	At 2.20	Rn
Fr 0.70	Ra 0.90																	
		La 1.10	Ce 1.12	Pr 1.13	Nd 1.14	Pm 1.13	Sm 1.17	Eu 1.20	Gd 1.20	Tb 1.10	Dy 1.22	Ho 1.23	Er 1.24	Tm 1.25	Yb 1.10	Lu 1.27		
		Ac 1.10	Th 1.30	Pa 1.50	U 1.70	Np 1.30	Pu 1.28	Am 1.13	Cm 1.28	Bk 1.30	Cf 1.30	Es 1.30	Fm 1.30	Md 1.30	No 1.30	Lr 1.30		

Figure 1. 7: Periodic table belong to Heusler family; X<sub>2</sub>YZ & XYZ

ray diffraction [59]. After successful investigation of such alloy experimentally, researcher linked their magnetic and chemical properties as well as established their compositional ratio.

In the last few decades, Co-based Heusler alloys produced interest among the researchers. So the attempt was done by Webster *et al*, in 1970, to examine their magnetic and chemical properties of Co<sub>2</sub>MnX with X= Ga, Si, Ge, Sn, Sb, and Al [61]. The main features that differentiate Co-based alloys from Ni and Cu based alloys are due to high saturation magnetization and high Curie temperature. Which produce serious attention due to its numerous practical application especially in spintronics devices. Heusler family is predicted to show the behavior of half-metallic ferromagnetic [42]. Kubler *et al*, analyzed the electronic structure of Co<sub>2</sub>Mn (Sn, Al) that show the minority spin states at Fermi energy (E<sub>f</sub>) almost vanish and majority spin density of states only contributes at Fermi energy (E<sub>f</sub>) level [62]. The prediction of half-metallicity in Heusler family, Co-based Heusler alloys has produced special attention for the researcher in both theoretically and experimentally field.

### 1.7.1. Structural Properties of Heusler Alloys

Heusler family are generally synthesized by ternary and quarterly atoms, which are classified into two main groups; Full Heusler alloy with a composition of X<sub>2</sub>YZ, indicated by L<sub>2</sub> structure and that can be possible to leave one position among four sub-lattices unoccupied called Half or semi Heusler alloy with a composition of XYZ that is indicated by C1<sub>b</sub> structure. X and Y belong to transition metal and Z belong to 'sp' atoms (III-V) in the periodic table.

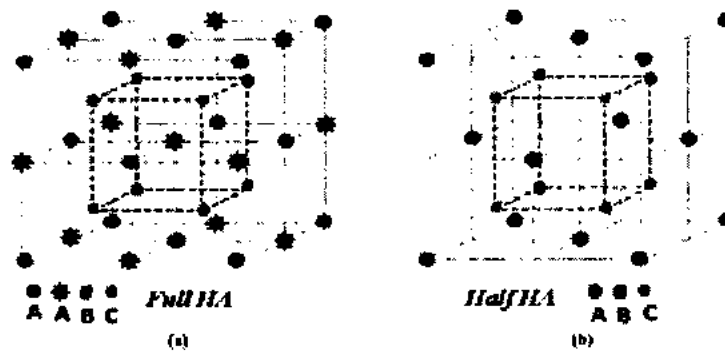


**Figure 1. 8:** Full Heusler Structure (L21) and Half Heusler Structure (C1b) respectively

The lattice point or Wyckoff position of Full Heusler alloys  $(0, 0, 0)$  and  $(1/2, 1/2, 1/2)$  are occupied both by X-atoms, while  $(1/4, 1/4, 1/4)$  and  $(3/4, 3/4, 3/4)$  positions of lattice point are occupied by Y and Z atoms respectively. In the case of half Heusler, one of the lattice position of X atom become vacant. In general, unit cell of the full and half Heusler alloys crystal structure is shown in Fig. 1.8

For example, Co-based alloys such as  $\text{Co}_2\text{Mn}$  (Al & Sn), both the Co atoms fill the position of X- lattice point, whereas Mn fills the position of Y-atom and Al or Sn atom fill the position of Z-lattice point. The structure analysis of such full Heusler alloy, it is clear that each Mn or sp (Al or Sn) atom occupy the symmetry of octahedral with the position of eight Co atoms as the nearest position, and every Co atom occupy four sp and four Mn atom with the first neighbors to form the symmetry of tetrahedral [63].

### 1.7.2. Half-Metallic Ferromagnetism

In 1983, the concept Half-metallic ferromagnetism was introduced first time in Heusler alloys (NiMnSb) by de Groot *et al.* According to their theoretical approach, such Heusler alloy behave as Half-metallic ferromagnetism due to full spin polarization on basis of band structure calculations [42]. Here, “the minority spin electrons behave as a semiconductor, whereas majority spin electrons act as metallic behavior”. The materials or alloys having such characteristics were known to be ‘half metal’. This is because the charge carrying current would be only one spin direction. That produced the spin-polarized transport properties in a pure half-metallic material which contribute 100% spin-polarized character. Up to present numerous Heusler alloys (half and full Heusler) have been predicted theoretically and experimentally to be half-metallic ferromagnetism [63, 64]. Mathematically the electron spin polarization at fermi level is written in Eq-1.1 as;



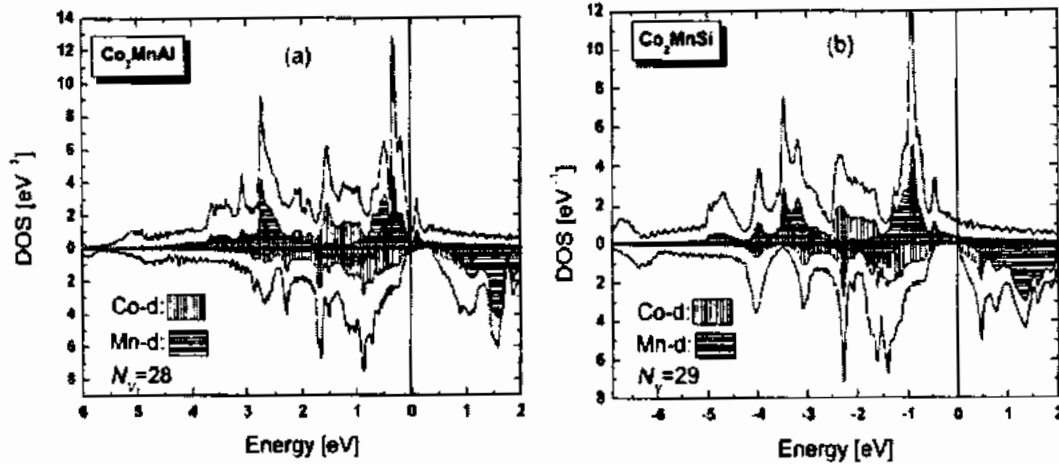


Figure 1. 9: Calculated spin density of states for various Co-based Heusler alloys as described

$$\text{Spin polarization } (P) = \frac{N\uparrow(E_f) - N\downarrow(E_f)}{N\uparrow(E_f) + N\downarrow(E_f)} \quad 1.1$$

Where  $N\uparrow$  and  $N\downarrow$  indicate the density of state up and down at fermi level respectively. If  $N\uparrow(E_f)$  or  $N\downarrow(E_f)$  equal to zero then the spin polarization of electrons will be equal to 100%.

### 1.7.3. Origin of the Band Gap in Heusler Alloys

Galankis *et al.* [73] have specified the cause of band gap in the minority density of states (DOS). They suggested that valance electrons of d-shell as covalent hybridization between the transition metals arises the gap called band gap. In full Heusler alloys where the structure are interpenetrating fcc along the body diagonal that arrange in an X-Y-X-Z.

Several researchers explain the impact and the role of sp atoms in the hybridization. Such as Galankis *et al.* mentioned that in half Heusler alloy (NiMnSb) that sp atoms in the majority states play a vital role to specify the location of a gap at Fermi level due to p and d states of transition metals through hybridization [63]. The shift of bands can damage the half mantellic character in Heusler alloys by exchanging the sp atom. Just as, Co-based full Heusler alloys with chemical composition  $\text{Co}_2\text{BC}$  (Whereas B= Fe & Mn and C= Al or Si), Kandpal *et al.* have presented that production of distinct moments at both Co and (Mn, Fe) sites due to the existence of sp atoms [65]. They observed that the sp atoms with increasing order of valance state, just by replacing Al with Si be able to affect an increment in localized moments on Co and B (Mn & Fe)

## 1.8. Factors Affecting on Disrupting Half-Metallic Ferromagnetism

Co-based Heusler alloys are expected to be a half-metallic ferromagnetic character with large Curie temperature and possess high saturation magnetization which makes them smart and attractive material used in spintronic devices; such as anisotropic magnetoresistance (AMR), giant magnetoresistance (GMR) and tunneling magnetoresistance (TMR). With Maximum spin polarization up to 100% which is an ideal for half-metallicity, that probably to play role in magnetic tunnel junctions (MTJ). But experimental researcher predicted that such spin polarization is difficult to attain as expected by theoretical researchers [66]. Rajnikanth *et al.* using the technique of point contact Andreev reflection technique (PCAR), observed that  $\text{Co}_2\text{MnAl}$  full Heusler alloys with  $L2_1$  type structure have spin polarization up to 60% [66]. Recently Yamamoto *et al.* observed that the chemical composition of  $\text{Co}_2\text{MnSi}/\text{MgO}/\text{Co}_2\text{MnSi}$  alloy showed that tunnel magnetoresistance (TMR) value enhanced with the increment of Mn concentration [67]. These factors predict the selection of Co-based alloy for the half-metallic character which bound the range of half-metallicity that must be essential to understand properly. In literature different researcher (theoretical and experimental) have advised various factors that affect the spin polarization. Some are discussed below.

### 1.8.1. Structural Disorders

The full and half Heusler family shows half-metallic ferromagnetism which is sensitive its crystal structure either order, partially disorder or fully disorder form. If all the four atoms in full Heusler alloys are occupied in their respective lattice position then it forms full order crystal structure indicated by  $L2_1$ , while in half Heusler, if all the three atoms are positioned at their respective lattice point then it shows full order crystal structure indicated by  $C1_b$ . In  $L2_1$  structure, if X-atoms are placed at their respective order form and Y-Z atoms are exchanged their position randomly with respect to each other than such structure leads to B2 type disorder. Similarly when both X-atoms are partially exchanged with Y and Z-atoms with an equal probability, then such disorder is termed as  $\text{DO}_3$  type structure. Also when all four sub-lattice positions of atoms in full Heusler alloys are exchanged randomly then it transformed to A2-type disordered structure as shown in Fig.1.10 [61, 68].

All of these disorders (B2,  $\text{DO}_3$  & A2) in Heusler family play a vital role that is influenced on the spin-dependent electronic structures [69]. Picozzi *et al.* have reported that

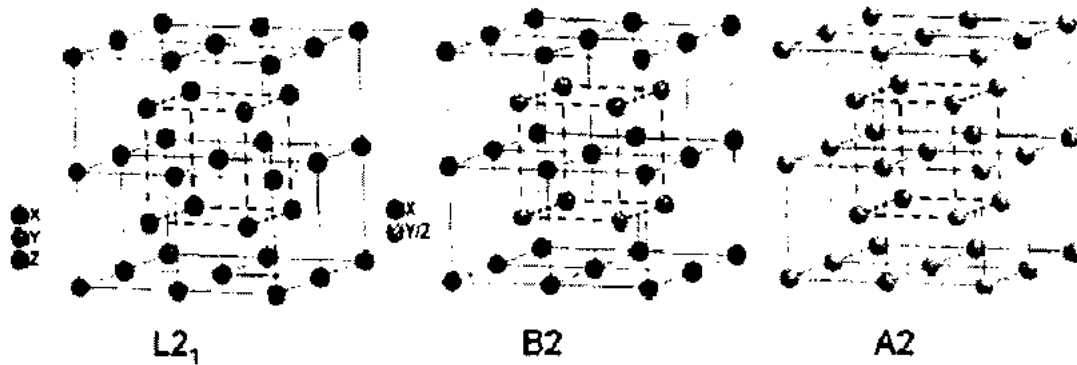


**Figure 1. 10:** shows the Full Heusler order structure ( $L2_1$ ), partially disorder with Y-Z (B2) atoms and full disorder with X-Y & X-Z (A2) atoms

the disorder of the Co atom in  $Co_2MnSi$  full Heusler alloy effect on their half-metallic ferromagnetism [69].

### 1.8.2. Temperature Effect

It has been observed that temperature ( $T > 0$ ) which plays a vital role in the reduced half-metallic character due to depolarization of spin properties [70]. In such circumstances, different feasible mechanisms have been recommended to examine the effect of thermal on spin polarization. The thermally activated spin mixing has been suggested by Skomski *et al.* [70]. Such mixing of the spin down and spin up states that totally deviate the features and characteristics of the states. According to them, the two spin channels having resistance ratio that varies from infinity to some predictable digit. So that the half-metallicity is restricted to zero temperature.

## 1.9. Magnetic Properties of Full Heusler Alloys

The phenomena of ferromagnetism in Co and Fe based Heusler alloys was observed by means of their infrequent electronic structure is changed from the materials that are a typical ferromagnetic character. The magnetic character originates from ordinary ferromagnetic materials (Fe, Co & Ni) by means of unpaired electrons that filled partially their inner shell. During the spin-orbital interactions in such normal ferromagnetic materials can produce non-integer value of their magnetic moments. So the Heusler alloys comprising of three or four (half or full Heusler) different elements among them one belong to the non-magnetic character to behave like an integer magnetic moments. Heusler alloys possess such significant features that are originated from band gap as explained above.

Another very important factor for selection of Heusler alloys before synthesis is the magnetic moment that can be estimated by using Slater-Pauling Rule.

### 1.9.1. Slater-Pauling Rule

The Slater and Pauling have given the basic idea to estimate the magnetic moment of Heusler alloys on the basis of valance electrons. The magnetic moment  $m$  of the 3d elements and their alloys can be assessed by means of average valance electron number ( $N_V$ ) per atom [71, 72].

So in minority bands which are fully occupied [63]. The overall magnetic moment of half Heusler ( $C1_b$ ) with three atoms per formula unit. Then Slater-Pauling rule can be written in Eq-1.2 as;

$$m_{XYZ} = N_V - 18 \quad 1.2$$

Whereas  $N_V$  indicates the total valance electrons. As the total number of valance electron can be calculated; by adding the total number of spin down and spin up electrons as shown in Eq-1.3.

$$N_t = N_{\uparrow} - N_{\downarrow} \quad 1.3$$

In short, the total magnetic moment can also be calculated by using the formula which is given in Eq-1.4& Eq-1.5.

$$M_t = N_{\uparrow} - N_{\downarrow} \quad 1.4$$

OR

$$M_t = N_V - 2N_{\downarrow} \quad 1.5$$

In the case of full Heusler ' $X_2YZ$ ' ( $L2_1$ ), there are four atoms per unit cell leading to the generalized Slater-Pauling formula (Eq-1.6);

$$m_{X_2YZ} = N_V - 24 \quad 1.6$$

Here 24 indicate the sum of completely occupied minority states and majority states in such Heusler alloy, which shows that double the value of minority occupied states.

According to the Slater- Pauling rule, it gives the integral value of the total magnetic moment. Although in full Heusler (quaternary) alloys, the total magnetic moments can be the value in non-integral form because of it occupy some non-integral site even though it behaves as a half-metallic character as well.

### 1.9.2 Magnetocrystalline Anisotropy

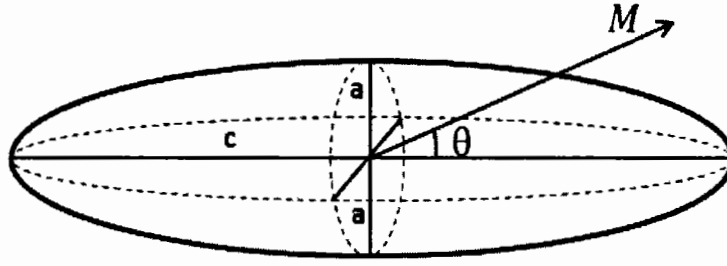


**Figure 1. 11:** Schematics prolate spheroid's for shape anisotropy

The magnetocrystalline anisotropy phenomena can rise in the crystalline specific materials. Hence the atoms are magnetized more energetically in a certain preferred direction. Such directions are correlated by the crystal lattice through principle axis. The cause of magnetocrystalline anisotropy is due to mutually magnetic dipoles interaction and the crystal electric field couple on the spin electron orbital. Generally, the energies of such anisotropy are expressed in the power of conies. So, the magnetocrystalline anisotropy energy for the crystal of hexagonally close packed shape can explained as [73]

$$E_{MC} = K_0 + K_1 \sin^2 \theta + K_2 \sin^4 \theta \quad 1.7$$

Where  $K_0$ ,  $K_1$  and  $K_2$  are the constant of anisotropy, whereas  $\theta$  is the angle between magnetization direction and c-axis.

### 1.9.3 Shape anisotropy

The grains with no preferred orientation of the polycrystalline spherical particle due to magnetized equally with same magnitude of applied field in all directions in which magnetocrystalline anisotropy becomes zero. However, the non-spherical geometry shows easy axis along its long axis. Therefore, in NWs, the same (non-spherical geometry) phenomena has been observed. The shape anisotropy of the NWs can be explained with prolate spheroid which is closed to their structure as shown in Fig.1.11

The magnetized components  $M$  of the prolate spheroid perpendicular and parallel to  $c$ , then the  $E_{ms}$  "magnetostatic energy" is written in Eq-1.8;

$$E_{ms} = \frac{1}{2} [(M \cos \theta)^2 N_c + (M \sin \theta)^2 N_a] \quad 1.8$$

Where  $N_a$  and  $N_c$  are the coefficient of demagnetization along a and c axis respectively. We have  $\cos^2\theta = 1 - \sin^2\theta$ , then above Eq-1.9. Become;

$$E_{ms} = \frac{1}{2}M^2N_c + \frac{1}{2}(N_a - N_c)M^2\sin^2\theta \quad 1.9$$

The angle dependent term in  $E_{ms}$  is same in form as in the crystal of anisotropy energy. The long axis of such geometry shows easy axis of the crystal

For prolate spheroid, the shape anisotropy constant  $K_S$  can be written in Eq-1.10 as;

$$K_s = \frac{1}{2}M^2(N_a - N_c) \quad 1.10$$

However, if the long axis shrinks equal to its short axis then shape anisotropy become disappear.

#### 1.9.4 Magnetic Anisotropy in Nanowire Arrays

In one-dimensional (1-D) NWs, due to magnetostatic dipole interaction that develop an anisotropic behavior among the NWs that change easy axis from long to short axis. Hence the overall effective anisotropy behavior in the 1-D NWs contributed by three main anisotropy field: magnetostatic dipole interaction field, magnetocrystalline anisotropy field and the shape anisotropic field. If the external field is applied parallel to the long axis of the NWs, then total field may written in Eq-1.11;

$$H_0 = 4.2M_s\pi r^2 \frac{L}{D_c^3} \quad 1.11$$

Here  $D_c$ ,  $r$  and  $L$  are the inter-wire distance, radius and length of the NWs. However if the external field is applied perpendicular to the NW, then sum of dipole field and demagnetization field are calculated by the Eq-1.12

$$H_{90} = -2.1M_s\pi r^2 \frac{L}{D_c^3} + 2\pi M_s \quad 1.12$$

Hence the overall effective anisotropy ( $H_K$ ) is expressed in numerically by the Eq-1.13

$$H_K = -6.3M_s\pi r^2 \frac{L}{D_c^3} + 2\pi M_s + H_{mc} \quad 1.13$$

#### 1.10. Density Functional Theory

Density functional theory (DFT) is a computational modelling method [74] based on quantum mechanics and used to investigate the electronic structure [75] of many body systems,

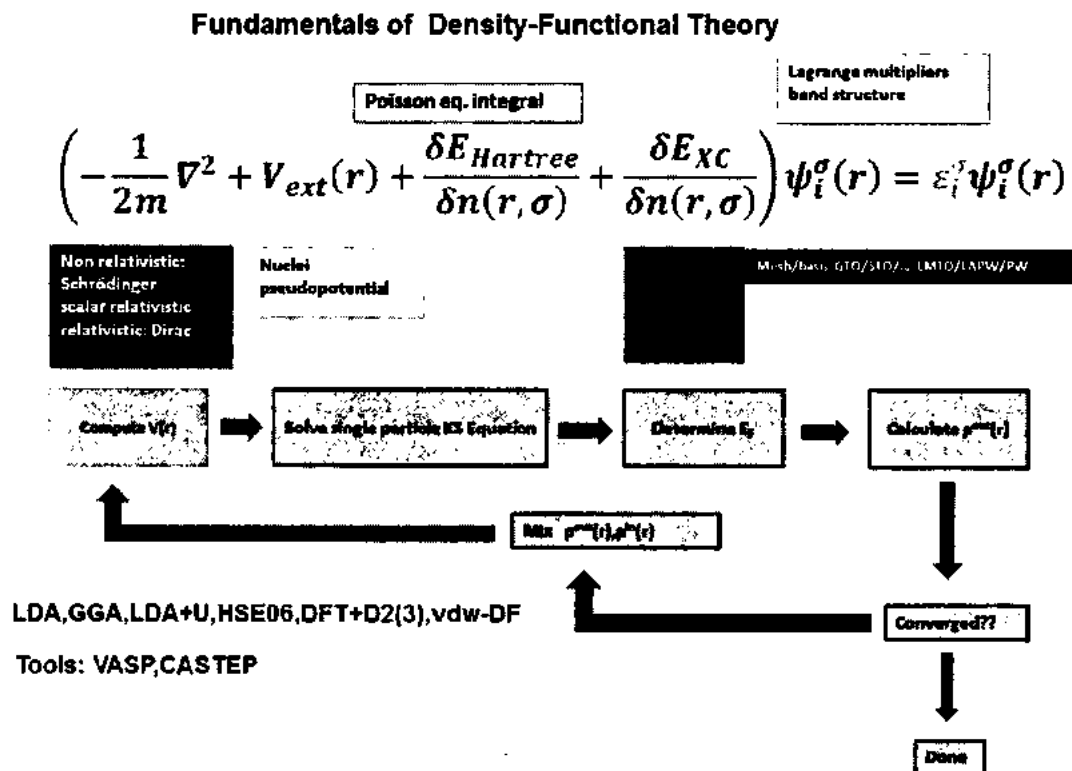


Figure 1. 12: Schematics diagram for Kohn–Sham equations

particularly for atoms molecules. By using this method the properties of many-electron system can be investigated by using functional. Electron density is the basic function of density functional theory (DFT). The computational costs are quite low as compared to traditional methods. We have used the program package WIEN2K to perform electronic structure [76] and magnetic properties of Heusler alloys [77]. The program code is based on full linearized augmented plane wave methods (FP-LAPW) [78].

We can express the-undefined exchange– correlation energy functional in some useful way. That is involved in finding minimum energy solutions of the total energy functional. Nothing we have presented so far really guarantees that this task is any easier than the formidable task of fully solving the Schrodinger equation for the wave function. This difficulty was solved by the great Kohn and Sham, which were awarded by Noble prize in 1998. That showed the task of finding the right electron density can be expressed in a way that involves solving a set of equations in which each equation only involves a single electron. The Kohn–Sham equations have the form.

The main difference is that the Kohn–Sham equations are missing the summations that appear inside the full Schrodinger equation. This is because the solution of the Kohn–Sham equations are single-electron wave functions that depend on only three spatial variables.

### 1.11. Motivation of the Thesis

Presently material scientists show their interest in the spin-dependent current (spintronics) or magneto-electronics along with charge transfer through which information was carried out. These conventional charges along with the spin-dependent electronic devices that enhance their effects such as low energy consumption, non-volatility for magnetic random-access memories also increased their integrate densities and data processing speed. So in the electronics field, through such approach towards novel materials having large Curie temperature, provided that to control, precise and completely understand the role spin dependent current. The properties of such spin orientation either spin up or down produced maximum spin-polarized current called half-metallic ferromagnetism. The detail explanation of half-metallicity has been mentioned in the above section. Hence the half-metallic material plays a vital role in transport and magnetic based devices, like magnetic sensor, giant magneto-resistance (GMR), tunneling magneto-resistance (TMR) and spin transfer torque (STT).

Co-based full Heusler alloy showed their attraction owing their structure in complex order that stimulates to contribute in the novel area of transport and magnetic properties. Such alloys keep high Curie temperature along with the large value of saturation magnetization. That attracts significant attention towards the scientific and technical field of spintronics. There are numerous types of Heusler alloys that belong to ternary and quaternary phase, which have been expected as a half-metallic character.

In the present case, Co-based full Heusler alloys ( $\text{Co}_2\text{Mn}_{0.5}\text{Fe}_{0.5}\text{Sn}$ ) NWs were fabricated in well align and homogeneous AAO templates according to their estimated diameter and length with control mode through AC-electrodeposition. Such solid structure possess large surface area with desired length and diameter. The magnetic properties of such Heusler ( $\text{Co}_2\text{Mn}_{0.5}\text{Fe}_{0.5}\text{Sn}$ ) showed the field of effective anisotropy that contributed through magneto-crystalline anisotropy, shape anisotropy, and magnetostatic anisotropy field. In NWs the shape anisotropy is dominated that made it a suitable candidate for sensors and perpendicular data storage devices. The  $\text{Co}_2\text{Mn}_{0.5}\text{Fe}_{0.5}\text{Sn}$  alloy NWs enhance such properties in distinction compared with bulk materials or other alloys nanostructure and shape. Up to date



Co-based ( $\text{Co}_2\text{Mn}_{0.5}\text{Fe}_{0.5}\text{Sn}$ ) full Heusler alloy NWs by means of AC- electrochemical deposition is not reported in the literature.

In the next experiment Fe-based Heusler alloy ( $\text{Fe}_2\text{CoSn}$ ) NWs were selected and synthesized through the same technique. In literature, Hongzhi Luo *et al.* in 2012, using first-principles to examine the transport and magnetic properties of 'Fe<sub>2</sub>YZ' novel full Heusler alloy. The literature survey shows that different techniques were used to synthesize Fe-based Heusler alloy nanoparticles and thin-film through an arc-melting, balling milling and molecular beam epitaxy. There is a long list of Fe-based full Heusler alloys, among which some were examined through electrodeposition. Similarly the above experiment, Fe-based full Heusler alloy acquires massive saturation magnetization along with large Curie temperature that shows half-metallic character to produce novelty in spintronic based devices. The half-metallic structure can be confirmed using Slater-Pauling [ $M = (N_V - 24)\mu_B$ ] rule, where M and  $N_V$  are total magnetic moment and sum of the valance electrons of the alloy respectively.

Presently, the permanent magnets with large coercivity and high energy density are obtained from the alloy the alloy of rare-earths with 3d metals, although their thermal stability is limited and low magnetization compared with ferromagnetic, 3d transition metals such as; Fe, Co, and their alloys. If such composition can succeed large value of coercivity, at that moment all these difficulties and limitations will resolve that are linked through the magnet of the rare-earth elements. To obtain such results, magnetic NWs and nanorods (NRs) produce the shape anisotropy that might be the novel structure for permanent magnets.

Another article in which diamagnetic copper (Cu) has been coupled with iron (Fe) to form composite  $\text{Fe}_{100-x}\text{Cu}_x$  (NWs) that behave as a soft magnetic owing to interfacial exchange. It has been shown some motivating and exciting disparity in structural and magnetic behavior to synthesize  $\text{Fe}_{100-x}\text{Cu}_x$  alloy NWs by using various the concentration of  $\text{Fe}_{100-x}\text{Cu}_x$  in AAO templates deposited through AC-electrochemical process. It shows amazing results of their magnetic and structural properties by means of low dimensional NWs (high aspect ratio) related to bulk complement. Such alloy (FeCu) NWs have their numerous advantages with excellent and low-cost ductility and saturation magnetization as well as their application in technological devices, for example, catalysis, optics, sensors, electrochemistry and recording media due to vertical storage devices along the easy axis. The choice of AC-electrodeposition in AAO templates to synthesize NWs as it has significant advantages over other fabrication

technique; due to the composition ratio of the deposited alloy can be easily controlled, economical (low-cost) and deposit at room environment with no need of vacuum. The parameters such as; deposition potential, frequency, concentration, pH, current density etc that influence on the structural and magnetic properties on simple and complex structure of Heusler alloys during the AC-electrochemical deposition in AAO templates. All these advantages of AC-electrochemical deposition produced distinguished among the others.

TH03364

---

---

## **Chapter No. 2**

---

---

## Chapter No. 2

### Literature Review

#### 2.1. Anodic Aluminum Oxide (AAO) Templates

In broad sense, the morphology of anodized aluminum oxide (AAO) templates is described through various parameters; the diameter pore, interpore distance, density of pore, thickness of the pore wall, porosity and the thickness of the barrier layer. Hence such morphological parameters of anodic alumina are correlated with the various conditions of anodization; anodizing potential, temperature, the type of electrolyte, current density, purity of anodic aluminum, stirring, and pre-treatment of aluminum. All these parameters are comprehensively explained in the introductory chapter of this thesis. Also In recent time Sulka *et al.* [79] has been explained the above parameters in their review article.

##### 2.1.1 Basic Stages for the Two Steps of Anodization

The self-order AAO templates were synthesized in 40V of oxalic acid at 0.3 M electrolyte solution by Fukuda and Masuda, as a result of nonhomogeneous and disorder alignments of templates were fabricated [12]. But was extended to second step of anodization, after which uniform, align and well order anodic alumina was formed which they are named as “two step of anodization” [80]. The first step of anodization was carried out in the range of 5 to 24 hrs. Then nonhomogeneous anodic alumina were etched in yellow solution (0.2 M CrO<sub>3</sub>+ 0.5 M H<sub>3</sub>PO<sub>4</sub>) at 60 to 80 °C for 2 hrs to produce the texture of concave like hemisphere [81]. The second step was carried out with same conditions as in first step, so that the nucleation of the AAO templates were occurred at the center of concave texture [11, 82]. To increase the alignment, order and periodicity of AAO templates, one can proceed it to three step of anodization.

##### 2.1.2. Three-Step of Anodization

Three steps of anodization was observed in sulfuric [83] and in oxalic acid [84, 85] with same conditions/parameters that were adopted in in the two steps of anodization. Each electrolyte required different time of anodization for each three steps separately. Such as oxalic acid need 10, 690 and 3 to 4 min for first, second and third step of anodization respectively [84]. It was clearly observed that uniformity, alignment and periodicity in AAO templates was excellent in three steps compared to the two steps of anodization [85, 86]. The influence of multistep (two,

three or even four steps) of anodization on uniformity and periodicity of AAO templates was affected and was clearly observed by Brändli *et al.* [87] that increment of the anodizing steps leads to increase the alignments and periodicity in the pore diameter of anodic alumina.

## **2.2. The Basic Models to Synthesize AAO Templates**

The morphology of AAO templates such as, pore diameter, pore wall, porosity, interpore distance etc, were significantly varied with respect to (w.r.t) concentration and type of electrolyte [88, 89] and also influence with different anodizing conditions [90-92]. The anionic contents are reduced w.r.t the time of anodization because of the concentration of electrolyte decreases in a linear format, although the templates were grown in a steady state, investigated by Han *et al* [93]. This model adopted the linear proportionality between the interpore distance and anodization potential. The support was given to this model of AAO templates by Thamida and Chang *et al.* They linked the same proportionality between anodization potential and interpore distance [94]. They observed that electric field at metal/oxide and oxide/electrolyte on both interfaces was predicted to depend on interfaces geometry. According to their model, the anodization potential was not influenced on the friction of the diameter to interpore distance of the pore of AAO templates but affected by pH of electrolyte [94].

In literature, a number of attempts were done to observe the morphology of AAO templates using different acidic electrolyte, such as phosphoric, sulfuric and oxalic acid to optimize the condition that produced best desired structure (uniform and homogenous) with different pore diameter/interpore distance of anodic alumina. The best results were taken from AAO templates to synthesize NWs, NTs and nanorods. Such AAO templates were synthesized with different acidic electrolytes are; (i) 0.3 M oxalic acid at 40V produced the interpore distance was 102 nm [95-97], (ii) the 0.3 M sulfuric acid at 25V synthesized the interpore distance was 66 nm [12, 95] and (iii) the 0.3 M phosphoric acid at 195 V synthesized the interpore distance was 450 nm [97, 98].

### **2.2.1. Patermarakis And Colleagues Proposed the Growth Models of AAO Templates**

The anodic alumina by various acidic solution were presented in different theoretical models: such as Patermarakis *et al.* [99-108]. Hence various conditions were employed to obtain the kinetic model of such self-assembled AAO templates observed by Patermarakis *et al.* [102-104]. Therefore they proposed the separate model for carrying of charge through the bottom of the barrier layer [107, 108].

According to Macdonald *et al.* the interfaces of oxide/electrolyte produced the vacancies that were expended over the interfaces of metal/oxide. The barrier layer thickness and the current density in a logarithm format must be proportional to the anodization potential in a linear format [109-111].

Another model was proposed by Li *et al.* [84] about the growth formation of AAO templates. In this model they observed that increment of electric field which effect to increase the oxide corrosion and shrinks the thickness of the barrier layer. Similarly in oxalic acid electrolyte (0.3M) at fixed potential grown-up the oxide rate at 1nm/min at different temperature [112].

$$(5^{\circ}\text{C}) \quad R_h = 392.30 - 26.92 U + 0.63U^2 \quad 2.1$$

$$(15^{\circ}\text{C}) \quad R_h = 123.43 - 9.19 U + 0.23U^2 \quad 2.2$$

$$(5^{\circ}\text{C}) \quad R_h = 51.33 - 3.71 U + 0.095U^2 \quad 2.3$$

To measure the oxide growth rate at constant potential in sulfuric acid electrolyte (2.4 M) with one step, two steps and three steps of anodization was observed by Sulka *et al.* [113]. They found no variation in the rate of oxide growth among all three anodizing process experimentally.

## 2.3. Synthesis of Nanowires (NWs)

### 2.3.1. Single Component of NWs

Schwanbeck, *et al.* investigated the effect of different diameter of AAO templates on magnetic properties of Co NWs. They observed that the electrodeposition was employed on galvanostatic condition unless the potential gained constant voltage. After that deposition of such NWs in AAO templates stopped until few of membrane were filled at top of AAO templates. As a result same magnetic properties i.e isotropic behavior, were observed along parallel and perpendicular NWs having diameter equal to 200 nm. But the NWs that were synthesized in 100 nm AAO templates showed the anisotropic behavior i.e the value of coercivity was greater along the plane compared to perpendicular NWs.

The Fe, Co and Ni NWs presented high aspect ratio and magnetically isotropic behavior was examined by Sellmyer *et al.* In ferromagnetic NWs, Fe shows maximum coercivity (3000 Oe) among Co and Ni. Whereas Ni displays minimum coercivity (950 Oe) and Co shows the intermediate result (2600 Oe).

### 2.3.2. Binary Alloys NWs

The significance of the combination of magnetic with nonmagnetic alloy NWs, such as CoCu alloy NWs was synthesized in anodic alumina with different pore diameters. Such alloy was synthesized by Blythe *et al.* (in 2000) with 20 and 200 nm of AAO templates through electrochemical deposition process. The anisotropy was observed during demagnetization of CoCu alloy NWs. In 2001, Sellmyer *et al.* studied that coercivity was linearly improved by the addition of Fe concentration in FeNi alloy NWs. They also observed that decrement of coercivity in FeCu alloy NWs by the increase of Cu contents.

### 2.4. Heusler Alloy

Presently in physics, the researcher focused their attention towards new class family called Heusler, which is linked with 100 years (in 1903) back, that Fritz Heusler discovered the  $\text{Cu}_2\text{MnAl}$  composition behave as a ferromagnetic although all of the three elements were non-ferromagnetic [114].

Since such alloys motivated the researcher because of their specific structure to tune the electronic properties stretching from half- metallicity [62, 115] to ferrimagnetism [116] above semiconductor of nonmagnetic [117, 118] towards the topological insulators [119, 120]. The family of Heusler alloys was comprehensively studied somewhere else [59]. The explanatory analysis of the data storage by means of Heusler alloys was found in that review article comprehensively.

#### 2.4.1. Cobalt-Based Full Heusler alloy Nanostructures

Hence currently research (experimental and theoretical) of Heusler alloys divert towards Fe and Co-based alloys due to possessing the stability of half metallic ferromagnetism [121, 122]. Initially the large magneto resistance (MR) value [123-125] was observed in Co-based quaternary full Heusler alloys that enhance the function of tunneling magneto resistance (TMR) and giant magneto resistance (GMR) base devices [123, 126]. In 2003 Inomata *et al.* were the first who investigated the experimental evidence of tunneling magneto resistance (TMR) in Co-based ( $\text{Co}_2\text{Cr}_{0.6}\text{Fe}_{0.4}\text{Al}$ ) quaternary full Heusler alloys in the order of B2-type structure [126]. And observed the ratio of MR at room temperature (RT) and at 5K upto 16% and 26% respectively. That produced the experimental evidence and provide path to get large TMR value at room temperature in quaternary full Heusler alloy. Such experiment of full Heusler alloy was proceeded further to synthesize thin film by varying the contents of the alloy

to get the structure of A2 and B2 type of disorder. It provides the base to increase the TMR value through anodic alumina (amorphous) in MTJs by the electrodes of Heusler alloy, such as;  $\text{Co}_2\text{MnAl}$  [127, 128],  $\text{Co}_2\text{FeAl}$  [129],  $\text{Co}_2\text{FeAl}_{0.5}\text{Si}_{0.5}$  [130] and multilayer [131]. The electrode synthesized through Co-based full Heusler alloys was the evidence of high MR values; 8.8 to 10.2% of full Heusler  $\text{Co}_2\text{MnGa}_{0.5}\text{Sn}_{0.5}$  [132],  $\text{Co}_2\text{FeGa}_{0.5}\text{Ge}_{0.5}$  has 41.8% [133] and the maximum value so far 74.7% was observed in  $\text{Co}_2\text{Fe}_{0.4}\text{Mn}_{0.6}\text{Si}$  [134].



---

---

## **Chapter No. 3**

---

---

## Chapter No. 3

# Synthesis Techniques

Recently the nanotechnology attracted the scientists due to their high aspect ratio synthesized with numerous nanostructures through novel materials. Especially, the economical and homogeneous NWs and NTs synthesized through electrochemical deposition technique in the nanopores of anodized aluminum oxide templates (AAO), that is periodically ordered structures with dimension (1-D) less than 100 nm, has produced broad range activities in every field of life particularly in engineering and biomedical research. The enormous development in nanotechnology that allows enhancing the magnetic, catalytic, mechanical and optoelectronic properties in magnetic recording media, sensing devices and functional electrodes due to huge dimensional reduction with the accurate switch of their surface geometry [135]. Besides, anodize alumina itself observe several motivating and remarkable properties due to their unique and variable structure to synthesize nanotubes and NWs (1-D nanostructures) of different geometry.

### 3.1. Effect of Applied Conditions on Geometry of Anodized Aluminum Oxide (AAO) Templates

Anodized aluminum oxide (AAO) templates are synthesized in various electrolytes solution among three of them is commonly used in control conditions; phosphoric acid, oxalic acid and sulfuric acid [79]. Scientists have been attracted to examine the quantitative and qualitative effect on the nanopores' geometry by several operative conditions. The operational conditions of each electrolyte is different from others such as anodization voltage, electrolyte concentration, time is taken for the first and second step of anodization and temperature during anodization process effect the geometry of AAO templates like interpore distance, porosity, pore diameter, wall thickness and barrier layer thickness, also different electrolyte have different ranges of voltage. In the case of sulfuric acid, the anodization voltage was taken in the range of 15 to 25V [136]. The voltage cross such limits, result in the dissolution of anodic alumina and no porous geometry can be achieved. The AAO templates with a large pore diameter can be synthesized in a high voltage anodization. Hence among all, it was observed that Phosphoric acid was selected to synthesize large pore diameter that achieve the maximum 195V. [97, 137] and oxalic acid that ranges from 20 to 100 V [138-147]. To understand such

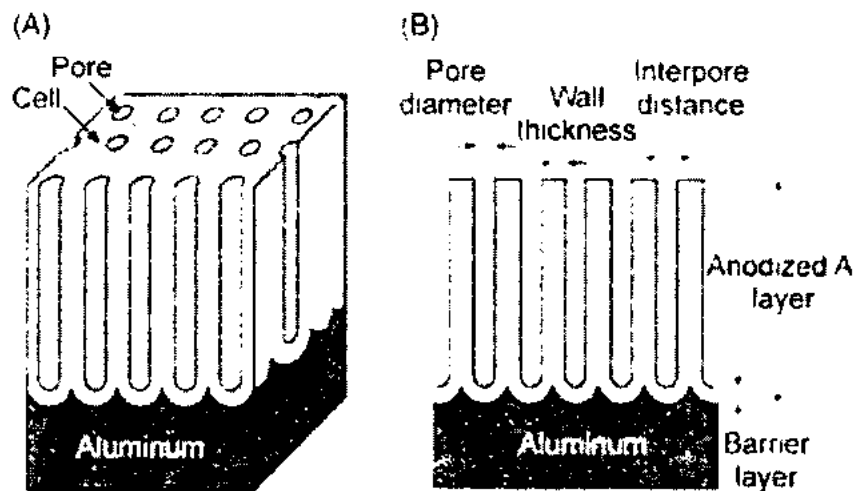


**Figure 3. 1:** (A) Shows the systematically the porous of anodic alumina and (B) shows the side view of the complete structure of alumina

logic, we first review some initial and effective parameters that are affected on AAO templates as shown in Fig.3.1.

### 3.1.1. Pore Diameter of AAO Template

The pore diameter of AAO templates is directly proportional to the anodization potential as given in Eq-3.1 such that  $\lambda_p$  is constant of proportionality equal to  $1.29\text{nmV}^{-1}$  [18].

$$D_p = \lambda_p \cdot U \quad 3.1$$

Here  $D_p$  and  $U$  indicate the diameter of the pore in nm and anodization potential (V) respectively. According to Wood and O.Sullivan observation [18], that pore diameter, wall thickness, interpore distance barrier layer thickness, and  $W_U$  is the wall thickness per volt at a constant potential of anodization can be inter-related with respect to each other as followed in Eq-3.2 :

$$D_p = D_c - 2 \cdot W = D_c - 1.42 \cdot B = D_c - 2 \cdot W_U \cdot U \quad 3.2$$

Here  $D_c$ ,  $W$  and  $B$  indicate the interpore distance, wall thickness and the thickness of barrier layer respectively. All is measured in nm scale. Whereas  $W_U$  measures the thickness of the wall per unit volt (nm). The Palibroda has been reported through Eq-3.3, that the pore diameter mainly dependent on the anodization potential related to their critical potential  $U_{Max}$  [148].

$$D_p = 4.986 + 0.709 \cdot U = 3.64 + 18.89 U/U_{max} \quad 3.3$$

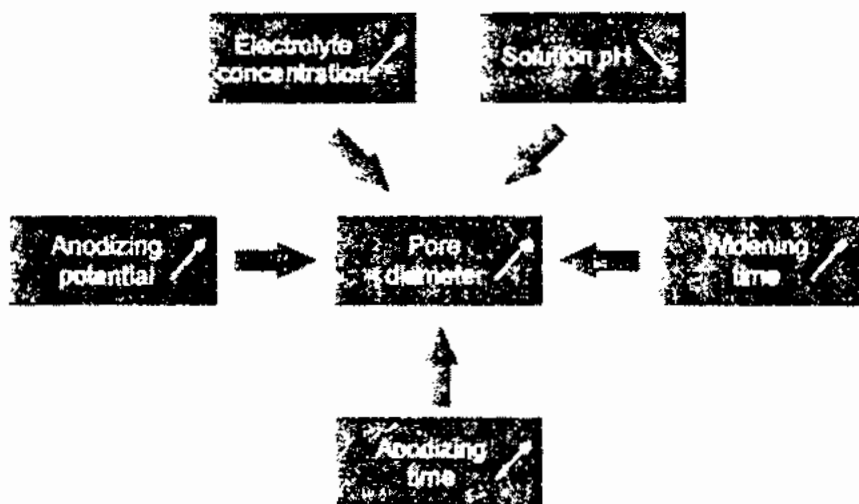


Figure 3. 2: Factor effect on the porous diameter of AAO templates

In the last few decades it has been observed, that the pore diameter of AAO templates has been affected by the pH and temperature of the anodizing solution, i.e. the pore diameter of AAO templates declines by reducing the pH [149] and temperature of the anodizing solution [113]. Also, the influence of the acidic electrolyte concentration is inversely proportional to the pore diameter of AAO templates [97]. In short various parameters that influence on the pore diameter of AAO templates are schematically presented as shown in Fig 3.2

### 3.1.2. Interpore Distance of AAO Templates

In the above discussion, it is clear that interpore distance of anodized aluminum oxide templates is linearly proportional to the anodizing potential through a constant of proportionality as given in Eq-3.4. such that  $\lambda_c$  nearly equal to  $2.5\text{nmV}^{-1}$  [97].

$$D_c = \lambda_c \cdot U \quad 3.4$$

Similarly, Keller et al. also presented numerically to calculate the pore diameter more accurately from the Eq-3.5 [150].

$$D_c = 2 \cdot W + D_p = 2 \cdot W_U \cdot U + D_p \quad 3.5$$

The thickness of the wall of AAO templates is numerically calculated by O.Sullivan and Wood [18] that is almost 71% thickness of the barrier layer. They have proposed the following Eq-3.6

$$D_c = 1.42 \cdot B + D_p \quad 3.6$$

### 3.1.3. The Wall Thickness of AAO Templates

The thickness of the wall of AAO templates can be calculated from the above Eq-3.7 of Keller *et al.* [150]

$$W = D_c - D_p / 2 \quad 3.7$$

During the anodization of aluminum through phosphoric acid, the wall thickness of the AAO templates is proportional to the thickness of the barrier layer as presented by O.Sullivan and Wood [18]. The mathematical form is presented in Eq-3.8.

$$W = 0.71 \cdot B \quad 3.8$$

The proportionality constant in Eq-3.8 slightly varies w.r.t the change of anodization potential, was calculated by Ebihara *et al.* [151]. Hence from 5 to 20V, the proportionality constant of Eq-3.8 was changed from 0.71 to 0.66. Similarly, the proportionality constant is gradually increased above 20V and finally it attained 0.89 at their critical (maximum) anodization potential.

### 3.1.4. Thickness of the Barrier Layer of AAO Templates

As in the above discussion, it is clear that barrier layer thickness is directly proportional to the anodization potential. That has been calculated theoretically in the range of 1.3 to 1.4nmV<sup>-1</sup> [152].

### 3.1.5. Porosity

Porosity is the ratio of the pores occupied of the surface area to the full area of the surface as given in Eq-3.9.

$$\text{Porosity} = \frac{S_{\text{pores}}}{S} = \frac{S_p}{S_h} \quad 3.9$$

The porosity of the anodized alumina mainly depends on acidic electrolyte to the dissolution of oxides and the rate of growth oxides. Also, the density of the porosity depends upon the anodization condition; the electrolyte concentration, temperature during anodization, nature of acidic electrolyte solution and duration of the first and second step of anodization. But the utmost significant and valuable factor is the pH of the acidic electrolyte solution and the anodic potential.

If we suppose that pore of each template is exactly in the circular nanostructure, then the pore area ( $S_p$ ) and whole surface area ( $S_h$ ) can be developed further as in Eq-3.10 and Eq-3-11;

$$S_p = \pi \cdot \left(\frac{D_p}{2}\right)^2 \quad 3.10$$

$$S_h = \frac{D_c^2 \cdot \sqrt{3}}{2} \quad 3.11$$

So the put Eq-3.10 and Eq-3-11 in Eq-9 we get Eq-3.12;

$$Porosity = \frac{\pi}{2\sqrt{3}} \left(\frac{D_p}{D_c}\right)^2 = 0.907 \cdot \left(\frac{D_p}{D_c}\right)^2 \quad 3.12$$

The porosity with hexagonal nanostructure arrays were calculated by Ebihara *et al.* in Eq-3.13 [151].

$$Porosity = 10^{-14} n \cdot \pi \cdot \left(\frac{D_p}{2}\right)^2 \quad 3.13$$

Here 'D<sub>p</sub>' indicates the diameter of the pore (AAO templates) in nm scale and 'n' shown the density of alumina (total numbers of pores/cm<sup>2</sup>).

### 3.1.6. The Pore Density of AAO Templates

The pores density of AAO templates is the overall amount of pores occupying 1 cm<sup>2</sup> surface area.

$$n = \frac{10^{14}}{P_h} = \frac{2 \cdot 10^{14}}{\sqrt{3} \cdot D_c^2} \quad 3.14$$

Put Eq-3.4 in Eq-3.14 we get:

$$n = \frac{2 \cdot 10^{14}}{U^2 \cdot \sqrt{3} \cdot \lambda_c^2} \approx \frac{18.475 \cdot 10^{12}}{U^2} \quad 3.15$$

## 3.2. Pre-Treatment of Aluminum Foil before to Start Anodization Process

There are few steps before to start anodization called Pre-treatment. These steps produce a great influences on the periodicity, homogeneity and uniformity of anodized aluminum oxide (AAO), which are briefly explained below.

### 3.2.1. Pre-Treatment of Aluminum Foil

The selection of the aluminum due to its purity is an important and primary factor that influences on the result. Also before to start the anodization process, pre-treatment of aluminum played a vital role that effects on the morphology of self-synthesized anodized aluminum oxide (AAO) template.

### 3.2.2. Heat (Annealing) treatment

After select the substrate, the annealing treatment is then proceeded, so that on the surface of substrate stresses are reduced which enhance the average grain size. Generally, the aluminum substrate is annealed at 500 °C under nitrogen atmosphere for 4 to 5hrs [153, 154].

### 3.2.3. Degreasing of the Aluminum Foil

Before anodization, degreasing of aluminum is an important step that influenced on the morphology of anodic alumina. The aluminum is immersed for the 60sec in the aqueous solution of 5% NaOH. After that the mix solution of H<sub>2</sub>O + HNO<sub>3</sub> (1:1), the aluminum is submerged for 30 to 60sec, that shine the surface of the aluminum [11, 155-157]. Somewhere else in literature methanol and benzene [158] trichloroethylene [159] dichloromethane [9] and acetone or ethanol have been used separately to clean up the surface of aluminum. But the most effective solution for the degreasing of the aluminum sample is the mixture of HCl+HNO<sub>3</sub>+HF+H<sub>2</sub>O (20:10:1:69). All of the above solutions are significantly effective for the self-organized of anodic alumina that is highly ordered, uniform and homogenous [95].

### 3.2.4. Electrochemical Polishing of the Surface of Aluminum Foil

The purpose of electropolishing is to make the surface smooth and mirror shine, so that to synthesize homogenous and highly order AAO templates. Hence the aluminum foil is electrochemically polished through perchloric acid (HClO<sub>4</sub>): Ethanol (CH<sub>3</sub>CH<sub>2</sub>OH) =1:4 for 150 to 200sec at room temperature under 9V (dc). After electropolish, the aluminum foil has been properly rinsed through distilled water so that the acid solution completely is removed and produced no hurdle during the two-step of anodization.

Among all, pre-treatment for surface polishing, an electrochemical method having the mixture of perchloric acid and ethanol was explained in detail elsewhere [160]. Hence the effect of electrochemical polishing on the morphology of AAO templates throughout anodization was also observed [154, 161, 162]. The surface of anodic alumina behaves as a hexagonally with regular and homogenous structured along with miller indices of Al (100) and Al (111).

## 3.3. Brief Survey to Synthesize AAO Templates using Two Steps of Anodization Technique

### 3.3.1. First Step of Anodization

The first step of anodization after pre-treatment of aluminum foil, one can select the electrolyte solution; either phosphoric, oxalic or sulphuric acid, to fulfill their desired goal. As each

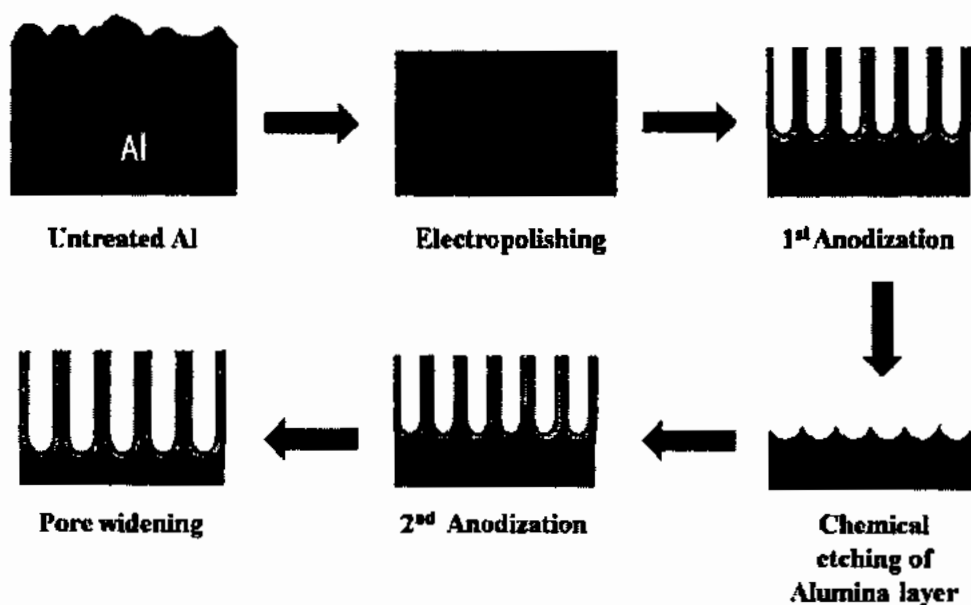


**Figure 3. 3:** The experimental procedure for a two-step self-organized anodization

electrolyte needs different anodization potential, time, temperature and concentration that must be influenced on their results. Generally, we use 5% phosphoric solution by applying 60V DC at temperature between 2 to 5 °C for 5hrs with continuous magnetic stirring to maintain the electrolyte solution homogeneous. But after completion the first step, the morphology of anodic alumina has not homogeneous with uniform ordered. Hence to produce uniformity with proper order that greatly influenced on our results, then dip the sample in a yellow solution for heat treatment to remove non-uniformly anodic alumina. The whole steps of AAO templates are illustrated in Fig.3.3 as explain below.

### 3.3.2. Heat Treatment

After the first step of anodization, the non-periodic structure of AAO templates has been synthesized. So to synthesize AAO templates in a periodic pattern, we must remove the non-periodic templates. For such circumstances, we dip our sample in yellow solution, which is the mixture of 6 wt% of phosphoric acid and 1.8 wt% of chromic acid and kept at 60 °C for 2hrs. After completion the heat treatment, it must be washed with distilled water for a number of times so that no drops of the yellow solution are attached to the sample.

### 3.3.3. Second Step of Anodization

After heat treatment in a yellow solution, then second step of anodization was proceeded to synthesize uniform and homogeneous AAO templates. All parameters/conditions is kept



similar as in the first step of anodization, only the time duration is increased from 5hrs to 20hrs. The duration of time is directly proportional to the length of the synthesized AAO templates. The selection of electrolyte, all the conditions and the parameters that effect the morphology of AAO templates is discussed below along with their mathematical expressions.

### 3.4. Factors Determining the Morphology of PAA Structures

During the anodization process, different parameter that influenced on the morphology of AAO templates such as; the type of electrolyte, the concentration of the electrolyte, anodization potential, temperature and the pH of electrolyte [10, 11, 97, 163-168]. It is cleared that pore diameter and interpore distance of the self-synthesize AAO templates that directly proportional to the anodizing potential through an approximate constant in the range of 2.6 to 2.9 nm/V. On the basis of a number of the experimental results, the barrier thickness has been predicted to be half numerical value relative to interpore distance [10, 11, 163]. The selection of electrolyte such as oxalic, sulphuric or phosphoric for self-synthesis of AAO templates is restricted according to their desired results. Typically the use of sulphuric acid is to obtained the AAO templates with less pore diameter and interpore distance. Because of in such electrolyte the templates are synthesized at low anodizing voltage (15 to 30V). Whereas the phosphoric acid is used for the maximum anodizing voltages (100 to 195V) to get large diameter AAO templates and the oxalic acid has been used for intermediate anodizing voltage up to 30 to 65V. The differences in their conductivity that produced variations in their anodizing voltages. Such as the conductivity of sulphuric acid is the highest among the other two acids. Hence for such acid, if the anoding voltage is used greater than 30V can breakdown the oxide layer and may have produced leakage in the sample.

That way the anodization of aluminum in phosphoric acid synthesized large pore diameter due to its highest pH value compare to the other two acids [10, 11, 163, 166-168]. To control the current and to prevent the oxide structure during the anodization process, the temperature should be adjusted in the range of 1 to 5°C (below 6°C). But it has been observed that at low temperature the growth rate of AAO templates is decreased [163, 166].

It has been observed that the morphology of anodic alumina was affected by some other parameters, such as to select the pure aluminum (almost 99.99%), pre-treatment that has been used before to start the anodization process such as; to anneal the sample for several hours up

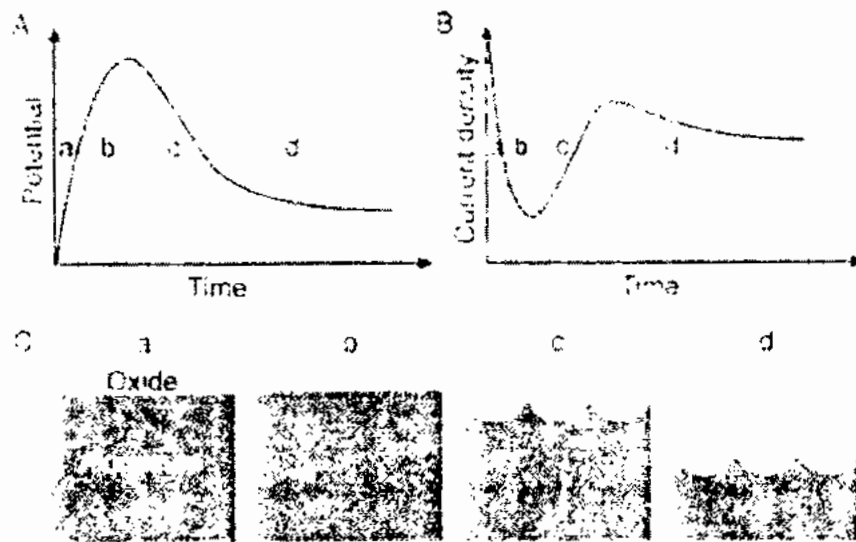


**Figure 3. 4:** (A) Graphical representation of the anodizing growth of alumina in Galvanostatic condition and (B) Potentiostatic condition, (C) Overall stages through anodic alumina oxide established

to 400 to 500°C, electropolish the sample chemically, stirring vigorously that eject heat and produced homogeneity in the solution during the anodization [12, 163, 169, 170].

### 3.5. Removal of the Aluminum Base

After completion the second step of anodization, the substrate of aluminum can be separated from anodic alumina in the electrochemical etching process using HCL 20% with 1 to 5V (dc)[171]. The most extensive and vigorously method to remove the oxidized aluminum from unoxidized aluminum using a wet chemical process. In such technique, the whole sample is immersed in mercuric chloride ( $\text{HgCl}_2$ ) solution, in which it dissolved the unoxidized substrate of aluminum in 1to 2hrs depend upon the concentration of mercuric chloride [83, 172, 173]. The  $\text{CuSO}_4/\text{HCl}$  solution was also observed to remove the oxidized anodic alumina from unoxidized alumina which needs excessive attention and care as compared to other technique [174].

#### 3.5.1. Extraction of the Barrier Layer and Pore Widening

It is necessary to remove completely or partially the barrier layer from AAO templates for the electrochemical deposition. In literature various methods are mentioned through which barrier layer is removed to produce conducting path for electrochemical deposition such as Cathodic polarization [175-177] and Voltage drop method [13]. But the commonly, easy and cheap

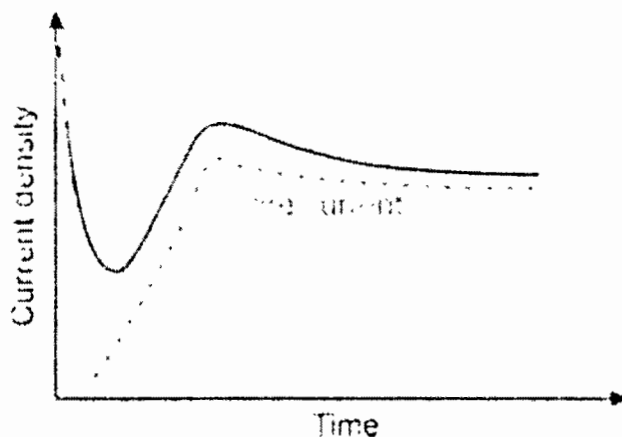


**Figure 3. 5:** Schematic diagram with constant anodizing show overlapping process during the growth of AAO templates

technique for self-organized anodic alumina that we have used in our experiment is the voltage drop method. Also, the pore can be opened and widened by immersing the oxidized alumina in the aqueous solution of phosphoric acid ( $H_3PO_4$ ) for 30 to 40 min, so that the desired materials can be deposited easily. Xu *et al.* [178] observed that the diameter of the AAO templates can be tuned through varying the chemical etching time in the solution of phosphoric acid.

### 3.6. Anodization and Potential/Current-Time Transient

It is necessary to record the potential-time transient graph and current density-time graph during the anodization of the first few minutes. It confirmed the regularity, homogeneity, and uniformity shape formation of the AAO templates. Both potential and current-time transit graph of 20%  $H_2SO_4$  below  $5^\circ C$  is illustrated in Fig.3.4:

The growth of anodic alumina during the anodization at constant applied current as shown in Fig.3.4 (A). Initially linear increase in potential with respect to the time, unless it reaches to their maximum value. And then slowly declined to achieve their steady state. Initially the linearly increased in potential (at stage a) shows the uniform growth of oxide thin film at the bottom of AAO templates. An additional increased in potential (at stage b) results in pores formation at the thin film of the barrier. At maximum potential (at stage c) after which it dropped slowly to breakdown barrier and started the formation of pores from the surface of the oxide film. At the end (at stage d) constant current density is achieved which is the sign of steady growth of AAO templates. Whereas at constant potential is shown in Fig.3.4 (B), initially the current density is declined rapidly w.r.t time and reached to its minimum value.

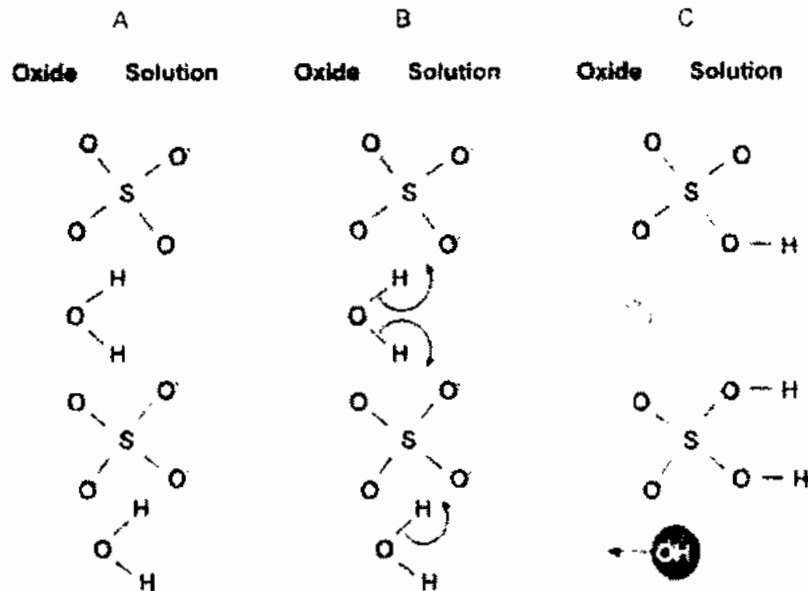


**Figure 3. 6:** Schematic diagram shows the formations of  $\text{OH}^-$  and  $\text{O}^{2-}$  ions at the interface of oxide/electrolyte with  $\text{SO}_4^{2-}$  anions adsorbed due to water interrelating

After that current density rises and attain their peak value, then slightly declined and achieve their steady state indicated the linear formation of AAO templates.

### 3.6.1 Current-Time Graph

The paper of research to synthesize uniform, higher order and homogeneous close-packed AAO templates. The result oriented; pore diameter, lateral length and interpore distance through constant anodization potential instead of current constant. Hence with constant anodization potential, the graph between the variation of current density w.r.t the time was observed by Hoar and Yahalom [179] as shown in Fig.3.5. The two overlapping graph showed that, first current decreases exponentially with the formation of thin film of barrier layer (aluminum oxide), and increase in the second graph that indicate the pore formation.

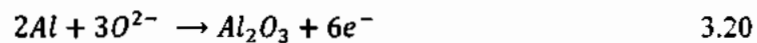
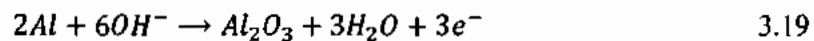
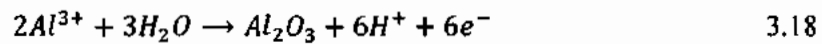
### 3.6.2. Linearly Growth of Anodic Alumina Oxide (Porous)

In literature, very large number of research articles have been presented by the researcher to investigate the formation of AAO templates through anodization of aluminum. But due to the electrochemical process, all aspects related to the formation of AAO templates are not clarified completely up till now. For example, there is an ambiguity that anion species  $\text{O}^{2-}$  carrying by oxygen or in fact  $\text{OH}^-$  ions may be involved in the anodization process. Simply water splits and generates the  $\text{OH}^-$  ions during anodization or dissolved  $\text{O}_2$  through reduction of water by cathode as illustrated in Eq.3.16 & 3.17 given below;



Hence the  $\text{OH}^-$  ions have been absorbed by the annihilation of  $\text{O}_2$  vacancy through which  $\text{O}^{2-}$  ions may be produced at the interface of electrolyte/oxide [180], simply the adsorbed anions interaction from the water splitting process in which  $\text{OH}^-$  can be formed as shown in Fig.3.6 [18].

In the process of anodization (acidic electrolyte) that grown the oxide amorphous film as illustrated in the reaction given below;



The anodic current that played a vital role is given by Eq-3.21;

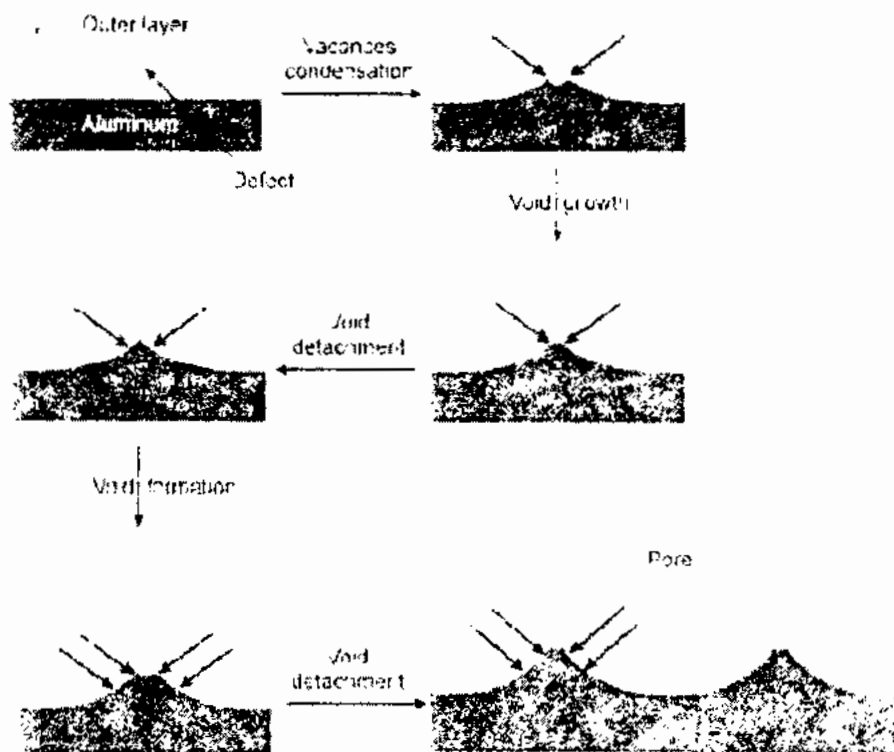
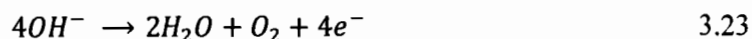


**Figure 3. 7:** Schematic diagrams illustrate the voids production in the porous layer of anodic alumina due to the condensation mechanism of vacancy

Hence in different electrolytes near the interfaces (metal/oxide) liberate oxygen, was reported in the literature which is represented by the following reactions (Eq-3.22 & Eq-3.23);



The transfer of oxygen from electrolyte that contains both  $O^{2-}$  and  $OH^-$  through barrier layer that produced anodic alumina, and  $Al^{3+}$  ions drift towards the oxide film. The ions of  $Al^{3+}$  synthesized the oxide at the boundary of metal/oxide as well as the oxide/electrolyte borders followed by the different condition of anodization [181].

The variation of external field at interfaces affects that influenced on the pore formation rate [182]. The Al-O bonds that started the oxidation because of polarization and the  $Al^{3+}$  ions in the presence of external field was simply removed [18].

### 3.6.3. The Mechanism Using Field-Assisted to Grow AAO Templates

At the interface of the oxide/metal vacancies are formed as soon as the anodization process starts result, in which the ejection of  $Al^{3+}$  due to field assisted into the electrolyte. At the interfaces of metal grains, vacancies begin to start due to condensation that produced a void. From the projection of peak that separated the void growth. Because of beneath the void, corrosion is started that produced the way to nucleates new void on its peak. As the saturation of aluminum that started more quickly through vacancies. So in this way, the growth of new void is started. Hence in a similar way, the repetition of the whole process is begun to start again and again as shown in Fig 3.7 [111].

### 3.7. Y-Branch Shape Multi-Segmented AAO Templates

If the diameter is rapidly changed, the nanoporous of multi-segmented structure is obtained. According to Lee *et al.* 2006 [183], such modulated AAO templates that are periodic in shape as shown in Fig.3.8, as the demand of nanotechnology. Moreover, the branched shape AAO templates like Y-shape nanostructure is synthesized by a rapid change in their anodizing voltage. In literature using oxalic acid, Y-shaped nanostructure (Y-branched AAO templates) have been synthesized by Zaraska *et al.* [184]. According to them, separated the oxides after completion the anodization first step, then anodization second step was started via 60V as illustrated in Fig. 3.8(d). Then the voltage dropped from 60 to 42V sharply after few minutes to start the second step of anodization, that affected the morphology of AAO templates (Fig. 3.8e).

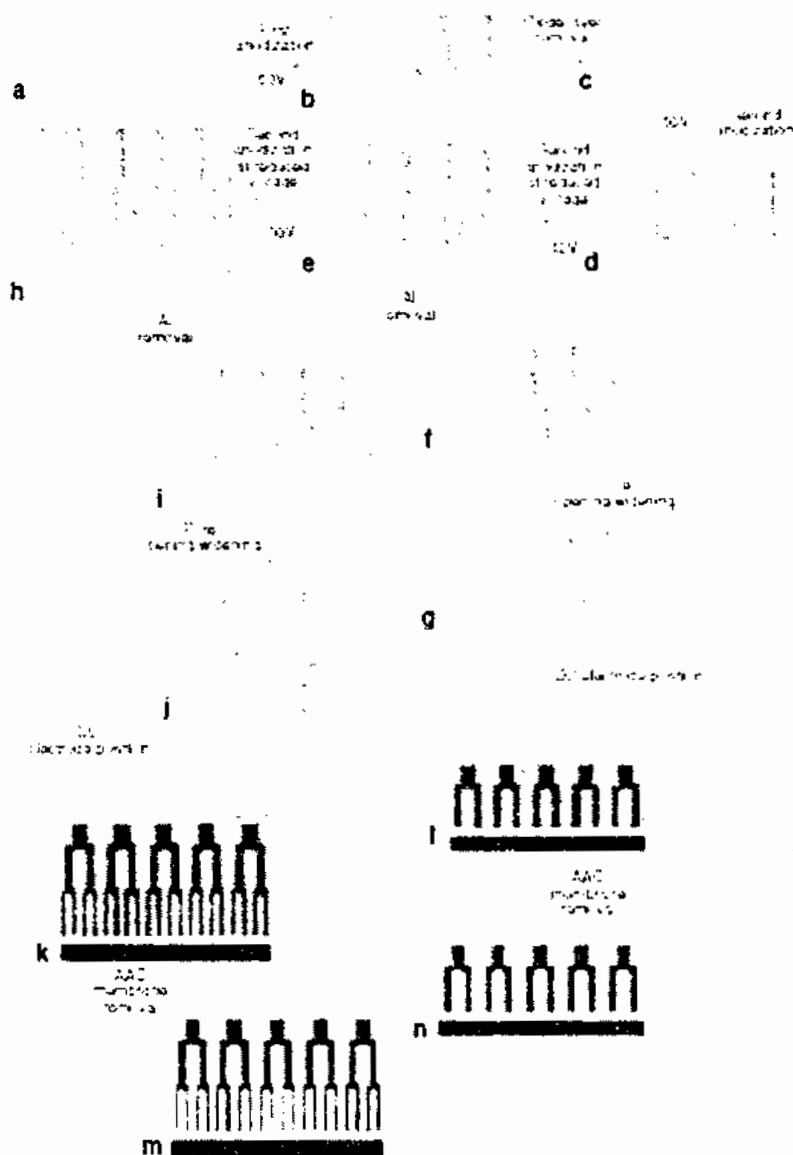


**Figure 3. 8:** Schematic representation of the formation of Y-branch AAO templates and deposition of material to synthesize NWs

The formation of three separately segmented anodic alumina through different diameter was obtained by reducing the voltage from 42 to 30V as shown in Fig.3.8 (h). After the synthesis of Y-branched shape AAO templates, one can deposited any material that is suitable for electrochemical deposition to get the very smart and definite structure. That produced a new way to enhance the properties of nanodevices in the present and future prospectus.

### 3.8. Electrodeposition

For the first time, Tin (Sn) was electrochemically deposited in 1970 by Possin [185]. After that such approach has been used all over the world to synthesize NWs, NTs and thin film. The motivation and attraction towards electrochemical deposition over the previous techniques for the researcher is due to the versatile, easy to control and economical, especially for the synthesis of the nanostructure. The factors that enhanced the properties of deposit material through electrochemical technique can be tuned through deposition voltage, temperature, composition/concentration of electrolyte and selecting of AC/DC channel. The steps of DC electrochemical deposition to synthesize NWs are shown in the schematic diagram (Fig.3.9).

For DC electrochemical deposition first, the aluminum substrate is removed from the base of AAO templates, and then the conducting material sputtered at the base of AAO templates that produced the way to deposit the desired material through DC electrochemical deposition. It consists of three electrodes; working electrode (work as a cathode), a counter

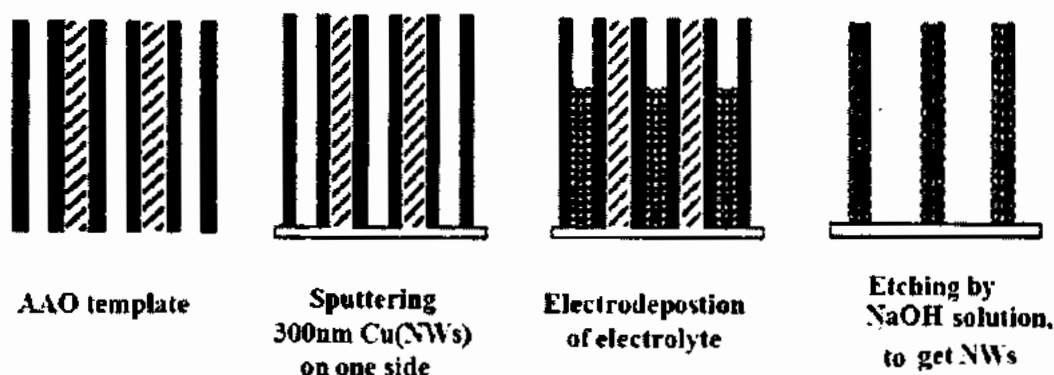


**Figure 3. 9:** The schematic diagram shows the complete synthesis of NWs using electrochemical deposition after removal of the barrier layer

electrode (work as an anode) and a reference electrode. From platinum (Pt) sheet or wire that is few millimeters thick called the counter electrode, with working electrode (cathode) AAO templates are attached through which the desired materials are deposited inside the templates and the reference electrode is placed near the working electrode inside the electrolyte. Hence negative DC potential is applied on the working electrode, as a result, the pores of AAO templates are starting to fill and one can wait till it fill up to its maximum (top) value. So in this way, one can be synthesized the order and uniform nanowires (NWs), nanotubes (NTs) and nanorods (NRs) in the desired and control length and diameter.



Similarly, in AC-Electrochemical deposition, it does not need to remove the substrate (aluminum) completely from the AAO templates to deposit the desired material as necessary for DC- electrochemical deposition. In such process, it needs only partially or cracks produced inside the oxide base of AAO templates that created the conducting path for the deposition inside the AAO templates. In AC-Electrochemical deposition, two electrodes (Cathode and Anode) are used so that the sample is connected either with cathode or anode. Remaining all the parameters are optimized before the deposition begin to start as discussed in the above part of this chapter in detail. During AC- electrochemical deposition the color of the sample change from whitish to blackish w.r.t to the time that showed the nucleation and growth of the desired NWs.

### **3.9. Sample Preparation for Characterization**

After deposition of the desired material inside the AAO templates, NWs, NTs and NRs are synthesized. In order to characterize them used XRD, SEM, EDX, VSM, Four probe Hall technique (Electrical properties). All the above characterizations have been done inside the AAO templates. Whereas for SEM and EDX the templates are etched with optimized molarity of NaOH for 100 to 120mnts time at 60°C. After removal of AAO templates the sample should be clean with distilled water for sufficient time and then dry in a clean and dust free environment. After that few nanometers gold (Au) has been sputtered with the base of AAO templates to produce conducting path for the characterization of SEM, EDX and TEM analysis.

---

---

---

## **Chapter No. 4**

---

---

## Chapter No. 4

### Characterization Techniques

#### 4.1. Morphological Analyses

There is a huge possibility to change lattice parameters after chemical synthesis. Therefore, simple NWs, alloy NWs and Heusler alloy NWs were characterized morphologically and topologically with scanning electron microscopy (SEM) after successful electrochemical deposition. For more resolution and magnification, Transmission electron microscopy (TEM) can also be used instead of SEM. And Energy dispersive X-ray spectroscopy (EDS) technique was used to analyze the chemical composition. So all of the above techniques required the NWs without the AAO templates, which were dissolved in NaOH aqueous solution.

##### 4.1.1. Scanning Electron Microscopy (SEM)

Generally Scanning electron microscopy (SEM) technique is employed to examine the surface topology, morphology and particle or grain size. The block of the SEM diagram is shown in Fig 4.1. First electrons are generated from the source of electronic gun (Grid), that are accelerated on to the surface of the sample, as soon as electrons interacted with its surface, resulting in an ejection of primary electrons, X-rays and backscattered electrons, All radiations i.e. backscattered electrons, secondary electrons etc. can be collected by the detectors. The

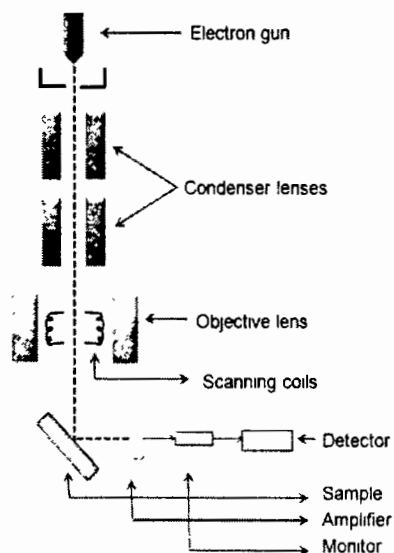
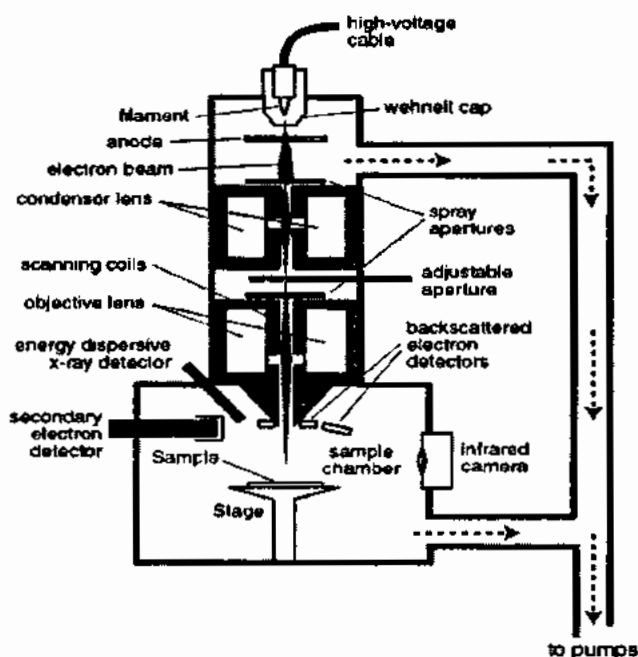


Figure 4. 1: Functional Block diagram of scanning electron microscope (SEM)

information about sample surface across the screen can provide as collectively effect the amplified current from the detector combined with the spot of the cathode ray tube (CRT).



**Figure 4. 2:** Schematic diagram of a Scanning electron microscope.

In Fig. 4.2, the electrons are accelerated rapidly due to a very small spot of the beam about 5 nm. These electrons were accelerated as they gain energy up to 10 MeV with a wavelength of 0.12 Å with comparison to the wavelength (4 to 7) x 1000 Å of visible light. As soon as the electrons interacted on the surface of the sample, the electrons are emitted with photons from the surface of the sample (material) and these electrons are collected by cathode ray tube (CRT) which showed them as an image.

### Secondary Electrons Emission

The incident electrons with very short wavelength on the surface of the material (sample), results in scattering of electrons with two different types have been observed; one is elastic and second is inelastic scattering. During inelastic collisions, the incident electrons is transferred their energy to the electrons of sample material, and therefore emission of electrons was carried out. If the energy of electrons is < 50eV, then these electrons are referred to as the secondary electrons.

### Emission of Back-Scattered Electrons

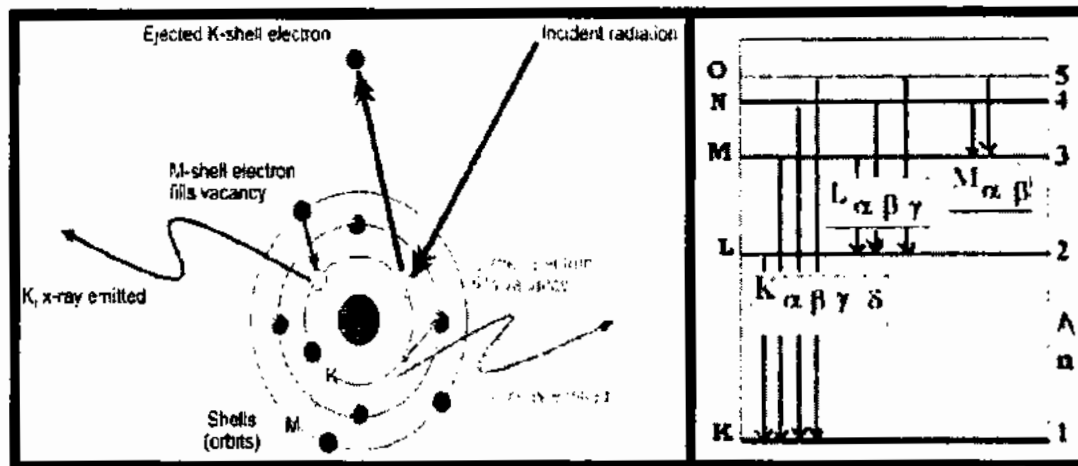


Figure 4.3: Schematic of inner shell transitions and K, L and M series

The energy of back-scattered electrons is generally so high that it is almost comparable to the energy of the incident electron. In conducting samples, the production of backscattered electrons has been produced with maximum possibility due to their large number of atoms. These electrons are not taking part in energy dispersive X-ray analysis (EDS).

#### 4.1.2. Energy Dispersive Spectroscopy (EDS)

This tool is very useful for research at laboratory level which measures the composition at a specific ratio of the required samples. In this process, electrons are generated from an electron gun (source of an electron) and the beam of electrons strike on the atoms of the sample that causes the transitions of the inner shell. As the incident electrons transferred their energy to the inner shell electrons that is bounded near the nucleus, which produce atoms in the excited state. Thus vacancy (hole) is produced, as electrons jump from the ground energy state to the higher energy states. Now to fill the vacant space (hole), electrons are fallen down from the higher energy states and release some definite rays called characteristics X-rays which are analyzed by EDS. Only those electrons are occupied the holes whose energy become equal to the difference of energy of the two shells. Hence, the continuous emission, that measures the composition of the desired materials as schematically in Fig.4.3.

Different radiations are produced during the interactions of incident electrons on the samples that includes Energy dispersive spectroscopy (EDS) and X-rays. The sensor is used to

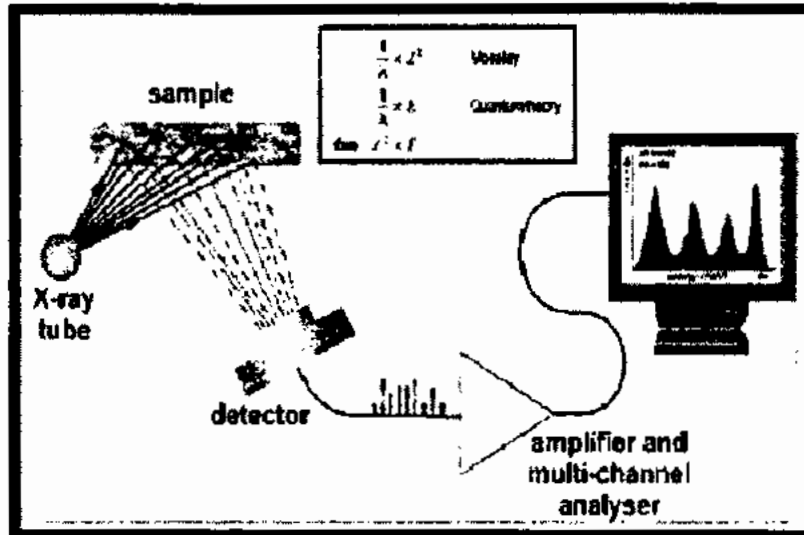


Figure 4. 4: Energy Dispersive Spectrometers

disperse the typical X-rays of distinct materials into an energy spectrum. During EDS, specific software is used to analyze the energy spectrum in order to measure the specific elements.

#### Auger electrons

Auger electrons are emitted when incident electrons interact with the core electrons on the surface of the sample. So these electrons are responsible that displayed the elemental composition ratio.

The strike of X-rays on the sample that generated an extra vacancy by second knocked out electron, such phenomena is known as auger effect. In this phenomena, first X-rays are fallen on the sample which ejected the electrons from the core-shell and creates a hole. To fill such vacancy, the electron jumped from the upper shell and released some amount of energy equal to the difference of the two shells. This energy was used to knock out the secondary electron. Such electron (secondary electron) is known as "Auger electron". The schematically diagram is shown in Fig.4.4.

In such phenomenon, emitted X-rays are called characteristic x-rays. These holes or vacancies are generally filled by an electron in K, L and M shells. Hence different names or symbols are allocated to these shells which were filled by different shells of electrons. If L-shell electrons filled the vacancy of K-shell, then emitted X-rays are known as K-alpha. If such vacancy was filled by M-shell then such X-rays are known as K-beta as shown in Fig.4.3

### Working and Boundaries Limitations

1. The X-rays radiation generated the energy peaks of various elements these were taken from different energy shell. Hence such shell (K, L and M) are overlapped each other in various elemental compositions.
2. It is difficult for EDS to identify those elements, whose atomic number is classically less than Na.

### 4.2. Structural Analysis

In chemical synthesis, there is a huge possibility to change the lattice parameters. Therefore, after successful synthesis of magnetic and Heusler alloys NWs through an electrochemical process, the structure was analyzed and confirmed initially by X-ray diffractometer (XRD) technique.

#### 4.2.1. X-ray diffraction (XRD)

The Structure of nanomaterials can be characterized through XRD, which is basic and very valuable technique among all. For Heusler alloys NWs, It is essential to determine the precise and accurate position of the atoms in the crystal lattices. XRD can also be used to measure the crystallite size or grain size associated with the width of the diffracted peaks determined through the Scherrer formula as shown in Eq-4.1:

$$D = \frac{k\lambda}{\beta \cos(\theta)} \quad 4.1$$

Where  $k = 0.9$  represents the correction factor (also known as shape factor),  $\lambda$  is incident wave length of X-ray (Cu  $K\alpha = 1.5406\text{\AA}$ ),  $\theta$  is the peak position and  $\beta_{hkl}$  represents full width at half maximum (FWHM), which is taken in radian and  $D$  is the diameter of the grain size taken in angstrom ( $\text{\AA}$ ).

Lattice strain in the materials was measured through Stock Wilson equation due to its widening of the diffraction peaks, as given by the relation Eq-4.2.

$$B_{strain} = \eta \tan\theta \quad 4.2$$

In XRD, diffraction pattern is observed only, if the wavelength of the interacting radiations is compared to the crystal structure of interatomic distance. So the wavelength of X-rays have taken in few angstroms which is nearly comparable to the inter-planer spacing of

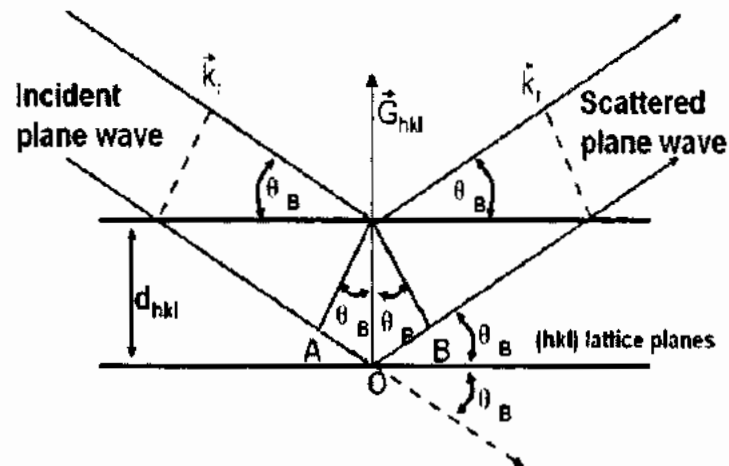


**Figure 4. 5:** The Bragg's law determines the spacing of the crystal's lattice (straight black arrow) between the lattice planes surface (blue horizontal lines). The left side and right side Green arrows show incident and scattered X-rays respectively. Where  $\theta$  is the diffraction angle between the incident and diffracted X-rays received through the detector.

crystal structure. Hence, structural information of material was investigated through XRD that were scattered from the lattice positions of the crystal structure. The XRD working principle is concerned with the scattered X-ray after striking with the lattice planes as a function of wavelength, energy, polarization, incident and scattered angle. Let X-rays are allowed to strike on parallel planes placed at distance  $d$  (inter-plane spacing) as shown in Fig. 4.5.

The X-rays incident on parallel planes through an angle  $\theta$ , as listed in above Fig 4.5. If the path difference between B to B' and A to A' equal to  $n\lambda$ , then it is said to be constructive interference. Such phenomena was first explained by L. Bragg and W.H Bragg in 1913. According to him, the interaction of X-rays produced diffraction pattern with respect to their lattice spacing that relates the Eq-4.3.

$$n\lambda = 2d \sin\theta \quad 4.3$$

Hence, ' $n$ ' is a positive integer and ' $\lambda$ ' correspond to a wavelength of X-rays used in angstroms ( $\text{\AA}$ ), ' $\theta$ ' shows the diffracted angle and ' $d$ ' is the inter-planar spacing, In Eq-4.3, one can find the lattice constant ( $d$ ) easily, whereas integer  $n=1$ , wavelength ( $\lambda$ ) and angle ( $\theta$ ) are all known quantities. Later on, the density of crystal structure, particle size, cell parameters and unit cell volume can be calculated after the initial evaluation. Secondly, another two ways that was analyzed our sample for crystal structure with the help of; JCPDS cards (Joint Committee



on Powder Diffraction Standards) or ICDD cards (International Center for Diffraction data). Which is already reported in research work and another method is by Rietveld confinement.

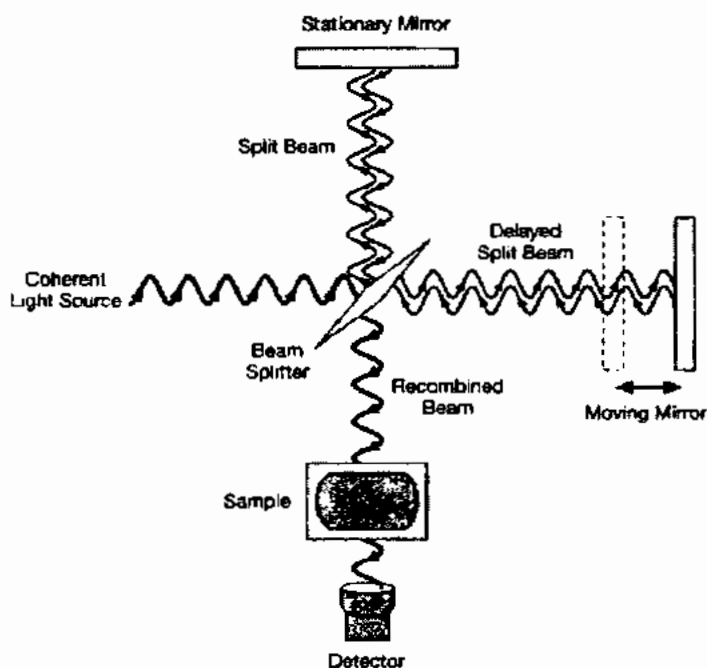


**Figure 4. 6:** The schematic diagram Fourier transform infrared spectroscopy (FTIR)

#### 4.2.2. Fourier Transform Infrared Spectroscopy (FTIR)

To determine the structure and bonds of the unknown molecules produced during the synthesis of the samples that were identified through the frequency of vibrational modes of the molecule, IR spectroscopy is used. Among all, large numbers of normal modes were confined at a specific functional group that identifies the particular functional groups such as; C-O, C-H stretching bond as well as it shows the presence of bending vibration of a hydroxyl group and a carbonyl group.

All the incident frequencies are quantized and somehow slightly changed due to different molecules; the spectrum comprises the absorption bands at the specific wavenumbers or frequencies. The basic operational principle of IR spectroscopy; series of frequencies were emitted from IR source and incident on a sample as illustrated in Fig. 4.6. The energy of these photons with definite specific frequencies was absorbed.

All wavelengths have been collected simultaneously that shows in the enhancement of its sensitivity. The splitter was used to split the incident beam from the source. After splitting, the first beam was directed towards the fixed mirror which then reflects back to the splitter

beam, and the second beam was directed towards the movable mirror (normally a few millimeters). To adjust the reflected beam of both rays, the second beam which strikes with a moveable mirror through which the length was adjusted against the reflected beam from the stationary-mirror. The two beams after reflection from a fixed and moveable mirror with different path lengths interfere again at the beam splitter that produced constructive and destructive interference (an interferogram). It gives us informations that was taken from each wavelength after transmitted through or reflect from the sample in a time-domain range. Then the results from fourier transformation was taken through mathematically, as the intensity of light at each individual frequency was extracted via computationally. The graph was obtained with intensity against wavenumbers that shows different bonds in various materials at different frequencies [35]. In this work, a Biorad FTS-40 and Varian 7000 FTIR spectrometer is used to obtain spectra of the samples in the range from 600 to 4000  $\text{cm}^{-1}$  with 4  $\text{cm}^{-1}$  resolution. In such type of research, the importance of FTIR was never denied, but due to its some limitations, such as it has difficult to examined the spectra that obtained in a complex mixtures and assign or allocate their peaks accordingly.

### 4.3. Magnetic Measurements

There is a huge probability to change lattice parameter during the chemical electrochemical deposition process. Therefore for all, pure NWs, alloys NWs and specifically Heusler alloy NWs were characterized magnetically through Vibrating sample magnetometer (VSM). It is notable that the samples for SEM, TEM and EDS characterization were first separated from the templates via through chemical etching process. While the samples (NWs) were retained inside the templates to make NWs were aligned in proper direction during the magnetic measurement.

#### 4.3.1. Vibrating Sample Magnetometer (VSM)

Van Oosterhart and S. Foner were the first to develop vibrating sample magnetometer (VSM). The magnetic properties were commonly investigated through VSM technique. The VSM schematic is shown in Fig.4.8.

This technique is based on the Faraday's law of electromagnetic induction, which states that 'in an electrical circuit, the induced voltage  $V(t)$  is directly proportional to the change of magnetic flux per time taken

$$V(t) = - C d\phi/dt \quad 4.5$$

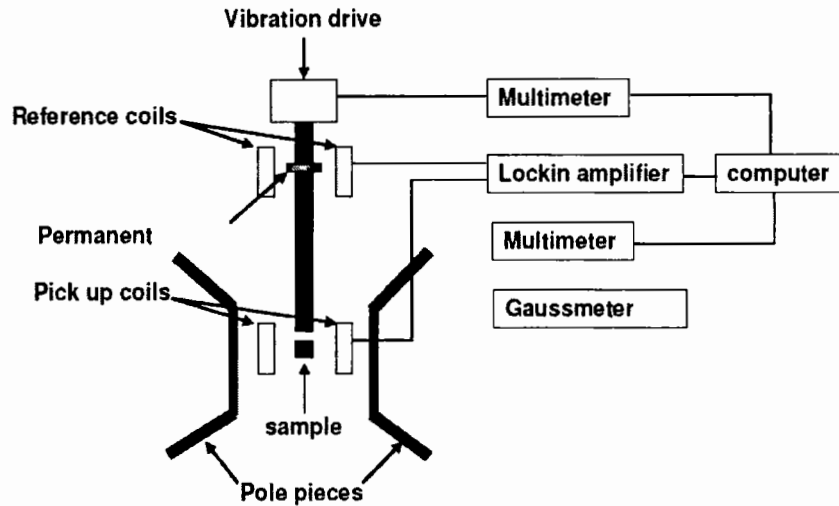


**Figure 4. 7:** Schematic illustration of VSM

To measure the magnetic properties, the samples were attached with the bottom of the non-magnetic holder that vibrates due to the vibratory assemblage. Also in VSM field was produced by the electromagnetic owing to generating of the flux by the samples which were recorded through detection coils. Resulting the magnetization was produced by the change the change of magnetic field which is directly proportional to each other. Started from minimal (zero), the field gradually increases directed towards positive (maxima) and then negative (maxima) cycle, and in this way, negative cycle towards positive cycle was repeated again. And finally, M-H loop or hysteresis loop was generated in a form of complete repeated cycle. Usually, the magnetic moment in VSM technique was taken in emu (CGS-unit), so the value of magnetization was taken in emu/gm. In this research, all measurements of VSM technique was taken at room temperature. Vibrating sample magnetometer (VSM) of model Micro-Sense EV-9 was used to measure magnetic properties and this device has the capacity to generate a magnetic field of  $\pm 20$  kOe. Due to intrinsic properties of different materials different applied field is required. Such as Co and Fe have large anisotropy, required high applied field to saturate them compared to Ni (completely saturates at Ni  $\pm 5$  kOe).

#### 4.4 Two Point Probe Hall Technique

In General, the electrical measurement in two-probe technique is used to calculate the resistance between two points in a conductor. Therefore, the resistance/resistivity can be

measured from the current and potential difference that are calculated from such technique as illustrated in the Fig.4.8.

From the above Fig.4.8 shows that the current flow from probe-1 to probe-2 that can be measured through ammeter (A) and the potential difference drops across the two end of the probe can also be measured through voltmeter (V). Using the well-known relation to calculate the resistivity of unknown conductor;

$$\rho = \frac{V A}{I L} \quad 4.6$$

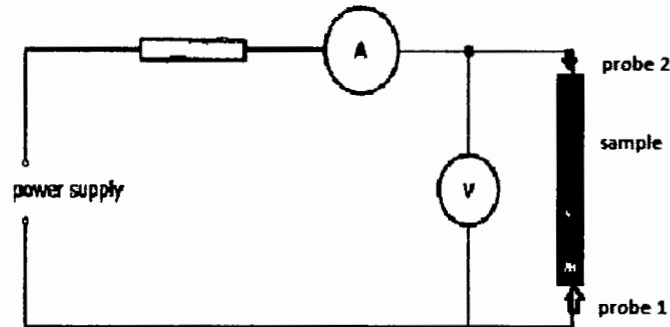


Figure 4. 8: Setting of two probe system

Here 'L' is the length of conductor (between the two- probes) and A is correction area of the sample.

#### Limitations in the two probe Technique

- i- In such technique the lead connection increase the resistance of the sample.
- ii- The connection of the nanomaterials for such characterization is so difficult
- iii- Two-probe technique cannot be use for the irregular shape body

So another technique to measure the resistivity of sample called 'Four point probe', through which different shapes of samples are characterized without soldering connection to prevent the sample from heating.

#### 4.4.1. Four Probe Method

The metal (tungsten) tips supports by spring with various radius is used in such technique. The connection (tips) are spaced equally from each another as shown in Fig 4.9. During the characterization, the spring prevent the sample from the damage (prevent from hard pressing). The inner two probe (2 and 4) measure the potential difference while the outer two probe (1 and 4) calculate the current. So from these to results the resistivity can easily be measured as given in above equation. The input impedance is very high in the inner circuit so that the current cannot pass and the potential is dropped across these two probes.

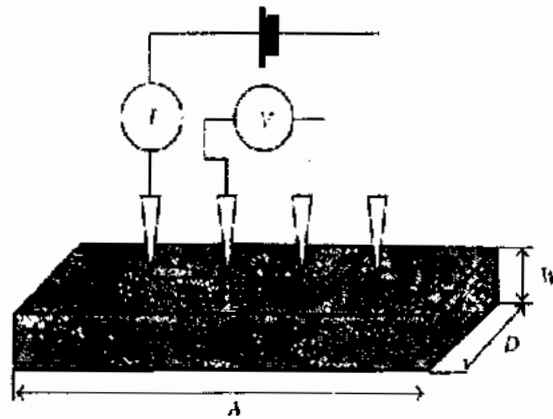


Figure 4. 9: Four point probe measurement scheme

---

---

## **Chapter No. 5**

---

---

## Chapter No. 5

### Electronic, Magnetic and Half-Metallic Properties of $L2_1$ -type $\text{Co}_2\text{Mn}_{0.5}\text{Fe}_{0.5}\text{Sn}$ Heusler alloy Nanowires

#### 5.1. Introduction

To increase the interest in the research field of spintronics or magneto-electronics during the last few years, so-called half-metallic ferromagnetic materials with high Curie temperature are required [186, 187]. The gap present at the Fermi level shows 100% spin-polarized that increased the performance of the spin-dependent devices. In the present time, the family of Heusler alloys [114], especially Co-based full-Heusler alloys has appealed remarkable interest in the technological and scientific field of spintronics due to their greater stability in half-metallic both in the experimental and theoretical analysis [121, 188]. Hence, it has unlimited and outstanding magnetic and transport properties to enhance the efficiency of devices based on half-metallicity [189]. The efficient and high spawned input, spin current makes them valuable candidates in spin-transfer torque (STT) [190, 191], magnetic sensor devices [192] and increase the effect of the giant magnetoresistance (GMR) [193]. During the recent decade, the large values of MR in the early stages due to quaternary ( $\text{Co}_2\text{Cr}_{0.6}\text{Fe}_{0.4}\text{Si}$ ) full Heusler alloy in MTJs produced huge interest in TMR and GMR devices [124-126, 194]. Up to now, Co-based ( $\text{Co}_2\text{Mn}_{0.5}\text{Fe}_{0.5}\text{Sn}$ ) Heusler alloy nanowires (NWs) synthesized in anodized aluminum oxide (AAO) templates with AC- electrodeposition has not been reported in the literature. In magnetic properties, the effective anisotropic field is also contributed by magnetostatic anisotropy field, shape anisotropy and magneto-crystalline anisotropy field. The shape anisotropy is dominant along NWs which makes it suitable for perpendicular data storage devices and sensors applications. In this paper, we have prepared  $\text{Co}_2\text{Mn}_{0.5}\text{Fe}_{0.5}\text{Sn}$  NWs into anodized aluminum oxide templates by changing the AC potential rather than changing the pH, concentration and temperature of solution each time to induce interesting properties. Beside it, we have used density functional theory (DFT) to discuss its arrangement of magnetic moment and proved that this alloy is half-metallic with 100% spin-polarization. It will open the new way to increase the efficiency of spintronics devices in the future.

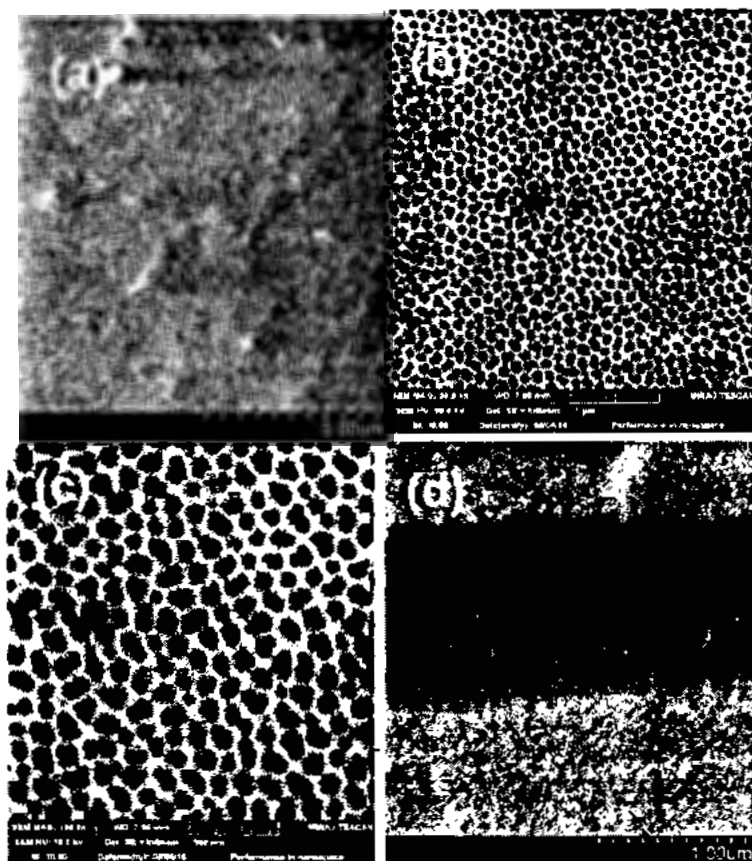


**Figure 5. 1:** Typical top-view SEM image of AAO templates at 5  $\mu\text{m}$  scale, (b) Top-view SEM image of AAO templates at 1  $\mu\text{m}$  scale, (c) Top-view SEM image of AAO templates at 500 nm scale and (d) the cross-section SEM image of AAO templates.

## 5.2. Results and Discussions

### 5.2.1. Synthesis and Morphology of AAO Templates

The synthesis of AAO templates using two steps of anodization was explained in detail in our previous work [195]. The overall chemical reaction during the anodization process;

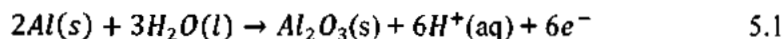
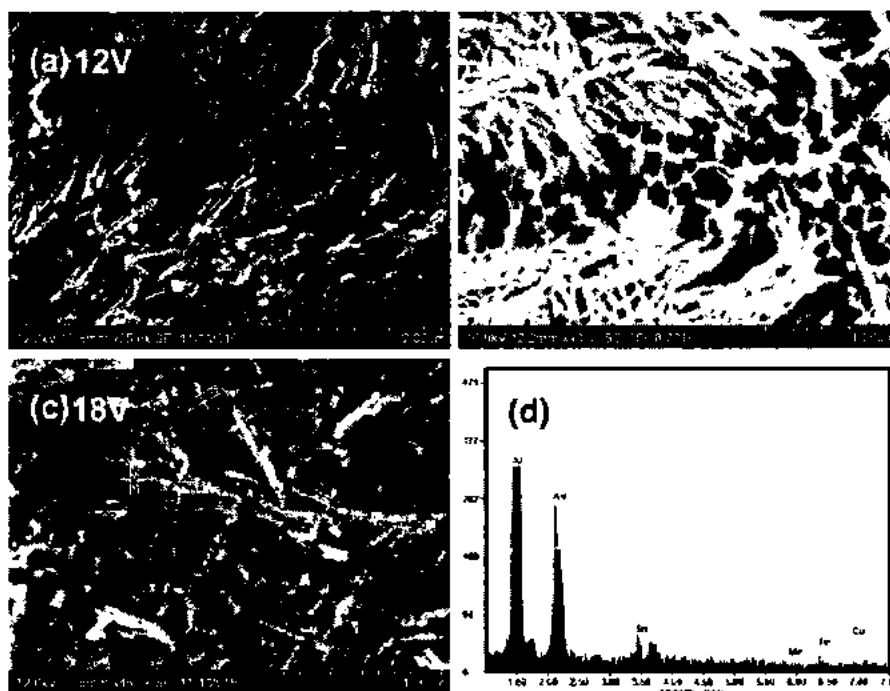


Fig. 5.1 shows the SEM images of AAO templates from which (a, b & c) were taken at the top view and (d) shows the cross-section view of AAO templates. These images confirm that diameter and interpore distance was 62 nm and 115 nm respectively while length lies in the range of microns. These results show that templates are hexagonal arrays in a regular pattern.



### 5.2.2. Morphology of Nanowires



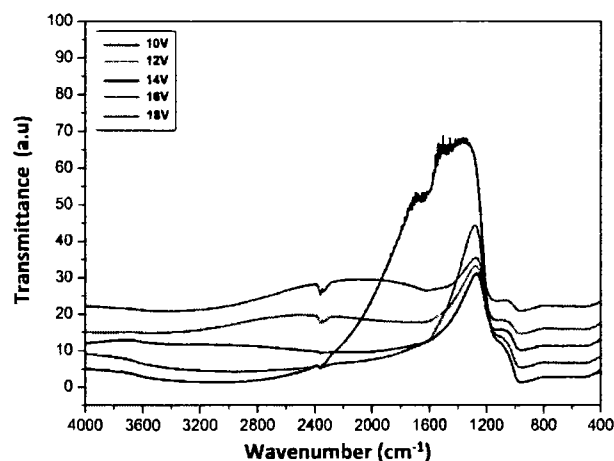
**Figure 5. 2:** The SEM images of NWs deposited at different voltages. (a) 12 V, (b) 14 V, (c) 18 V and (d) shows EDX of NWs.

Fig. 5.2 (a, b & c) shows the SEM images of Co-based ( $\text{Co}_2\text{Mn}_{0.5}\text{Fe}_{0.5}\text{Sn}$ ) full Heusler alloy NWs which was confirmed from EDS as shown in Fig. 5.2 (d). The average diameter of these NWs was 58 nm showing a regular, aligned and homogenous shape. Because up to now, no technique was recorded in literature in which nanowires were aligned even after the removal of templates as explained in the experiment.

### 5.2.3. Molecular Analysis

We have synthesized Co-based ( $\text{Co}_2\text{Mn}_{0.5}\text{Fe}_{0.5}\text{Sn}$ ) nanowires using AC-electrodeposition. The chemistry of the surface morphology changes dramatically due to the increase of aspect ratio (surface to volume ratio) of NWs. It is due to the increase of the ratio of dangling bond on the surface of NWs and more active surface is created at the nanoscale. FTIR technique is relatively more important and interesting to study the synthesized Co-based ( $\text{Co}_2\text{Mn}_{0.5}\text{Fe}_{0.5}\text{Sn}$ ) full Heusler NWs as shown in Fig. 5.3.

Fig. 5.3 shows the FTIR spectrum which was recorded in the range of  $400\text{-}4000\text{ cm}^{-1}$ . All samples show approximately similar peaks, i.e. the peaks lie in the region  $(900\text{-}1000)\text{ cm}^{-1}$  and  $(1100 - 1200)\text{ cm}^{-1}$  were linked with the excitation of  $\text{Al}_2\text{O}_3$  and C-O stretching bond



**Figure 5. 3:** The FTIR results in Co-based ( $\text{Co}_2\text{Mn}_{0.5}\text{Fe}_{0.5}\text{Sn}$ ) full Heusler alloy NWs

respectively whereas the region lie ( $2300\text{-}2400$ )  $\text{cm}^{-1}$ , broadband ( $3200\text{-}3600$ )  $\text{cm}^{-1}$  corresponded to  $\text{CO}_2$  molecular and hydroxyl ions due to water molecules present on the surface which contributed from air and synthesis of aqueous solution.

#### 5.2.4. Structure Analysis

The ternary  $\text{X}_2\text{YZ}$  Heusler alloy has usually  $\text{L}_{21}$  structure with the space group ( $\text{Fm-}3\text{m}$ ). When one of the X-atoms is replaced by another transition element, we can get the quaternary structure of Heusler alloy  $\text{XX}'\text{YZ}$  with the space group of  $\text{F-}43\text{m}$  (space group 216). So the crystal structure of Co-based ( $\text{Co}_2\text{Mn}_{0.5}\text{Fe}_{0.5}\text{Sn}$ ) Heusler alloy NWs were studied by X-ray diffraction (XRD) analysis with  $2\theta=20^\circ\text{-}100^\circ$  range. The increase in intensity and shift of diffraction peaks have been observed in all five samples. These variations indicate that deposition voltage not only affects the composition of alloy but also affects the order of crystalline network and lattice strain. The XRD result shows many reflection peaks as shown in Fig.5.4 which has been compared with standard data [ICSD cards: 652713, 150692] and indexed them as Sn, and  $\text{Co}_2\text{Fe}_{0.5}\text{Mn}_{0.5}\text{Sn}$  structure.

It was found that the NWs deposited at 14 V and lower than 14 V, only show fundamental reflection peaks [(220), (400) and (531)]. This type of diffraction peaks reveals  $\text{L}_{21}$  type of crystal structures with A2 and B2 disorder. Besides these fundamental reflections, it also contains (101) and (110) reflection peaks that indicate the tetragonal crystal structure of Sn. The XRD of the full heusler alloy structure consists of the odd super lattice, even super lattice and fundamental reflections. However, the main characteristic super-lattice reflections peaks [(111) and (200)] with fundamental peaks were only observed in a sample deposited at

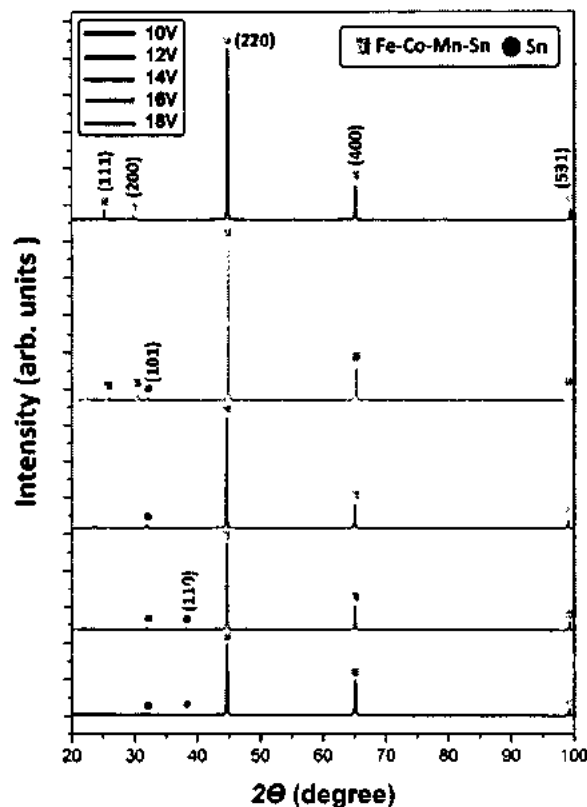


**Figure 5. 4:** The X-Ray Diffraction results Co-based ( $\text{Co}_2\text{Mn}_{0.5}\text{Fe}_{0.5}\text{Sn}$ ) full Heusler alloy NWs.

16 and 18 V, which corresponds to  $L2_1$  crystal structure, but sample deposited at 16 V also contains fundamental reflection tetragonal phase of Sn as well.

### 5.2.5. Compositional Analysis

Energy dispersive X-Ray spectroscopy (EDX) technique was used for the compositional analysis which confirmed the deposition of Co, Fe, Mn and Sn in the synthesis of NWs as shown in Fig.5.5.

The graph was plotted against different deposition voltages which clearly shows that different material has their different reduction potential, i.e Sn decreases with increase in deposition potential whereas (Co, Fe & Mn) almost increases with increase in deposition potential as shown in Table 5.1. These variations mainly affect electrical and magnetic properties as well as necessary for the formation of Heusler alloy NWs.

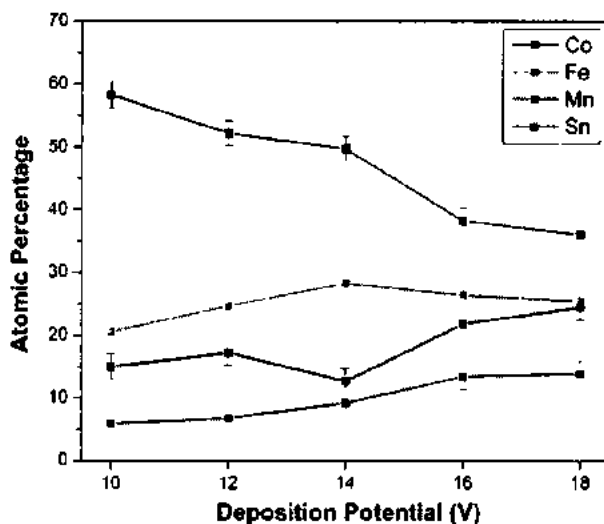


Figure 5. 5: The dependences of Co, Mn, Fe & Sn deposition on different AC potential value.

### 5.2.6. Magnetic Measurements

The magnetic properties of Co-based ( $\text{Co}_2\text{Mn}_{0.5}\text{Fe}_{0.5}\text{Sn}$ ) full Heusler alloy NWs were explained on the basis of the VSM technique as shown in Fig.5.6 (a). All five samples were characterized at room temperature and show excellent magnetic properties used in many spintronics devices. Fig. 5.6 (b) shows the variation of coercivity and saturation magnetization w.r.t deposition voltage. In general, the coercivity is affected by several factors, such as grain size, defects, Co content and variation of ferromagnetic (Fe & Co) and paramagnetic (Mn & Sn) ions in the synthesis of  $\text{Co}_2\text{MnFeSn}$  Heusler alloy NWs. The decrease of  $H_C$  may be due to the decrease of the grain size during the formation of Heusler alloy.

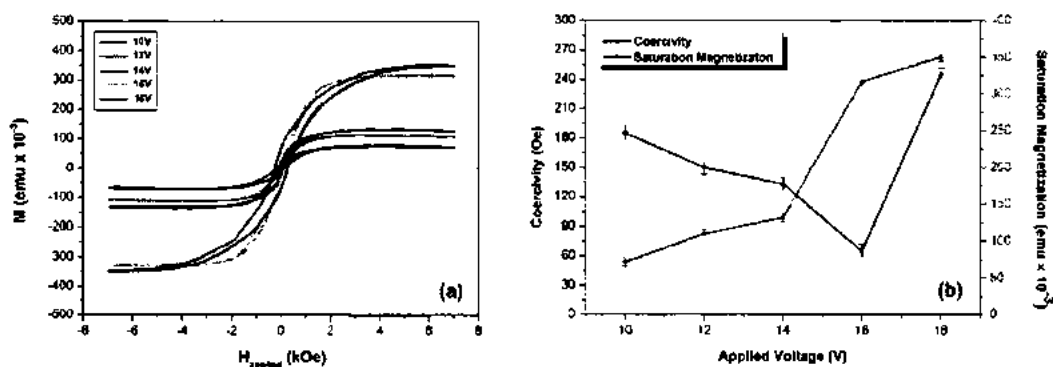


Figure 5. 6: (a) The Hysteresis loops of the Co-based ( $\text{Co}_2\text{Mn}_{0.5}\text{Fe}_{0.5}\text{Sn}$ ) full Heusler alloy NWs (b) The Coercivity and Saturation magnetization against Voltage of Co-based Heusler alloy NWs.

**Table 5. 1:** Different properties of Co-based ( $\text{Co}_2\text{Mn}_{0.5}\text{Fe}_{0.5}\text{Sn}$ ) full Heusler compound NWs.

V	at.%				Oe	$\text{emu} \times 10^{-3}$	$\text{emu} \times 10^{-3}$	$S^*$
	Fe	Co	Mn	Sn	$H_c$	$M_s$	$M_r$	
10	20.66	15.06	5.98	58.30	185	72	11	0.15
12	24.74	17.26	6.79	52.21	150	110	19	0.17
14	28.32	12.71	9.26	49.71	135	132	20	0.15
16	26.42	21.87	13.47	38.24	65	317	15	0.04
18	25.49	24.51	13.94	36.06	245	351	68	0.19

Furthermore, as voltage increases, the coercivity ( $H_c$ ) decreases and saturation magnetization increases, showing that deposition of nonmagnetic ions increases compared to magnetic ions in the compound. But finally, coercivity increases sharply up to (245 Oe) at maximum voltage (18V) shown in Table 5.1. This material could also be expected as a soft magnetic material. These variations twisted Co-based ( $\text{Co}_2\text{Mn}_{0.5}\text{Fe}_{0.5}\text{Sn}$ ) full Heusler phase in nanowires at a different deposited voltage which produced a new way to increase the efficiency of spintronic devices such as TMR and GMR, that produces a remarkable increase in the ratio of MR during the last decade [125, 194].

### 5.2.7. Electrical Measurements

First, the templates ( $\text{Al}_2\text{O}_3$ ) were dissolved in NaOH solution as explained previously that electrical measurement was analyzed with great precision without the interference of template

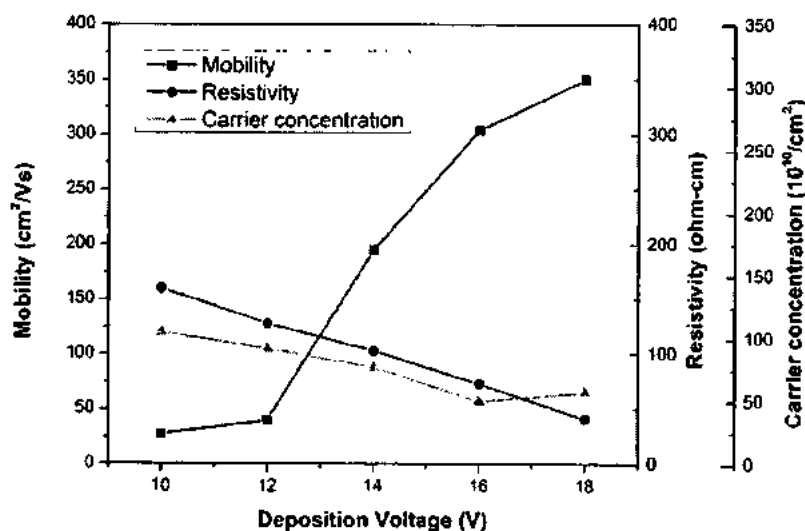


**Figure 5. 7:** Hall measurement shows the variation of mobility, carrier concentration & resistivity w.r.t deposition voltages of Heusler alloys NWs.

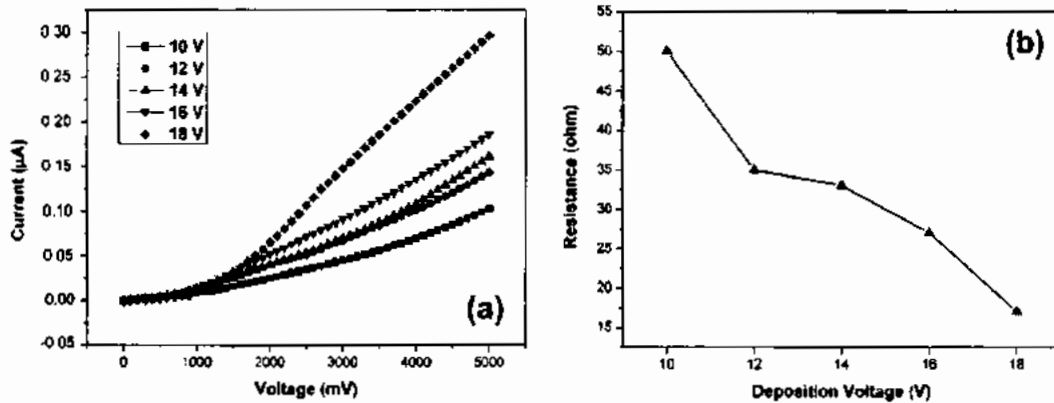


**Figure 5. 8:** (a) Two probe I-V curves show the resistance of Heusler alloys NWs (b) Shows the Resistance VS Deposition voltages of Heusler alloys NWs

(insulator). The  $I$ - $V$  curves which demonstrated the transport properties of Co-based ( $\text{Co}_2\text{Mn}_{0.5}\text{Fe}_{0.5}\text{Sn}$ ) Heusler alloy NWs are shown in Fig. 5.7 (a). It was characterized by two probe technique and Fig. 5.7 (b) shows that resistance decreases w.r.t deposition voltage. The transport properties of Co-based Heusler alloy nanowire electrode is much more efficient compared to the electrode of conventional porous nanoparticles [196].

We also characterized all the deposited samples (10 to 18 V) by four-probe (Hall technique) so that the comparison study among the variation of carrier concentration, resistivity and mobility may be performed as shown in Fig. 5.8. The mobility was increased from 28 to

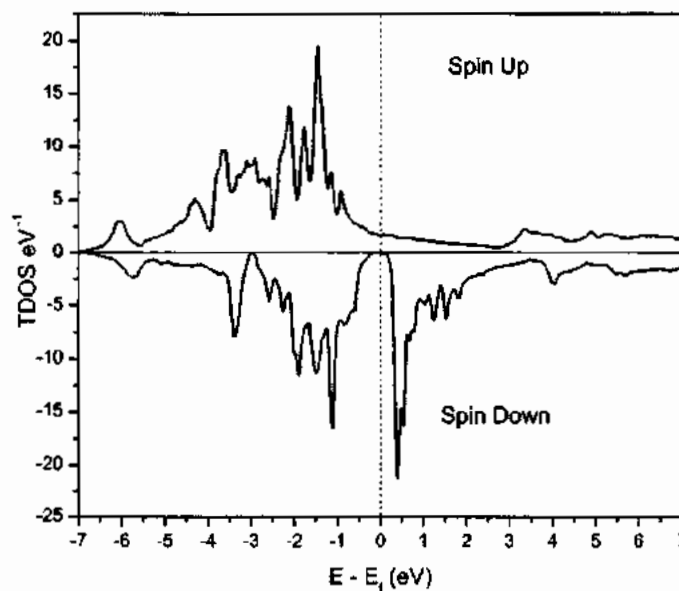


**Figure 5. 9:** Calculation of DOS for Co-based ( $\text{Co}_2\text{Mn}_{0.5}\text{Fe}_{0.5}\text{Sn}$ ) full Heusler compound NWs

358 cm<sup>2</sup>/Vs, whereas resistivity was decreased from 160 to 40 Ω-cm w.r.t increase in deposition voltage. The resistivity and carrier concentration decreased in a similar fashion w.r.t increase in deposition voltage, whereas mobility was increased with increase in deposition voltage which showed the increment of the grain size and diminishes the scattering of the electron grain boundary. But if the results were reciprocal to a present situation, then impurity scattering would be dominated. It means that our samples were pure without any contamination which confirm the results of FTIR. So the spin properties in (Co<sub>2</sub>Mn<sub>0.5</sub>Fe<sub>0.5</sub>Sn) Heusler alloy is of great interest for their practical use which is vigorous study in present as well as in future spintronics devices.

### 5.2.8. Computational Studies

To confirm the half-metallicity and ferromagnetism, we have employed state of the art full potential linearized augmented plane wave methods (FP-LAPW) within density functional theory as implemented in WIEN2k programs package [197]. Exchange and correlations approximation are made by generalized gradient (GGA) functional [198]. Details of the computational procedure can be seen elsewhere [199]. Muffin Tin radii for Co, Fe, Mn, and Sn are 2.45, 2.43, 2.43 and 2.43 respectively. The total spin-polarized density of states as shown in Fig. 5.9 and electronic band structure shown in Fig. 5.10 confirmed the half-metallic nature of Co<sub>2</sub>Fe<sub>0.5</sub>Mn<sub>0.5</sub>Sn Heusler alloy. In spin-up channel, valence band is made up have a major contribution from 3d states of Co, Fe, Mn and Sn and these d states cross the Fermi level assigning majority spin channel a metallic character. While in minority spin channel these states (3d states of transition metals) are localized and there appears a band gap of almost 0.26 eV. The half-metallic gap ( $E_{HM}$ ), which is the minimum energy for the electron to change the spin, can be calculated 0.26 eV using art full potential linearized augmented plane wave methods (FP-LAPW).

#### 5.2.8.1. The Slater-Pauling Rule

Slater and Pauling opened a new way to justify the magnetic moment  $m$  of the 3d elements and their alloys can be predictable on the basis of the average valence electron number ( $N_V$ ) per formula. That rule is also effective for the quaternary Heusler compounds as in our case Co<sub>2</sub>Mn<sub>0.5</sub>Fe<sub>0.5</sub>Sn.

$$m = N_V - 24 \quad 5.2$$

In our case  $N_V=29$ . So the total magnetic moment per formula (Co<sub>2</sub>MnFeSn) is  $5 \mu_B$ ,

Where  $\mu_B$  is Bohr magnetons that fulfills our experimental results.

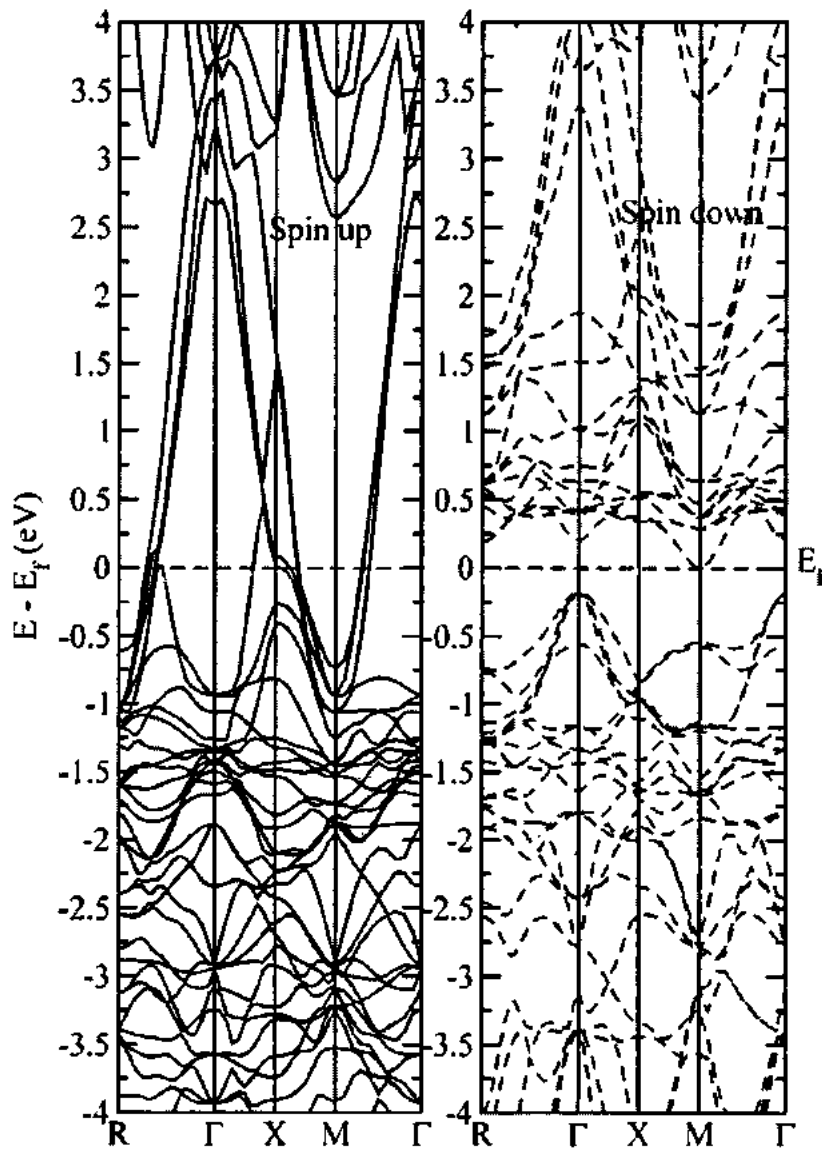


**Figure 5. 10:** Band structure of majority and minority spin states Co-based ( $\text{Co}_2\text{Mn}_{0.5}\text{Fe}_{0.5}\text{Sn}$ ) full Heusler alloy NWs.

### 5.2.9. Spintronics Properties

Co-based ( $\text{Co}_2\text{Mn}_{0.5}\text{Fe}_{0.5}\text{Sn}$ ) is half-metallic Heusler alloy which twists great interest towards spintronic devices due to its 100% spin polarization, was first predicted theoretically by K. Ozdogan *et al* [200]. The spin polarization of electron at fermi-level plays a vital role to use that specific alloy in the technical and scientific region.

$$P = \frac{N\uparrow(E_F) - N\downarrow(E_F)}{N\uparrow(E_F) + N\downarrow(E_F)} \quad 5.3$$



In  $(\text{Co}_2\text{Mn}_{0.5}\text{Fe}_{0.5}\text{Sn})$  Heusler alloy, Sn in a Si column is a much heavier element and large lattice constant produces smaller spin moment. That large lattice constant leads to increase in the majority states. The transition metals Fe and Mn have much larger space around them which leads to increase total spin moment extensively of the whole alloy  $(\text{Co}_2\text{Mn}_{0.5}\text{Fe}_{0.5}\text{Sn})$  [200].

To boost-up effective transport and spin-polarized carrier for practical application in spintronic devices, in a previous decade many researchers used ferromagnetic material which produced less than 100% spin polarization but due to deficiency of spin injection and slight spin polarization such materials were unsuitable for spin based technology [201]. A new type of material called Heusler alloy, which show half metallicity and 100% spin polarization at Fermi level and can predict to increase the efficiency of spintronics devices upto maximum value [202, 203].

---

---

## **Chapter No. 6**

---

---

## Chapter No. 6

# Structural, Magnetic and Transport Properties of Fe-based Full Heusler alloy Fe<sub>2</sub>CoSn Nanowires

### 6.1. Introduction

Fe-based full Heusler alloys show very interesting and significant magnetic, electronic and structural properties among other Heusler alloy [204-206]. They exhibit high Curie temperature, huge saturation magnetization and acquire half-metallicity at a room temperature which provides an ideal character for spintronics applications/devices [207, 208]. Half metallicity of the synthesized materials can be verified, either from theoretical model “density functional theory” (DFT) or total magnetic moment of the full Heusler alloy which must follow the Pauling Slater  $[M = (N_v - 24)\mu_B]$  formula,  $N_v$  is sum of valance electrons of the compound [208]. Currently, there are no reports in the literature on the fabrication of NWs using AC-electrodeposition based on Fe-Heusler alloy (Fe<sub>2</sub>CoSn). Fe<sub>2</sub>CoSn Heusler alloy NWs has got our attention due to all elements; Fe, Co, and Sn in the compound that can easily be deposited in the aqueous solution [209-211], which will give us a significantly new way to increase the efficiency of spintronic devices in future. Now permanent magnets with high energy density and coercivity products are obtained from the rare-earths with 3d metals alloys, despite their limited thermal stability and relatively low magnetization compared with ferromagnetic 3d transition metals like Co, Fe and their alloys. If 3d transition metals and their alloys can achieve high coercivity, then all these problems and hindrances correlated with the rare-earth magnets will be resolved. For this goal, magnetic nanorods (NRs) and nanowires (NWs) making use of shape anisotropy to enhance the coercivity could be new building blocks for permanent magnets [211].

### 6.2. Results and Discussions

#### 6.2.1. Synthesis of AAO Templates

The basic parameters for the synthesis of AAO templates by using two steps of anodization were explained in the experiment [212]. The chemical reaction for synthesis of pores arises at both interfaces, i.e Al<sub>2</sub>O<sub>3</sub> electrolyte, and Al/Al<sub>2</sub>O<sub>3</sub> interfaces. Al<sup>3+</sup> ions were emitted into the

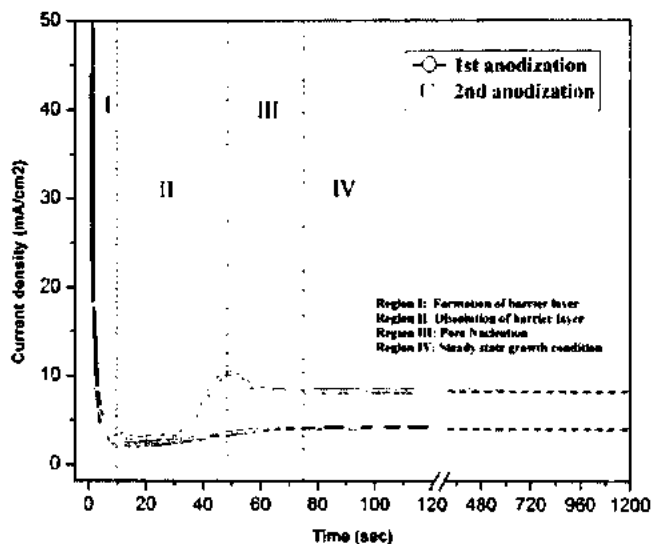
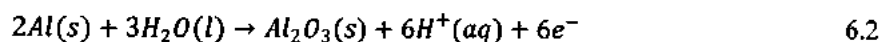


**Figure 6. 1:** Current VS. time graph using two-step anodization Prepared by 5%  $H_3PO_4$

electrolyte solution which affects the dissolution of  $Al_2O_3$ . Reactions related to the formation of pores at both  $Al/Al_2O_3$  interfaces and through ion movement across the barrier layer in which  $Al^{3+}$  ions drift towards  $Al_2O_3$ electrolyte interface:



Simultaneously water produced anions, reacted with Al to form  $Al_2O_3$



### Current VS Time graph of Anodization

The graph between current density Vs time transient recorded initially during the first 2 min of the first and second step of anodization as shown in Fig.6.1.

During the anodization, a rapid decrease of the current density was observed, that showed the formation of the barrier oxide layer (Step.1). The current density decreased at a slow rate indicated that cracks started at the barrier layer (Step.2). After completion of step 2, the current density was increased which indicated the formation of pore precursors (Step.3) [13, 177]. At last, the current density approximately became constant which was evidence that steady state of porous oxide formation was achieved. We called it the AAO template [213].

### 6.2.2. Morphology analysis

The SEM images of self-made AAO templates were synthesized by two steps of anodization as confirm from Fig.6.2. Three images of Fig. 6.2.(a-c) were taken from the top view of different samples with different resolutions showed highly ordered and aligned comprises the

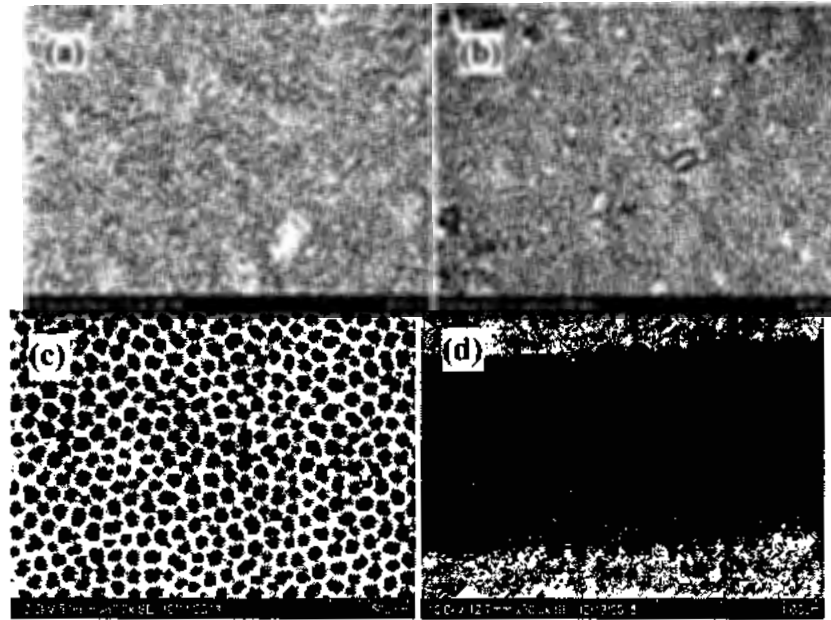


**Figure 6. 2:** (a-c) typical top view SEM micrograph of AAO templates and (d) show lateral view prepared by 5%  $H_3PO_4$  using two-step anodization with a high-density array of AAO templates

average pores diameter and interpore distance was in the range of 40 to 60 nm and 115 to 125 nm respectively. Fig. 6.2 (d) shows their lateral view which confirms alignment, order, and length was placed up to 15  $\mu m$ .

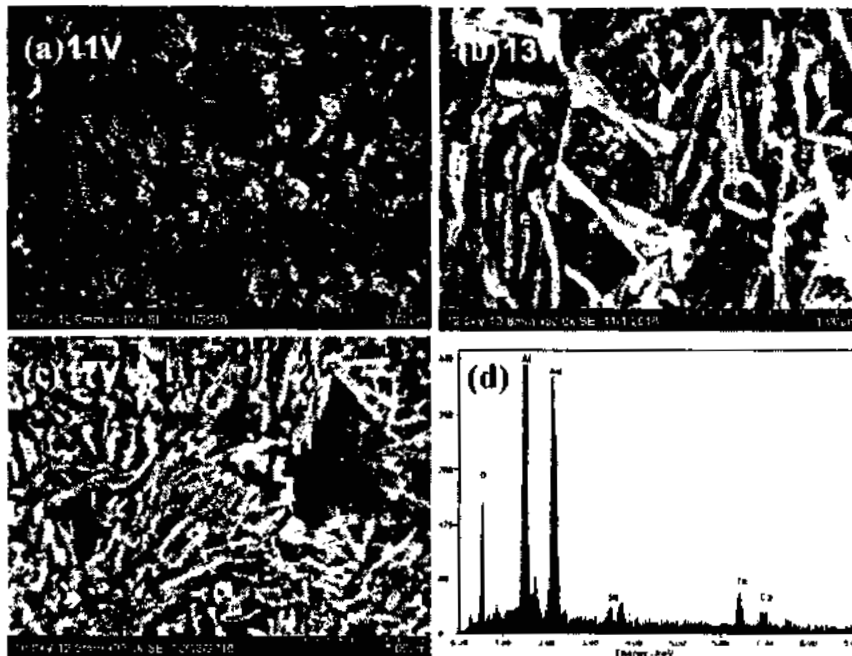


**Figure 6. 3:** (a-c) SEM images of  $Fe_2CoSn$  Heusler alloy NWs and (d) show EDX, conformation of  $Fe_2CoSn$  Heusler alloy NWs.

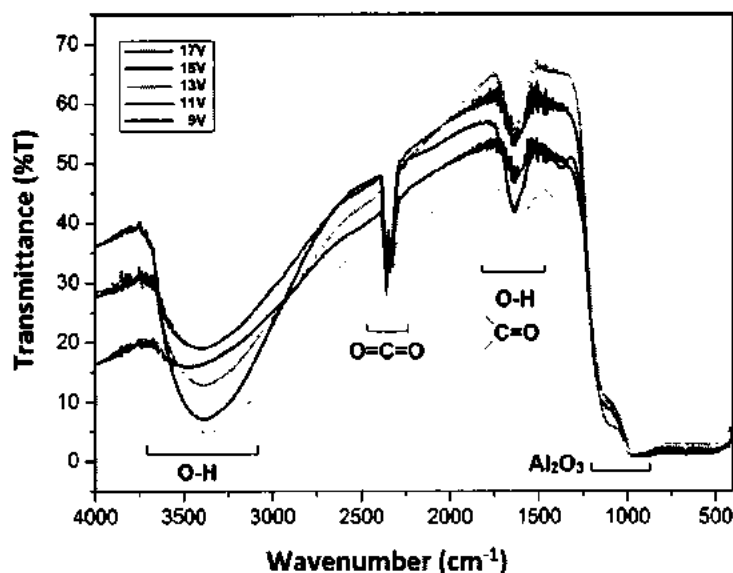


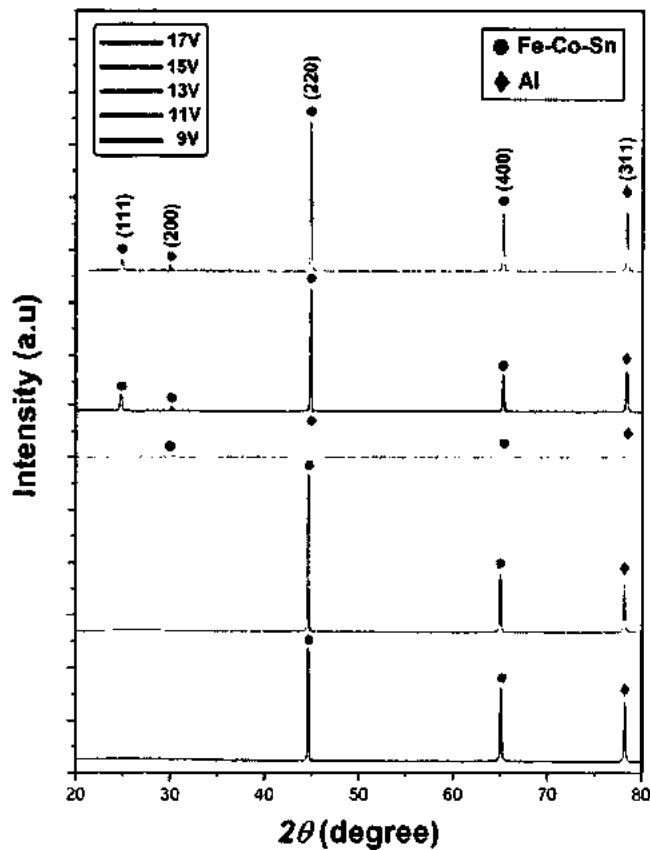
Figure 6. 4: The FTIR results of  $\text{Fe}_2\text{CoSn}$  Heusler alloy NWs.

Fig. 6.3(a-c) show the SEM images of Heusler alloys NWs which were confirmed from EDX shows in Fig. 6.3(d). These NWs were observed in SEM after the deposited samples dipped in 0.15 M NaOH aqueous solution for 1.5 hr at 60 °C to dissolve the templates and show clear images of aligned and non-agglomerated NWs.

The diameter of NWs ranges from 40 to 60 nm (Fig.6.3c) and length of the nanowires depends upon the deposition time and should be 15  $\mu\text{m}$ , which is not clear from SEM images because nanowires are broken during the preparation for SEM when we dissolved them in NaOH solution. It is also explained in our previous work with their mathematical formulae and in literature as well [176].

### 6.2.3. Surface Analysis

FTIR of NWs was examined within the AAO templates by using reflection mode in the range of 400-4000  $\text{cm}^{-1}$  as illustrated in Fig.6.4. To study the presence or absence of various vibration modes as well as the influence of voltage variation on chemical bonding between metal ions and impurities. Also metal-metal bond is not visible in FTIR. But NWs have a high aspect ratio (surface to volume ratio) as compared to their bulk counterpart of the same material. So that NWs influenced chemically more reactive, because of their dangling bonds, formed on the surface of NWs. Therefore, knowing the surface chemistry of Heusler alloy ( $\text{Fe}_2\text{CoSn}$ ) NWs,



**Figure 6. 5:** The XRD pattern of  $\text{Fe}_2\text{CoSn}$  Heusler alloy NWs deposited at different AC-voltages.

that had been synthesized, is of huge curiosity. The spectrum of all five samples are shown in Fig. 6.4.

In this spectrum, the peak in the region  $(900-1200) \text{ cm}^{-1}$  indicated the excitation of  $\text{Al}_2\text{O}_3$  bond. The sprinkle bands in a region  $(1650-1850) \text{ cm}^{-1}$  also correspond to the presence of bending vibration of a hydroxyl group and a carbonyl group. In the region around  $(2250-2330) \text{ cm}^{-1}$ , the bond of  $\text{CO}_2$  molecules was indicated which was present in the air. In all these spectrums, broadband was observed in the range  $(3200-3600) \text{ cm}^{-1}$  in all samples, can be assigned to the presence of hydroxyl group on the surface of samples. On the other end, no plasmonic effect was observed, that may be due to the attachment of vertically align NWs.

#### 6.2.4. Structure Analysis

X-rays diffraction (XRD) measurement of NWs were carried out in AAO templates along with Al-substrate. Crystallite of the synthesized sample was calculated by X-rays diffraction (XRD)

method using Debye Scherer formula exposing Cu-K $\alpha$  radiations:  $D = \frac{k\lambda}{\beta_{hkl} \cos \theta}$ . Where D is the grain size,  $k$  represents the correction factor (also known as shape factor),  $\lambda$  is incident X-ray (Cu K $\alpha$  = 1.5406Å),  $\theta$  is the peak position and  $\beta_{hkl}$  represents FWHM which takes in radians [214]. Diffraction patterns of all synthesized samples is depicted in Fig. 6.5, and the result was compared with standard data. Reflection peak (311) was observed in all samples which corresponded to Al-substrate, due to higher penetration depth of X-rays as compared to the lateral length of NWs.

XRD diffraction patterns of (Fe<sub>2</sub>CoSn) full Heusler alloys NWs could be divided into fundamental even super-lattice and odd super-lattice reflection [214, 215]. The fundamental reflection peaks can even be observed in the A2-type crystal structure while super-lattice reflections are only observed in the L2<sub>1</sub> crystal structure. It was observed that characteristic fundamental reflection peaks [(220) and (400)] and super-lattice diffraction peaks [(111) and (200)] were present in the nanowires that are deposited at 15V and 17V, which means NWs have higher order structure and corresponds to L2<sub>1</sub> crystal structure (space group *Fm3m*) which was confirmed from DFT result. While in NWs deposited at 13V had only even super-lattice reflection (200) observed along the fundamental reflection. The intensities comparison of peaks (400) and (200) with (220) suggests that NWs deposited at 13V may consist of B2 (space group *Pm3m*) as well as A2 cubic crystal structure (space group *Im3m*). Beside these reflection planes, a shift, as well as variation in intensity of diffraction peaks, have been observed with the increase in deposition voltage which indicates that deposition voltage affected on the order of chemical structure and composition. The lattice constants of super-lattice reflection containing NWs had been determined, as listed in Table.6.1. It was also observed that lattice constant of NWs deposited at 15V and 17V was greater than 13V which lie within the lattice parameter range of L2<sub>1</sub> crystal structure.

### 6.2.5. Compositional analysis

The EDX is a scientific tool by which we can determine the average elemental composition of our deposited samples (AC-electrodeposition) as shown in Fig.6.6.

The ratio of Co, Fe and Sn contents was confirmed from EDX, which varies w.r.t applied voltage. As voltage increases gradually the contents of magnetic ions (Fe & Co) increased as compared to non-magnetic ions (Sn). After the specific voltage (13), Co & Sn almost remained constant but Fe increased gradually up to 17 V, which indicated that different element showed



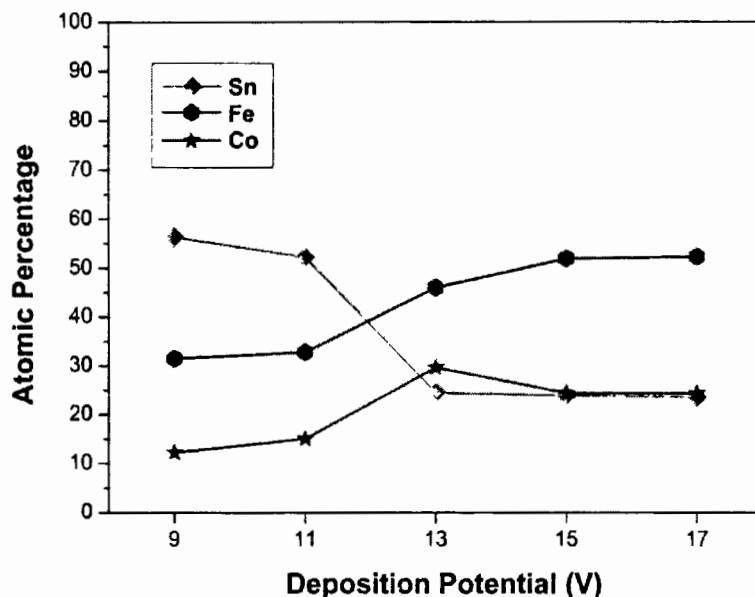


**Figure 6. 6:** Shows EDX pattern of deposited Fe, Co and Sn in Heusler alloy ( $\text{Fe}_2\text{CoSn}$ ) NWs at different AC-voltages

different reduction potential [216]. According to the result of EDX, the compositional ratio of Fe: Co: Sn at 13, 15 and 17 V was almost about 2.0: 1.0: 1.08, which is within the range of experimental error of the nominal 2:1:1 composition of  $\text{Fe}_2\text{CoSn}$ . Hence, our samples referred to as  $\text{Fe}_2\text{CoSn}$  Heusler alloy NWs, are confirmed through XRD and literature as well [204].

### 6.2.6. Magnetic Properties

Fig. 6.7(a) shows the hysteresis loops which explained the magnetic properties of all the electrodeposited samples at different AC voltages measured at room temperature which confirm ferromagnetic NWs. Fig. 6.7(b) displays that coercivity ( $H_c$ ) and saturation magnetization ( $M_s$ ) depend on the reduction potential from 9 to 17 V. The coercivity reaches to its maximum peak value, 484 Oe at 17 V from 200 Oe at 9V which shows that our sample was a soft magnetic material. The increasing/decreasing rate of coercivity and saturation magnetization as a function of deposition potential was observed. Here the length of the NWs was almost the same, lies in the range of 15 microns. The magnetostatic interactions between NWs were expected to be same, as using the same AAO template to synthesize Heusler alloy NWs. The coercivity increases sharply during the formation of  $\text{Fe}_2\text{CoSn}$  Heusler alloy NWs due to a decrease of diamagnetic tin (Sn) content and increase in ferromagnetic (Fe & Co) which also affects its specific structure and composition ( $\text{Fe}_2\text{CoSn}$ ). The highest coercivity was obtained for sample deposited at 17 V. At higher potential, the deposition of tin and the

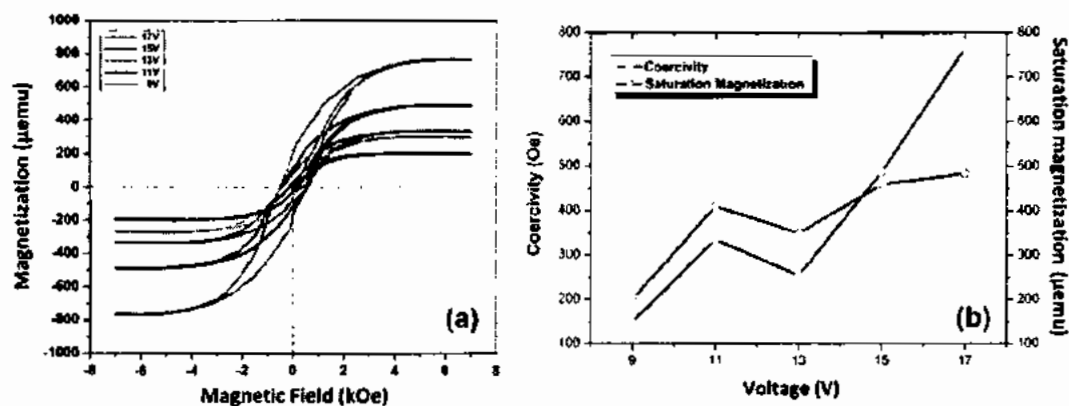


**Figure 6. 7:** (a) The Hysteresis loops of the samples deposited at different AC voltages from 9 to 17 V in 60 sec (b) the dependence of coercivity and saturation magnetization of the deposited samples at different AC voltages.

composition of  $\text{Fe}_2\text{CoSn}$  Heusler alloy NWs produces defects and makes the nanowires into tiny magnets. These disordered defects were spread throughout nanowires causing the blocking of domain walls and increment in magneto-crystalline anisotropy [217]. That influences the squareness (squareness =  $M_R/M_S$ ) of Heusler alloy NWs as illustrated in Table. 6.1. Squareness shows a linear trend as a function of deposition potential which may be due to an increase in grain size w.r.t increase in deposition potential as shown in Table. 6.1. The coercivity 200 to 484 Oe of the Heusler alloys  $\text{Fe}_2\text{CoSn}$  synthesized by A.C electrodeposition is reported in our present work which makes them feasible for many practical applications such as engineering industries also these hard magnetic material alloy are extensively used as permanent magnets in our daily products such as generators loudspeakers and motors etc. These alloys have replaced the rare-earth with 3d metals alloys which have limited thermal stability and low magnetization also explained elsewhere [210].

**Table 6. 1:** Show the different experimental results varies w.r.t deposition voltage.

V	at.%			Å	nm	Oe	μemu	μemu	S*
	Fe	Co	Sn						
9	31.48	12.22	56.29	-	34.4	200	150	25	0.17
11	32.74	15.04	52.21	-	35.9	410	335	73	0.21
13	45.98	29.58	24.43	5.69	33.2	350	254	56	0.22
15	51.84	24.35	23.80	5.75	36.6	460	488	112	0.23
17	53.18	23.28	23.52	5.75	37.7	484	765	185	0.24

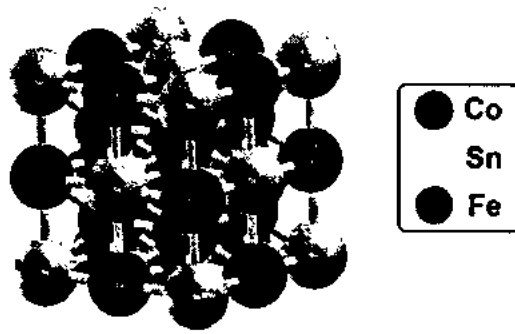


**Figure 6. 8:** The crystal structure of Fe<sub>2</sub>-based (Fe<sub>2</sub>CoSn) full Heusler compound NWs

### 6.2.7. Computational Results

Crystal structure of Fe<sub>2</sub>CoSn is shown in Fig.6.8, Co atoms are shown in blue, Fe in red and Sn in grey color. Sn atoms lie at the 4a (0.0, 0.0, 0.0), Fe atoms at 8c (0.25, 0.25, 0.25) and Co at 4b (0.5, 0.5, 0.5), the resulting structure belongs to space group Fm3m [214]. To find out the electronic structure and magnetic properties of Fe<sub>2</sub>CoSn Heusler alloy we have employed full potential linearized augmented plane wave (FP-LAPW) methods for the solution of Kohn-Sham equations as implemented in WIEN2k package [197]. Muffin tin radii are taken to be 1.83 a.u. for all three atoms in the basis. The generalized gradient approximation (GGA) was used for exchange and correlation functional. Plane wave cut-off was defined by  $RK_{\max} = 8.0$ ,

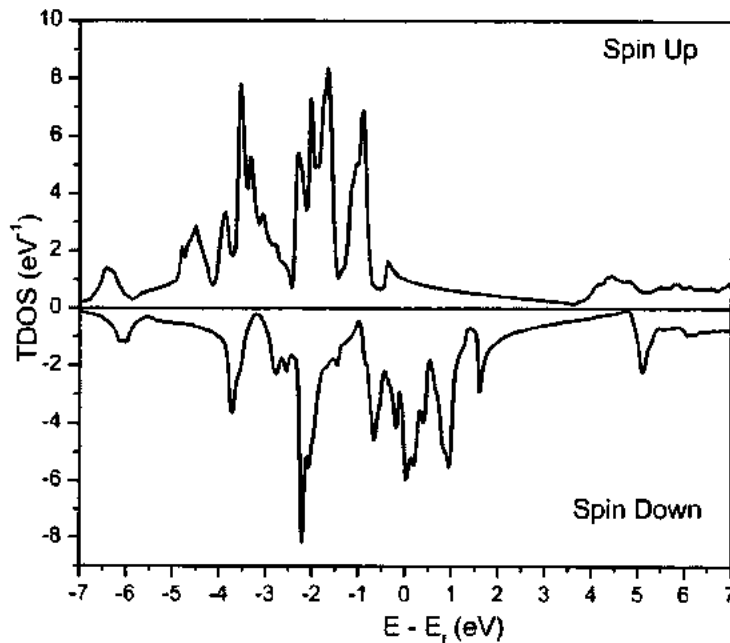


**Figure 6. 9:** Calculation of TDOS for Fe<sub>2</sub>-based (Fe<sub>2</sub>CoSn) full Heusler compound NWs.

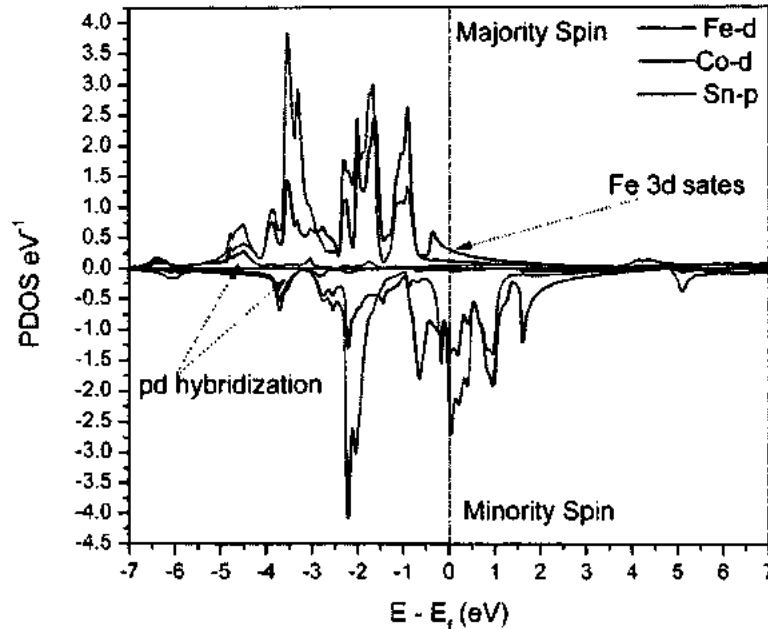


**Figure 6. 10:** Calculation of PDOS for Fe2-based ( $\text{Fe}_2\text{CoSn}$ ) full Heusler compound NWs.

and a number of the plane wave was adjusted by  $G_{\text{max}} = 14 \text{ (Ryd)}^{-1}$ . A fine mesh of  $21 \times 21 \times 21$  k points is made for the integration over Brillouin zone (BZ) with 286 k- points in an irreducible wedge of Brillouin zone (IBZ).

Spin-polarized total density of states (TDOS) can be seen in Fig.6.9. We can see that there are few states at the Fermi level in majority spin channel, these are Fe-3d states and are shown in Fig.6.10 (PDOS). If these states were not there the compound would be half-metallic like all other compounds of the series. However, these states are very few and have a little contribution to conduction when compared to minority spin channel.

Electronic band structure tells the bonding and character of electrons bands. DFT is a standard tool to calculate BS for materials to determine different properties of solids [199]. We employed LAPW methods for calculations of electronic BS of  $\text{Fe}_2\text{CoSn}$  which was shown in Fig.6.11. The valence band is mainly composed of 3d states of Fe and Co hybridized with Sn 5p states. There are some states in majority spin channel which makes this compound to be fully metallic instead of half-metallic like other full Heusler compounds. Calculations for Ferromagnetic ground state of  $\text{Fe}_2\text{CoSn}$  gives a total spin magnetic moment of  $7.29 \mu_B$ . However, these states are very few in number and do not contribute too much in conduction when compared to minority spin channel. This imbalance of charge transport through different spin channels can be viewed as half-metallic type behavior.

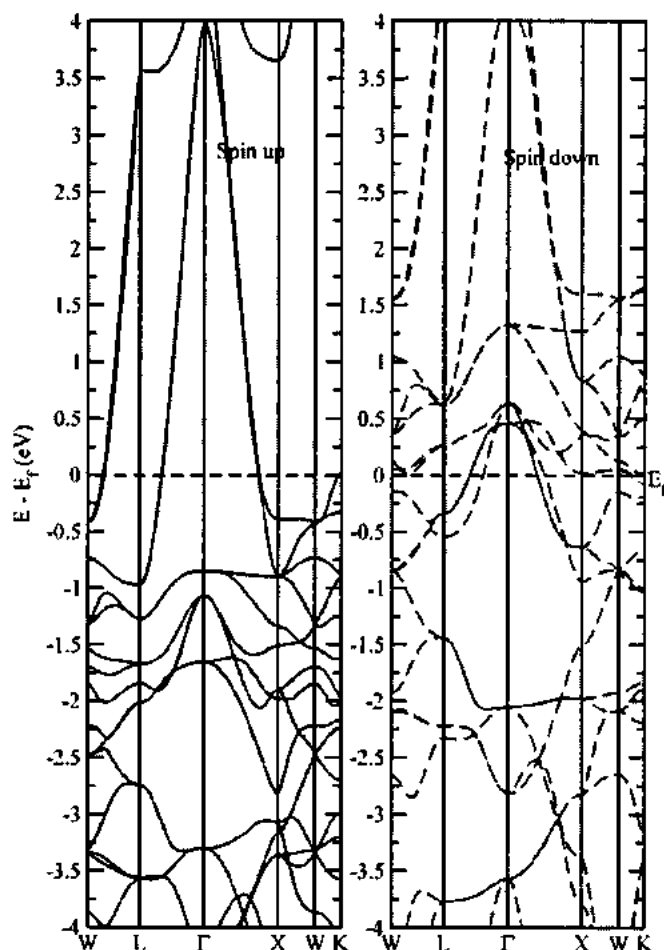


**Figure 6. 11:** Band structure of majority and minority spin states Fe2-based ( $\text{Fe}_2\text{CoSn}$ ) full Heusler compound NWs.

### 6.2.8. Electrical Properties

The electrical properties of Heusler alloys  $\text{Fe}_2\text{CoSn}$  NWs synthesized by A.C electrodeposition were characterized by two probes (Fig.6.12) and four-probe (Hall technique) Fig. (6.13 & 6.14). The electrical properties were measured using “Swin Hall 8800, China” without pelletization. Before the start of electrical characterization, first the samples were dipped in the 0.15 M NaOH aqueous solution for 1 hr at 60 °C, through which templates (work as insulator) were removed from the upper part of NWs while in the lower remained there to support the NWs in the standing mode and produced no hurdle during the characterizations.

#### 6.2.8.1. I-V Measurement

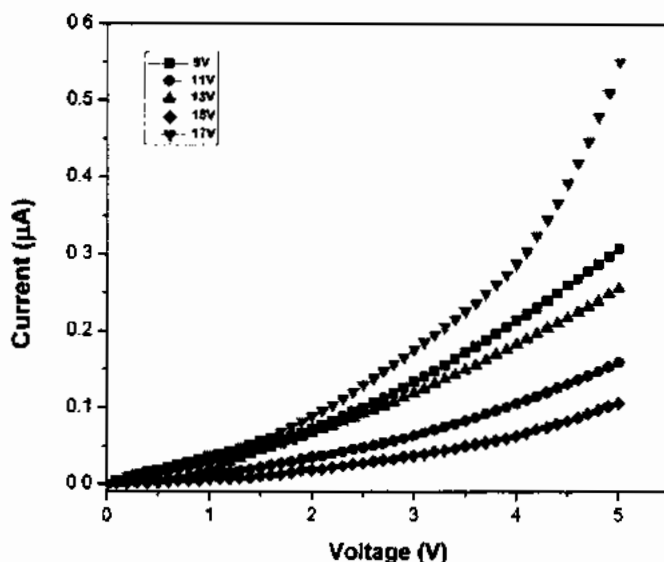


**Figure 6.12:** The variation of Current w.r.t deposition voltage.

The resistance ( $R$ ) was measured as a physical quantity using two probe  $I$ - $V$  measurements. In Fig.6.12, the curve between current and voltage was not a straight line showing non-ohmic characteristic which is a good sign for the use in spintronic devices (spin-dependent tunneling) as briefly explained in the above portion of the paper.

#### 6.2.8.2: Hall Measurements

To measure the transport property of Heusler alloy NWs experimentally, the four-probe (Hall) technique was developed through which we characterized our samples that depended on the

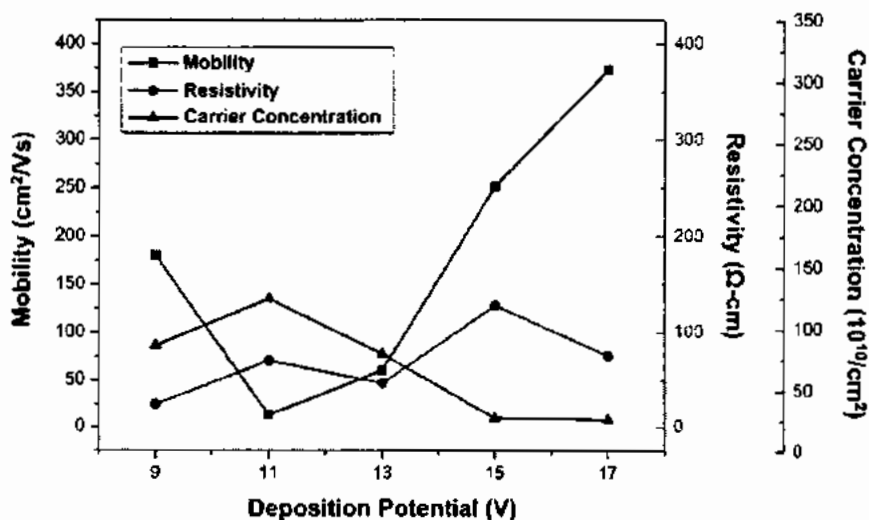


**Figure 6.13:** The variation of mobility, resistivity and carrier concentration w.r.t deposition voltages.

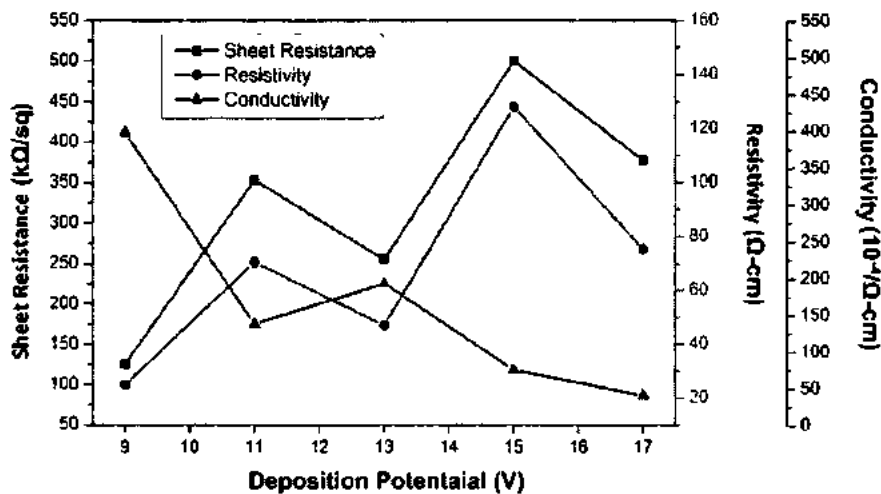


**Figure 6. 14:** The variation of sheet resistance, resistivity and conductivity w. r. t deposition voltages.

Lorentz force. The variation of mobility, carrier concentration and resistivity of Heusler alloys ( $\text{Fe}_2\text{CoSn}$ ) NWs with different deposition voltages (9 to 17 V) were shown in Fig. 6.13. The resistivity was slightly increased and then decreased from 9 to 13 V, whereas mobility first decreased from 9 to 11 V, and then increased sharply from 13 to 17 V, which show the enhancement of the crystallinity i.e. Grain size increased and reduced the scattering of electron grain boundary that decreased the resistivity of Heusler alloy  $\text{Fe}_2\text{CoSn}$  NWs. The resistivity of Heusler alloy NWs was measured from 25 to 128  $\Omega\text{-cm}$ . whereas mobility was observed relatively high, of the order 13.6 to 375  $\text{cm}^2/\text{Vs}$ . Maximum mobility was measured at 15 and 17 V, leading towards excellent transport property. The carrier concentration was calculated of the order  $10^{10}/\text{cm}^2$  and showed similar behavior as that of resistivity [218]. Fig.6.14 shows the relation between sheet resistance, resistivity and conductivity.

It confirms the inverse relation between (sheet resistance, resistivity) and conductivity. These experimental results were confirmed from theoretical formulae.

Mathematically the magnitude of Hall voltage was calculated by;

$$\text{Hall voltage}(V_H) = IB/qnd \quad 6.3$$

Where  $I$  is the current,  $B$  is the magnetic field,  $d$  is the sample thickness, and  $q$  ( $1.602 \times 10^{-19} \text{ C}$ ).

Mathematically the carrier concentration ( $n$ ) was calculated by;

$$n = IB/qdV_H \quad 6.4$$

Carrier concentration ( $n$ ) in above Equation can be measured, when all the remaining parameters are known,

Sheet density ( $n_s$ ) can be measured using Hall voltage.

$$\text{Sheet density}(n_s) = IB/q|V_H| \quad 6.5$$

The sheet resistance of the Heusler alloys NWs can be measured by using the Van Der Pauw resistivity technique. Which comprises both mobility and sheet density.

$$\text{Mobility}(\mu) = |V_H|/R_S IB \quad 6.6$$

Using Eq.6.3 we get;

$$\text{Mobility}(\mu) = 1/qn_s R_S \quad 6.7$$

We know that the Hall coefficient is given by

$$\text{Hall coefficient} (R_H) = V_H W / BI \quad 6.8$$

If we can measure the value of Hall coefficient, then mobility can also be measured by using Eq.6.8.

$$\text{Mobility}(\mu) = \text{Hall coefficient}(R_H) / \text{Resistivity}(\rho) \quad 6.9$$

Whereas resistivity of the desired sample can be calculated from the sheet resistance if we know the thickness of the sample.

$$\text{Resistivity}(\rho) = \text{Sheet resistance}(R_S) \times \text{thickness}(t) \quad 6.10$$

These mathematical/theoretical formulae are obeyed to fulfill the results taken from the experiments (Two and four probe) techniques.

The electrical control of the magnetized switching is highly desirable in ferromagnetic NWs in future spintronic applications and the capability of spintronics devices intensely depends on the source of spin-polarized current [58]. However, the Hall mobility values exhibit an opposite trend and decrease with annealed films. The similar decreasing trend of Hall mobility has also been observed in  $\text{Cu}_2\text{ZnSnS}_4$  thin films fabricated by a vacuum method with expending annealing time which may be attributed to the increase of the inter-grain potential barrier [219]. The practical applications of  $\text{Fe}_2\text{CoSn}$  Heusler alloys NWs devices, in which the planar Hall voltage in the ferromagnetic layer is tuned solely by piezo voltages as well as magnetic and opto-magnetic properties have been investigated by Buschow *et al* for bulk materials [220], and a spin filtering device (SFD) by Moodera *et al* [221].



---

---

## **Chapter No. 7**

---

---

## Chapter No. 7

### Morphology, structural and magnetic properties of $\text{Fe}_{100-x}\text{Cu}_x$ alloy nanowires

#### 7.1. Introduction

One-dimensional nanomaterials have got more focus because of the requirements of fundamental technical applications and physical researches in nano-devices [222-224]. Current research material such as Cu has excellent physicochemical properties, high electrical conduction, good biocompatibility and high surface activity. Presently, researchers are looking for new routes to the synthesis of ferromagnetic-nonmagnetic alloys NWs to enhance their properties in micro and nanodevices [225]. Nowadays, the focus of concentration has been got by NWs fabrication of arrays, due to its potential use in high-density perpendicular recording magnetic memories [226], sensors, giant magnetoresistance (GMR) [227, 228] and magneto-electronic devices [229, 230]. The occurrence of stimulating and remarkable variation in magnetic and structural behavior can be expected during the synthesis of alloy (FeCu), the iron (ferromagnetic) with copper (diamagnetic) through electro-deposition technique. It is a matter of great attention to study the relation of magnetic/structural properties with deposition parameters. Many practices are focused on synthesis of magnetic NWs [231]. The method of template-assisted electrodeposition is one of the simplest, easily controlled and inexpensive technique. The porous alumina is an attractive and smart way for the synthesis of NWs as it has uniform pore distribution, high pore density as well as the desired pore diameter/length [232, 233]. Ferromagnetic NWs such as Co, Ni and Fe, as well as their alloys, were fabricated by the porous membrane (AAO templates), have uniaxial anisotropy through easy axis parallel to the wire axis that produces the shape anisotropy of NWs [234-237]. This result could be remarkable for the structural and magnetic properties of FeCu NWs. The effective plating parameters such as current density and bath composition are well-known for the modification of compositional alloy NWs [238]. In the present effort, the structural and magnetization behavior of FeCu NWs, prepared by AC-electrodeposited from sulphate bath solution through different ratio ( $\text{Fe}_{100-x}\text{Cu}_x$ ) in the aqueous bath with constant AC-potential have been studied.

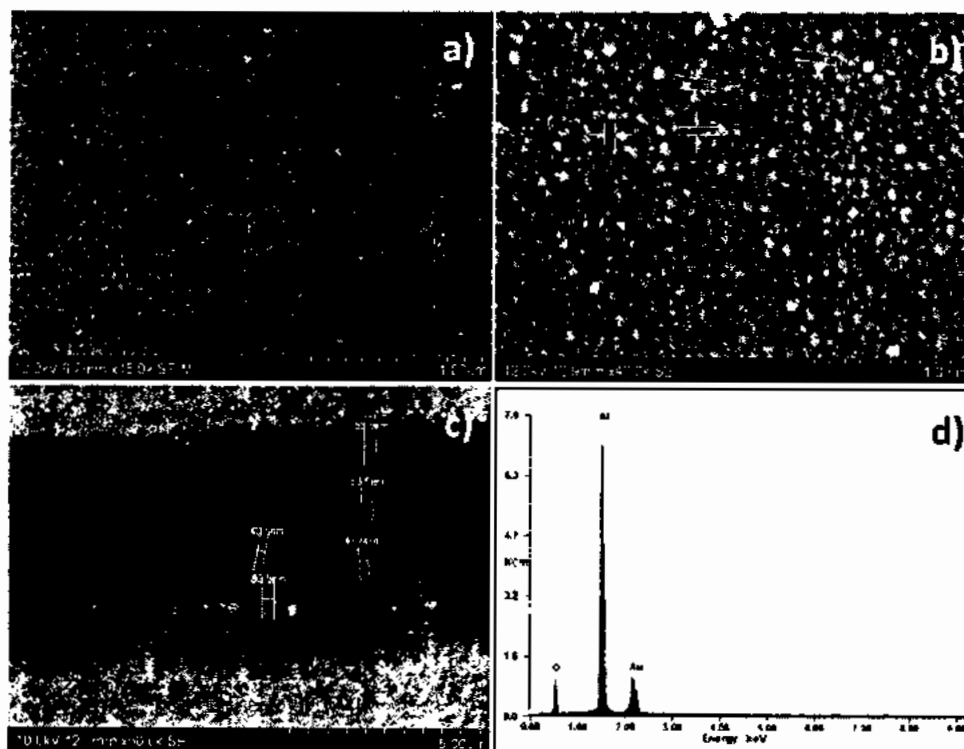


**Figure 7. 1:** SEM image of AAO template after second step anodization, (b)SEM image of AAO template after 30 min immersing in phosphoric acid and (c) the cross-section SEM image of AAO template (d) the EDX of templates.

## 7.2. Results and discussion

### 7.2.1. Morphology of AAO templates

The AAO templates were synthesized by two steps of anodization, by means of 5% of  $H_3PO_4$  (aqueous solution) as explained in the experimental portion. Fig.7.1(a & b) shows the morphology of the templates from a typical top view, after the completion of the 2<sup>nd</sup> step of anodization without immersed in  $H_3PO_4$  solution and immersed in 1 M  $H_3PO_4$  solution for 25 min respectively, which effect to increase the diameter up to 10%. These templates were homogeneous, regular and hexagonal in shape.

As illustrated in Fig.7.1C, showed the lateral view that confirmed their regular, aligned shape and length was placed in the range of 10  $\mu m$ . The top view SEM images with an average pore diameter and interpore distance were 50-65 nm and 120-130 nm respectively as shown in Fig.7.1b. Fig.7.1d (EDX) confirms the chemical composition of AAO templates.

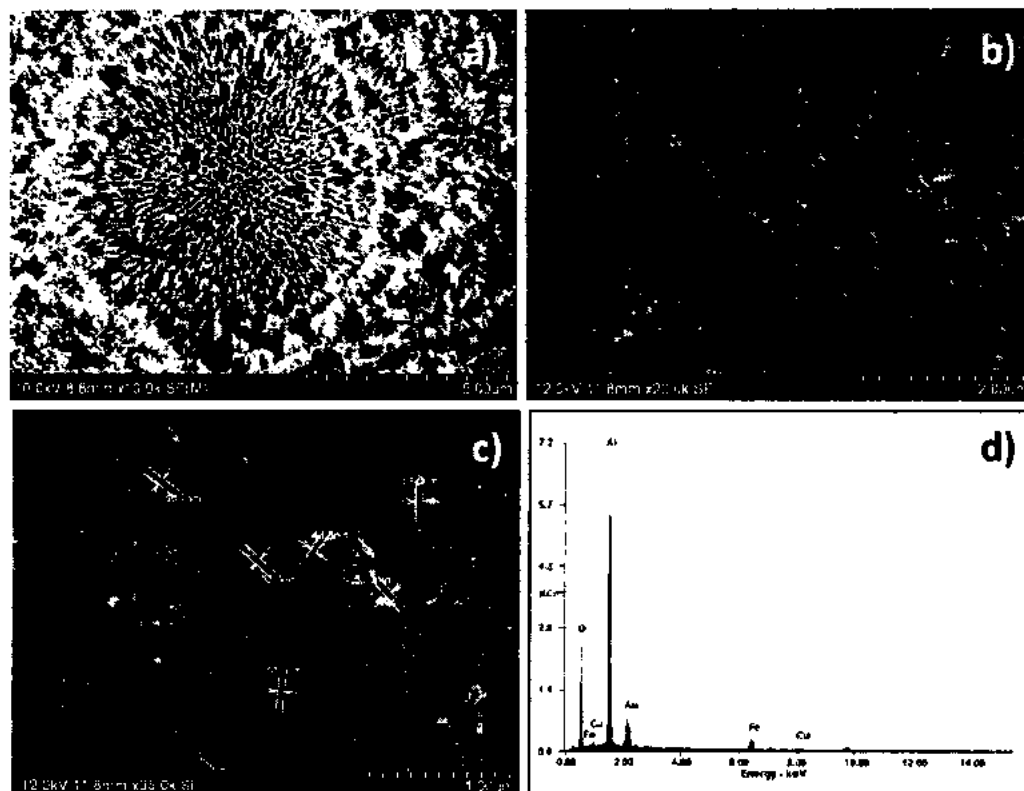


**Figure 7. 2:** Shows the SEM images of FeCu NWs after removing the AAO templates, (a) SEM image of FeCu NWs at 5  $\mu\text{m}$  scale, (b) SEM image of FeCu NWs at 2  $\mu\text{m}$  scale, (c) SEM image of FeCu NWs at 1  $\mu\text{m}$  scale and (d) Shows EDX of FeCu NWs.

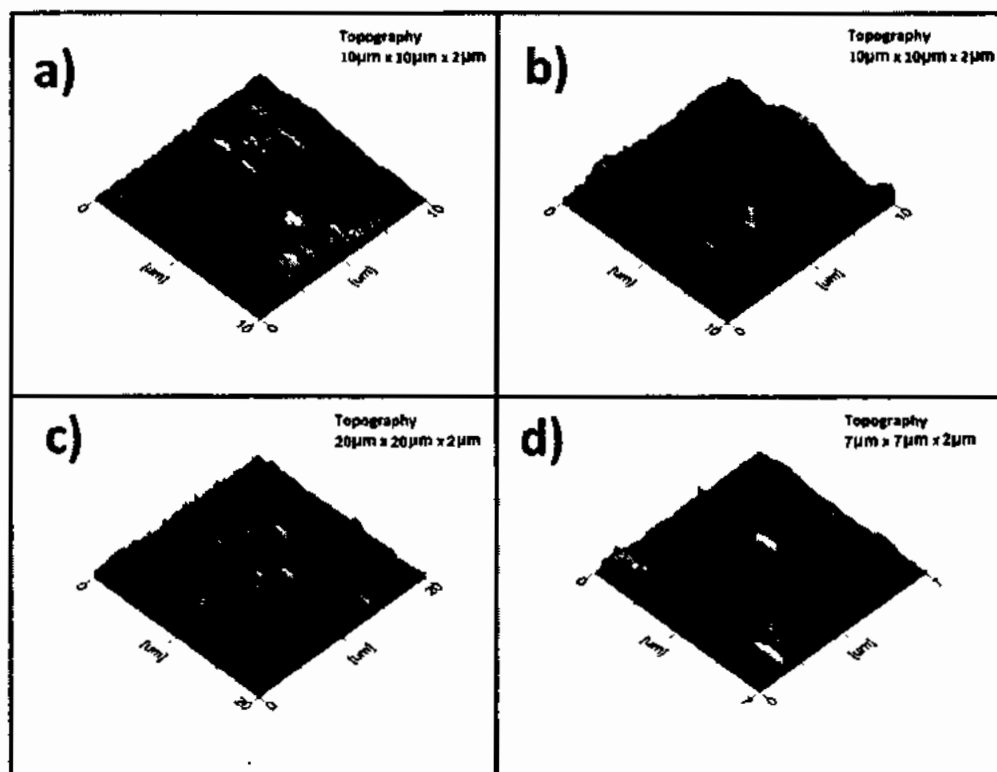
### 7.2.2. Morphology of FeCu Alloy NWs

Fig. 7.2(a-c) displays the SEM micrograph of FeCu NWs after dissolving the templates in 1.0 M of sodium hydroxide (NaOH) aqueous solution. These images confirmed the diameter of FeCu NWs were in the range of 50-56 nm and the length was estimated in 10  $\mu\text{m}$  according to the full depth of AAO membranes.

The concentration variation of iron sulfate ( $\text{FeSO}_4 \cdot 7\text{H}_2\text{O}$ ) bath was taken from 100 to 69 % w.r.t variation of copper sulfate ( $\text{CuSO}_4 \cdot 5\text{H}_2\text{O}$ ) bath from 0 to 31% simultaneously as given in Table 7.1. The Cu ions in deposited FeCu NWs was increased with an increase in the amount of Cu concentration, in the electrolyte bath solution. The composition analysis of Fe and Cu in the synthesis of FeCu alloy NWs with different bath configuration were obtained from EDX (Fig. 7.2d) as shown in Table 7.1.

### 7.2.3. Surface Analysis

The surface analysis of AAO templates and NWs (without dissolving in NaOH) was observed



**Figure 7. 3:** (a &b) The AFM images of AAO template after second step anodization and (c &d) the AFM images of FeCu NWs after removing the AAO templates.

through Atomic force microscopy (AFM) technique as shown in Fig. 7.3 (a & b) and Fig. 7.3(c & d) respectively. That technique provides a commanding tool to get qualitative confirmation deprived of any effect on their physical structure. The average surface roughness of AAO templates and FeCu NWs were found to be  $2\mu\text{m}$ , which provided supporting evidence of the SEM results. Fig.7.3 also confirmed the homogeneity and uniform morphology of our samples.

#### 7.2.4 Structural Analysis of FeCu Alloy NWs

The crystal structure of the synthesized samples ( $\text{Fe}_{100-x}\text{Cu}_x$ ) NWs were investigated with the XRD technique using Debye Scherrer formula;  $D = \frac{k\lambda}{\beta_{hkl} \cos \theta}$  exposing Cu-K $\alpha$  radiations ranges from  $20^\circ$  to  $70^\circ$  as shown in Fig.7.4. where  $\theta$  is the peak position,  $\lambda$  is wave length of incident X-ray; Cu K $\alpha = 1.5406\text{\AA}$  and  $\beta_{hkl}$  indicate FWHM (full width at half maximum) which takes in radians and  $k = 0.9$ , known as shape factor.

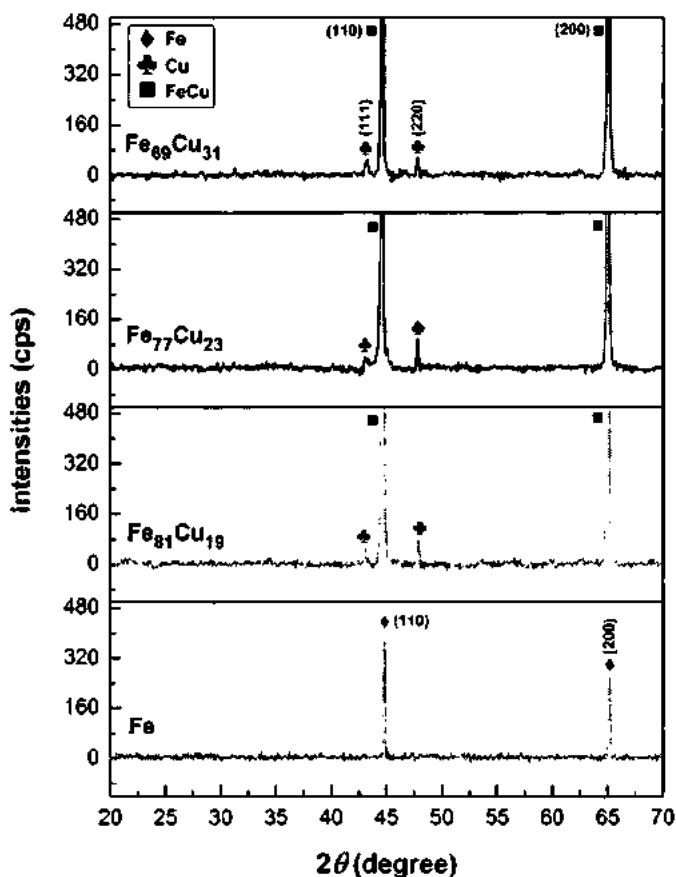
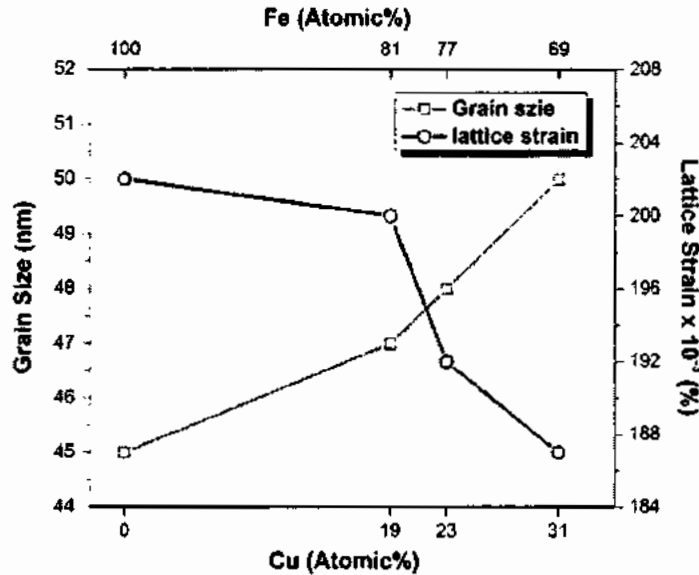


Figure 7. 4: XRD spectra of FeCu NWs arrays of various content (at %) embedded into AAO templates.

The XRD pattern of all synthesized samples were characterized without dissolving the templates in NaOH solution. The experimental results were compared with the standard data (JCPDs # 01-071-7667 & 01-080-5766). Sample first was synthesized through pure Fe-NWs reflect *bcc* crystal structure with the Miller indices (110) and (200) planes. As we added the concentration of Cu with Fe bath solution ( $Fe_{100-x}Cu_x$ ) as shown in table 7.1. Then *bcc* crystal structure of  $Fe_{81}Cu_{19}$  alloy NWs with reflection planes (110) and (200) were observed at  $2\theta = 44.685^\circ$  and  $2\theta = 65.071^\circ$  respectively along with Cu-*fcc* reflection planes (111) and (220) at  $2\theta = 38.388^\circ$  and  $2\theta = 47.899^\circ$  respectively as shown in Fig.7.4. So the Fe-*bcc* peaks were completely suppressed as a function of Cu contents increases in the synthesis of FeCu alloy NWs in all remaining samples. And the shift was observed towards the lower angle as we increase the concentration of Cu contents in the synthesis of *bcc*  $Fe_{77}Cu_{23}$  NWs at  $2\theta = 44.657^\circ$  and  $2\theta = 65.052^\circ$ . The same trend was observed in shifting the  $Fe_{69}Cu_{31}$  NWs peaks (110) and (200) towards lower angle at  $2\theta = 44.625^\circ$  and  $2\theta = 65.024^\circ$  respectively. Also, the grain size



**Figure 7. 5:** The variation of grain size and lattice strain of pure Fe and FeCu alloy NWs as a function of  $Fe_{100-x}Cu_x$  content (at %).

was calculated through XRD which shows increasing order as we increase the concentration of Cu in  $Fe_{100-x}Cu_x$  alloy NWs and lattice strain was decreased as shown in Fig 7.5. The shift produced towards lower angle was attributed due to stress, strain and lattice parameters of FeCu NWs. The lattice strain was decreased as we increased the concentration of Cu in  $Fe_{100-x}Cu_x$  NWs that affected the increment of lattice parameter [239] which illustrates the polycrystalline nature of FeCu NWs.

### 7.2.5. Magnetic Properties of FeCu Alloy NWs

The magnetic properties of ( $Fe_{100-x}Cu_x$ ) NWs were characterized through VSM at room temperature. The hysteresis loops of pure Fe and FeCu alloy NWs with different Cu at%, were studied parallel ( $0^\circ$ ) and perpendicular ( $90^\circ$ ) to wire axis, as shown in Fig.7.6 & Fig.7.7 respectively. The coercivity ( $H_c$ ) and squareness ( $M_R/M_S$ ) of all synthesise samples (Fe & FeCu NWs) were plotted as a function of Cu at% to observe the influence of composition on

**Table 7. 1:** Show chemical and structural parameters of electrodeposited FeCu NWs as a function of different composition contents (at %).

Samples	Electrochemical Bath Conc. $FeSO_4 \cdot 6H_2O$ / $CuSO_4 \cdot 5H_2O$	Measured Composition by EDS Fe (at%) : Cu (at%)	Alloys	Grain Size (nm)	Lattice Strain ( $\times 10^{-3}$ %)	Lattice Parameter (Å)
1	0.1M / -	100 / -	Fe	44.89	202.71	2.857
2	0.1M / 0.01M	81 / 19	$Fe_{81}Cu_{19}$	46.24	199.41	2.865
3	0.1M / 0.02M	77 / 23	$Fe_{77}Cu_{23}$	47.21	191.79	2.867
4	0.1M / 0.03M	69 / 31	$Fe_{69}Cu_{31}$	49.17	186.46	2.869

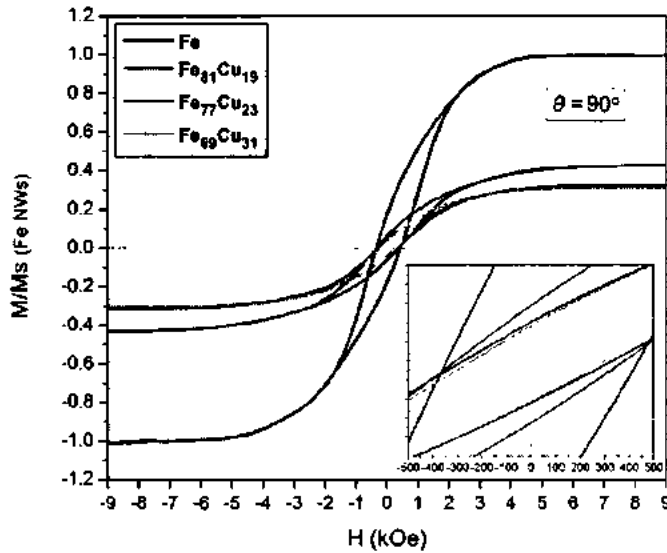


**Figure 7. 6:** Hysteresis loops of electrodeposited pure Fe and FeCu NWs perpendicular to the plane of the membrane with different Fe<sub>100-x</sub>Cu<sub>x</sub> content (at %) at a constant voltage (16V).The inset shows an enlargement of the central part of the loop.

magnetic properties, as illustrated in Fig.7.8 (a & b). The coercivity ( $H_c$ ) and squareness ( $M_R/M_S$ ), both were decreased significantly as a function of increasing Cu at% in FeCu alloy NWs as shown in Table 7.2. The coercivity ( $H_c$ ) was decreased expressively from 421 to 389 Oe and from 389 to 342 Oe, parallel and perpendicular to wire axis respectively as Cu at% increases from 0% to 19%. Further, the coercivity shows gradually decreasing order as we increases the concentration of Cu (at %) from 19% to 31% as shown in Fig.7.8 (a & b). The crystal anisotropy, shape anisotropy and magneto-static interactions play a vital role that stimulates the magnetic properties of the magnetic NWs [18]. In present case, the FeCu alloy NWs length was almost equal and placed in the range of 10  $\mu\text{m}$ , which was expected to be the same magneto-static interactions between NWs having identical templates (same diameter and length) were used to synthesize all samples (FeCu alloy NWs). Moreover, the coercivity ( $H_c$ ) is inversely dependent on grain size, as grain size was increased and reduced the lattice strain due to increase of Cu atoms (at%) in FeCu NWs that influenced to decrease the coercivity ( $H_c$ ) of the NWs. The remanence ( $M_R$ ) and saturation magnetization ( $M_S$ ) were decreased sharply with the addition of Cu (0% to 19%) concentration in Fe (Fe<sub>81</sub>Cu<sub>19</sub>) bath solution as shown in Table 7.2. These properties can be effected due to difference in their energies of Fe and Cu. The element with lower surface energy has tendency to segregate on to the surface of FeCu NWs; Fe = 2.613 eV atom<sup>-1</sup> and that of Cu = 1.377 eV atom<sup>-1</sup>.



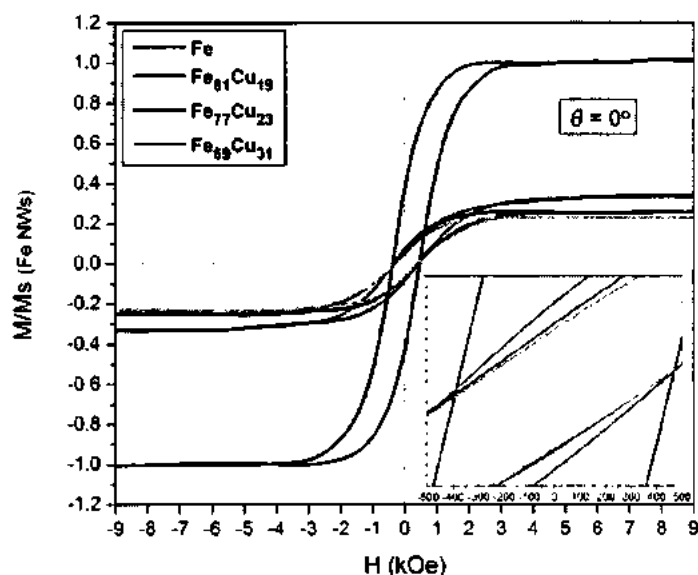


**Figure 7. 7:** Hysteresis loops of electrodeposited pure Fe and FeCu NWs parallel to the plane of the membrane with different  $\text{Fe}_{100-x}\text{Cu}_x$  content (at %) at a constant voltage (16V). The inset shows an enlargement of the central part of the loop.

It shows that Cu which is diamagnetic (non-magnetic) having an atomic radius greater than Fe, the alignments of the magnetic moment of ferromagnetic is suppressed in Fe at high at%. Hence, the NWs with low Cu at% are difficult to demagnetize, compared to those samples with higher Cu at%. Unlike Szpunar et al, who observed that the grain size has not any prominent effect on saturation magnetization ( $M_s$ )[240]. But here, the result was observed experimentally, that remanence ( $M_R$ ) and saturation magnetization ( $M_s$ ) decreases with increase in grain size as the Cu at% was increased during the synthesis of FeCu alloy NWs as shown in Table 7.1 & Table 7.2. It was calculated through Scherrer formula that the grain size of FeCu NWs was increased from 44.89 nm (pure Fe) to 49.17 nm ( $\text{Fe}_{69}\text{Cu}_{31}$ ) NWs. Remanence ( $M_R$ ) and saturation magnetization ( $M_s$ ) for Cu rich (FeCu) NWs reveal that the magnetic

**Table 7. 2:** Show various magnetic parameters of electrodeposited FeCu NWs as a function of different composition contents (at %)

Samples	Alloys	Coercivity (Oe)		Saturation Magnetization ( $\text{emu} \times 10^{-6}$ )		Retentivity ( $\text{emu} \times 10^{-6}$ )		Squarness	
			⊥		⊥		⊥		⊥
1	Fe	421	389	1704	1898	790.65	406.17	0.464	0.214
2	$\text{Fe}_{81}\text{Cu}_{19}$	389	342	572	776	129.27	133.47	0.226	0.172
3	$\text{Fe}_{77}\text{Cu}_{23}$	365	302	454	592	101.24	99.45	0.223	0.168
4	$\text{Fe}_{69}\text{Cu}_{31}$	356	296	415	577	92.13	95.72	0.222	0.166

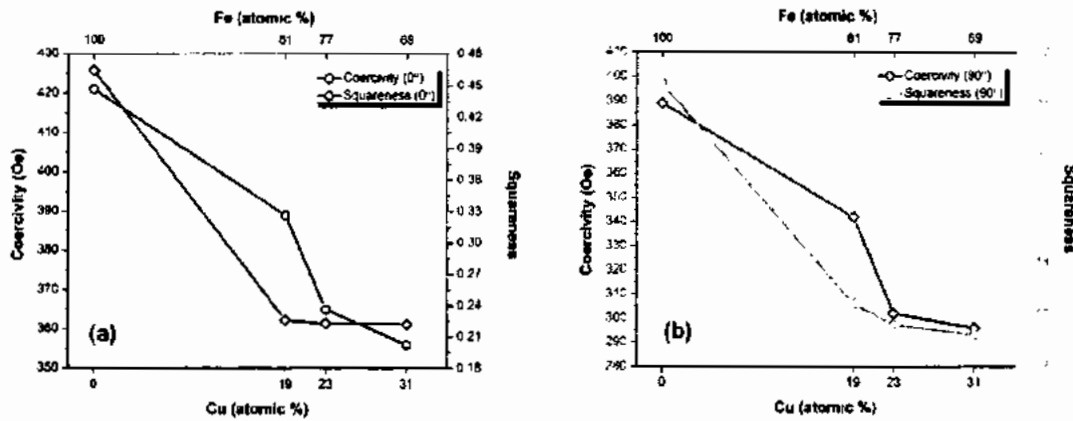


**Figure 7. 8:** Behavior of coercivity and squareness (a) Parallel and (b) Perpendicular to NWs long axis as function of Fe and Cu content in NWs

energy which aligns the copper magnetic moments, increases due to substantially increase in the number of Cu-Cu interaction. The squareness ( $M_R/M_S$ ) determines the easy and hard axes of the NWs, i.e the greater squareness value refer to easy the axis. Thus, our FeCu NWs have easy an axis along the NWs due to its large squareness value at  $0^\circ$ .



---

## **Chapter No. 8**

---

## Chapter No. 8

### Structural, Magnetic and Electrical investigations of $\text{Fe}_{1-x}\text{Mn}_x$ ( $0 \leq x \leq 0.39$ ) alloy Nanowires via Electrodeposition in AAO templates

#### 8.1. Introduction

Recently, the shape memory alloys attracted a lot attention due to application point view. C. M. Wayman discovered the shape memory effect in Fe-based alloy [241]. Since the shape memory effect and super elasticity of Fe-based nanostructure, such as FeMnSi and FeMn alloys that produced numerous interest due to their implementation in sensors, magnetic random access memory (MRAM) and other several potential applications [242, 243]. Particularly, to enhance the efficiency of spintronics devices such as race-track memories by using NWs that were synthesized through electrodeposition which is one of the most active current research fields [41, 244]. In future spintronics device that require spin-valves to inject the spin polarize current, need to fix one of the ferromagnetic material to anti-ferromagnetic which form their specific structure [245]. The iron-based ferromagnetic material couple with non-ferromagnetic like Manganese at nanoscale shows magnetically soft composite due to interfacial exchange coupling [246, 247].

The existence of the biologically alloys, such as Fe-based FeMn biodegradable alloy, that seems to be more suitable than nickel based; the anterior being necessary for humanoid [248, 249] and the nickel classified as a carcinogenic and a toxic [250]. Manganese is observed not to be toxic in cardiovascular system at a higher ratio [251-253]. The Mn from such alloy due to its controlled degradation could be acknowledged to be less than their toxic level in blood [254-256]. The ferromagnetic Fe which makes alloy with non-ferromagnetic material such Mn to form FeMn that were deposited through electrodeposition in AAO templates gives rise to a new technology. To fabricate align and uniform NWs in AAO templates, by using electrodeposition, have been used in many technological applications, such as the growth of vertical devices, with high aspect ratio. Up to present, very minor research has been done to study the structure and magnetic properties of FeMn alloys as a result to this, it is difficult to deposit Mn with Fe electrochemically [257, 258]. Hence, the work of this paper is first to synthesize FeMn alloy NWs in AAO templates through electrodeposition and second is to

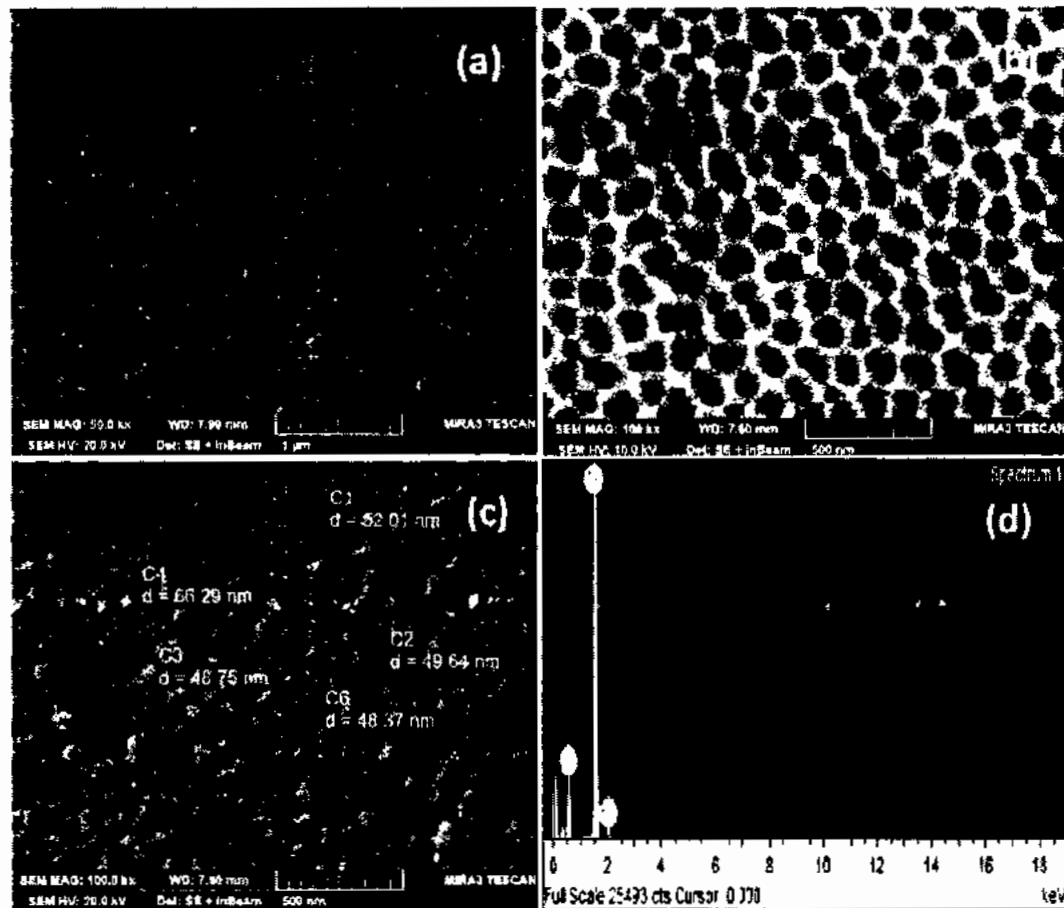


Figure 8. 1: (a, b & c) A typical top view SEM results and (d).show EDX result of AAO templates Prepared by 5%  $H_3PO_4$  with a high-density array of Nanopores

analyze their structural, magnetic and electrical properties in detail that will enhance the properties of spintronics devices in future prospectus.

## 8.2. Results and Discussions

The transit behavior of the current w.r.t time, during the first and second step of anodization, was explained in our previous work in detail [195]. Fig.8.1 (a-c) shows the top view of the AAO templates at a different resolution, which confirmed the regularity and homogeneous in a hexagonal shape. The average diameter and interpore distance were about 50nm and 125nm respectively. Whereas Fig.8.1d shows the EDX of the templates.

The SEM images were obtained at different resolution as shown in Fig.8.2 (a, b& c), and typical EDX spectra are presented to confirm the deposition of the required materials as shown in Fig.8.2d. Samples were characterized through SEM after the dissolution of the

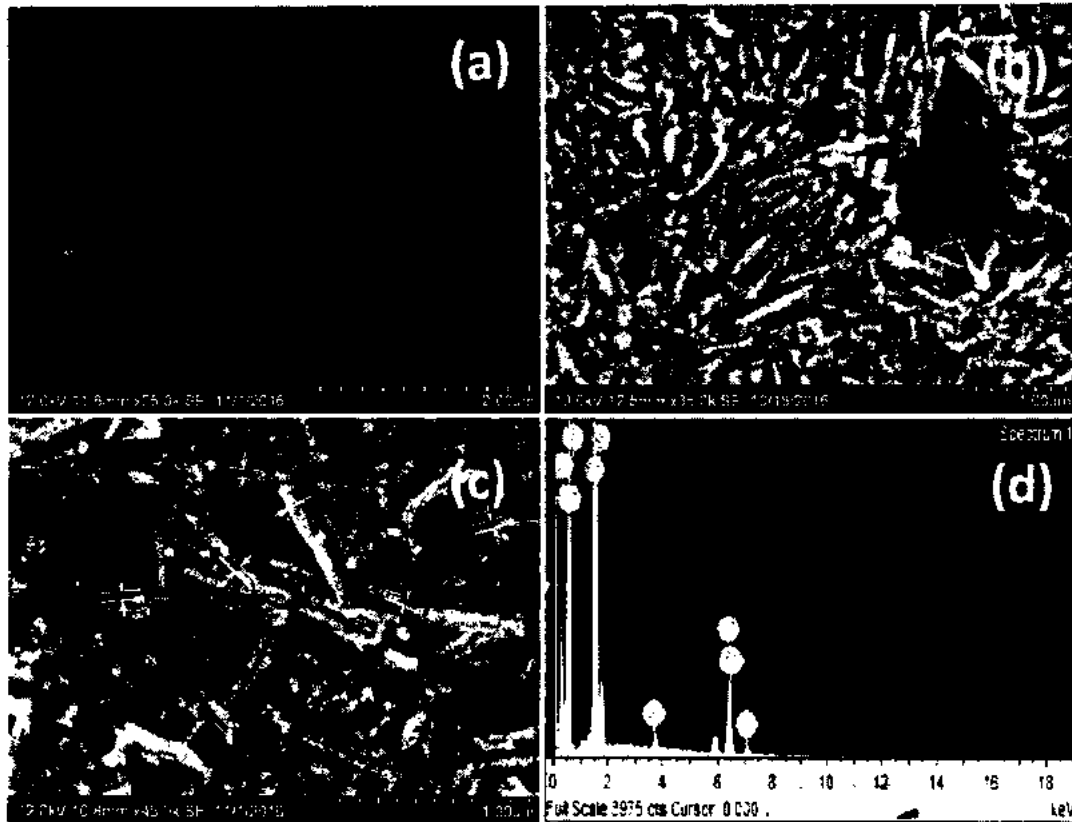


**Figure 8. 2:** (a, b &c) The SEM analysis and (d) EDX result of FeMn alloy NWs.

templates in 0.1M NaOH aqueous solution at 60 °C for 2 hrs. The average diameter of these NWs was about 50 nm.

Up to now, no specific method is discovered through which we can align these NWs after dissolving in NaOH solution. The compositional analysis of FeMn alloy NWs reveals that by increasing the concentration of Mn in the FeMn bath solution at constant electrodeposition voltage (15 V), that enhanced the concentration of Mn and decreased the Fe contents in the synthesis of FeMn alloy NWs as shown in Table.1. Which strongly affected on the structural, magnetic and electrical properties of FeMn alloy NWs.

The crystal structure of  $Fe_{1-x}Mn_x$  NWs were examined by obtaining X-rays diffraction (XRD) patterns without separating Al-substrate. Fig.8.3 shows the obtained diffraction patterns, which were analyzed by comparing with standard data [Fe (JCPDS# 96-411-3932), FeMn (JCPDS# 96-152-5356)]. The three diffraction peaks at  $2\theta \sim 44^\circ$ ,  $65^\circ$  and  $78^\circ$  were observed in all obtained diffraction patterns. The diffraction peak at  $\sim 78^\circ$  with (310) plane

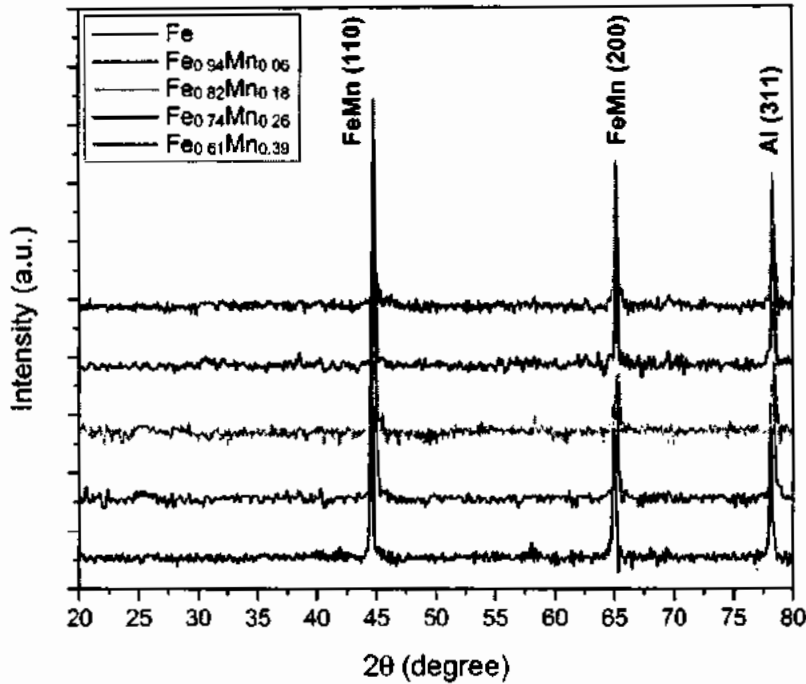


Figure 8. 3: XRD patterns of FeMn alloy NWs.

corresponds to reflection from the Al-substrate. In general, the penetration depth of X-ray increases at higher angle that is why reflection from Al-substrate appeared in the XRD patterns. The diffraction peaks at  $44^\circ$  and  $65^\circ$  with (110) and (200) planes, respectively, refers that the NWs were crystallized into body centered cubic structure. However, a shift in diffraction peaks was observed with increase of Mn content in NWs. The lattice parameter ( $a$ ) of NWs was also from (110) diffraction by applying following relation:

$$d = \frac{a}{\sqrt{h^2 + k^2 + l^2}} \quad 8.1$$

Where  $d$  is the interplaner spacing and  $h$ ,  $k$  and  $l$  are the miller indices of diffraction peaks.

The calculated lattice parameter values of NWs were listed in Table.8.1 that showed the lattice

**Table 8. 1:** Different calculated parameters of FeMn alloy NWs are obtained from XRD, VSM and EDX analysis. Here we represent the lattice parameter ( $a$ ), Grain size ( $D$ ) and lattice strain ( $\epsilon$ ), dislocation density ( $\delta$ ), coercivity ( $H_c$ ) and squareness ( $S^*$ ).

A	0.1M	-	100	0	Fe	2.872	38	236	6.9	324	0.22
B	0.1M	0.01M	94	6	Fe <sub>0.94</sub> Mn <sub>0.06</sub>	2.853	43	210	5.4	-	-
C	0.1M	0.02M	82	18	Fe <sub>0.82</sub> Mn <sub>0.18</sub>	2.851	46	186	4.7	252	0.23
D	0.1M	0.03M	74	26	Fe <sub>0.74</sub> Mn <sub>0.26</sub>	2.850	52	176	3.6	-	-
E	0.1M	0.04M	61	39	Fe <sub>0.61</sub> Mn <sub>0.39</sub>	2.847	53	173	3.5	230	0.25

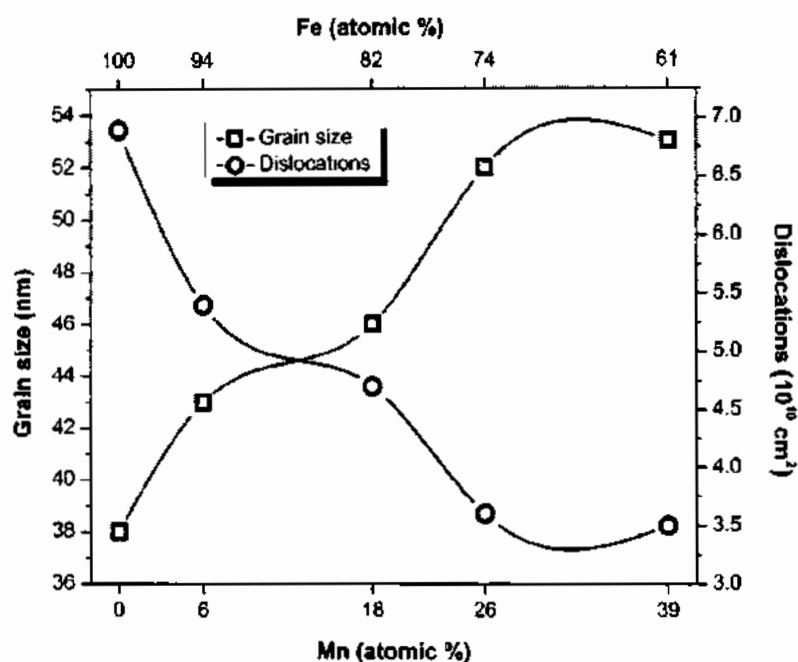


**Figure 8. 4:** The Grain size and Dislocations of FeMn NWs w.r.t atomic % of Fe and Mn.

parameter was decreased with increase of Mn content. Furthermore, Grain size ( $D$ ) and lattice strain ( $\epsilon$ ) of the NWs was also calculated from highly intense diffraction peak by applying Debye Scherrer equation and Stokes-Wilson Equation respectively, their values are listed in Table.8.1. An increasing trend in grain size was observed which indicates to the decrease of line dislocation density ( $\delta = \frac{1}{D^2}$ ) with increase of Mn content in NWs as shown in Fig.8.4. These analyses suggest that the grain boundaries was increased in NWs with the Mn substitution.

The electrical properties of  $\text{Fe}_{1-x}\text{Mn}_x$  alloy NWs were measured through four-probe (Hall technique) using “Swin Hall 8800, China”. Before to start the electrical characterization, first the samples were dipped in the 0.1M NaOH aqueous solution for 2 hrs at 60 °C, through which the templates (work as insulator) were removed from the upper part of NWs. So that no hurdle is expected during the characterization, while in the lower part remained there to support the NWs in the standing mode. As we deal with NWs instead of NW, because it is difficult to characterize a single NW. Therefore, the electrodes (four-probe Hall technique) are connected at the four corner of the sample (in square form) through silver paste.



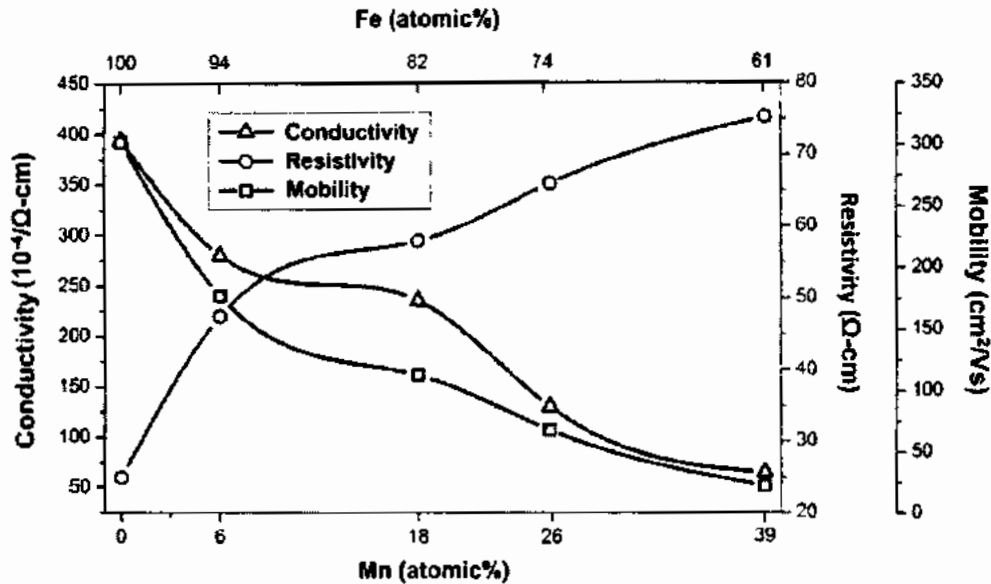


**Figure 8. 5:** Four probe (Hall measurement) analysis show the variation of mobility, Conductivity & resistivity w.r.t at% of Fe and Mn in FeMn alloys NWs.

$Fe_{1-x}Mn_x$  alloy NWs were characterized through four-probe (Hall measurement) technique as shown in Fig.8.5, which depend on Lorentz force. Fig.8.5 shows the variation of conductivity, resistivity and mobility w.r.t the variation of atomic percentage of Fe and Mn. Initially when pure Fe was deposited without Mn, then the grain size was absorbed up to 38nm. Which show high conductivity, mobility and display low resistivity. However, as the concentration of Mn is increased gradually (from 0.01 to 0.04M) in  $Fe_{1-x}Mn_x$  alloy NWs. Then the grain size was increased in a regular pattern, as shown in Fig.8.5. Also the resistivity was increased gradually (24 to 75.5  $\Omega\text{-cm}$ ) w.r.t increase in Mn concentration, while conductivity and mobility were shown opposite fashion to that of resistivity.

The magnetic properties of Fe,  $Fe_{0.82}Mn_{0.18}$  and  $Fe_{0.61}Mn_{0.39}$  NWs were examined by recording hysteresis loops at room temperature with applied magnetic field along the long axis of NWs. Fig.8.6 displays the recorded hysteresis loops and their corresponding parameter are listed in Table.8.1. It was observed that the coercivity ( $H_c$ ) and saturation magnetic moment was decreased with increase of Mn. Generally, the value of saturation magnetic moment depends on type of the materials and independent on its geometry, while  $H_c$  depends on geometry and exchange length of the materials, which is directly related with the reciprocal of the grain size in multi-magnetic domain material i.e.  $H_c \propto 1/D$ . Here, in present case, the  $H_c$  also showed inverse trend to grain size that confirms that the NWs consists on multi-magnetic domains.

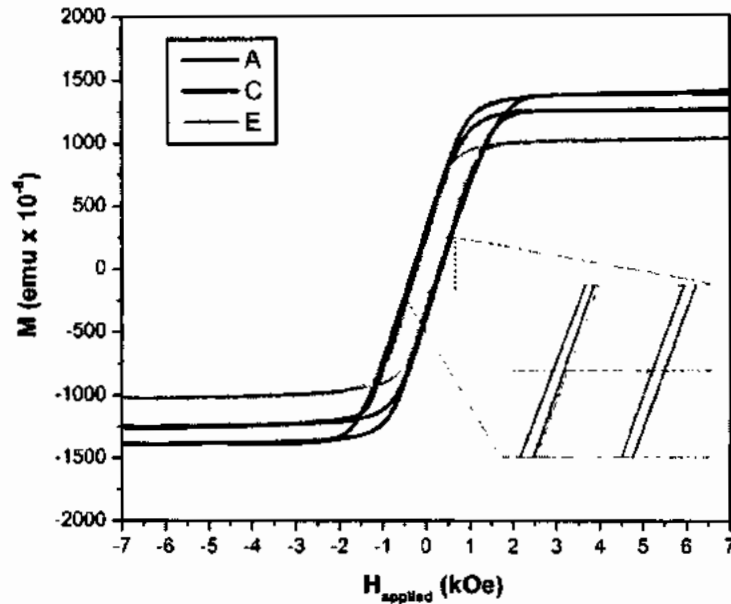


**Figure 8. 6:** Show the magnetic response of FeMn alloy NWs with the external magnetic field aligned parallel to the long axis.

Whereas, the squareness ( $S^*$ ), which is the ratio of remanence magnetic moment to saturation magnetic moment, of NWs' was increased with increase of Mn content in FeMn NWs. This increase in  $S^*$  reveals that uniaxial magnetic anisotropy of NW was improved. In principle, the overall magnetic anisotropy in NW arrays depend upon shape anisotropy, magnetocrystalline anisotropy and magnetostatic interaction between NWs. Among these anisotropy factors, shape anisotropy and magnetostatic interaction between NWs only depend on geometry and directly proportional to saturation magnetization of the NWs. Here, the increase in magnetic anisotropy, without any change in geometry and decrease of saturation magnetic moment, suggests that increase in magnetocrystalline anisotropy is the possible reason behind increase of magnetic anisotropy.

---

---

## Conclusion

The fundamental and principal objectives of this thesis was synthesise of aligned, homogenous and the periodic form of self-assemble anodized aluminum oxide (AAO) templates by two-step of anodization. The choice of self-assembled anodic alumina is to fabricate the nanowires (NWs) in the desired length and diameter. Such parameters strongly affect their magnetic, electric and structural properties of the synthesized NWs. The properties of the NWs that has high aspect ratio relative to the bulk counterpart also processes the shape anisotropy and transfer the additional charge (spin-dependent) in traditional electronic devices to enhance the function of spintronics devices, such as MR, GMR, TMR. To achieve such objective, four different series of the NWs have been synthesized; two series of the full Heusler alloys NWs (Co-based  $\text{Co}_2\text{Mn}_{0.5}\text{Fe}_{0.5}\text{Sn}$  and Fe-based  $\text{Fe}_2\text{CoSn}$ ) and two series of the binary alloys NWs ( $\text{Fe}_{100-x}\text{Cu}_x$  and  $\text{Fe}_{1-x}\text{Mn}_x$ ). Hence the quaternary full Heusler alloys NWs with a stable phase indicated by  $L2_1$ , through the chemical formula  $X_2YZ$  (2:1:1) and binary alloys were synthesized through AC-electrochemical deposition in self-assembled AAO templates through the pore diameter lie in the range of 55-65 nm. Such Heusler series can be predicted as half-metallic ferromagnetism with 100% spin polarization. Therefore such character NWs, the Co-based  $\text{Co}_2\text{Mn}_{0.5}\text{Fe}_{0.5}\text{Sn}$  full Heusler alloy and Fe-based  $\text{Fe}_2\text{CoSn}$  full Heusler alloys NWs were selected for such research, which has not been synthesized experimentally earlier before in the form of NWs. Hence the synthesized NWs of four different series have been characterized through various physical properties; morphology, electric, magnetic, structural and transport properties and the origin of band gap at Fermi level shows spin polarization 100 % (half-metallicity), has been confirmed through density functional theory (DFT) by using WIEN2k programs of full potential linearized augmented plane wave (FP-LAPW) technique.

Keeping in view the Co-based  $\text{Co}_2\text{Mn}_{0.5}\text{Fe}_{0.5}\text{Sn}$  full Heusler alloy NWs has been selected to synthesise their full order and stable ( $L2_1$ ) structure by changing 2V from 10 to 18V through AC- deposition potential in AAO templates that tune their various physical properties. The AAO templates were synthesized in 5% phosphoric acid with 60V (constant DC source) by two-steps of anodization at the range of temperature 1 to 5  $^{\circ}\text{C}$ . The morphology of the synthesized NWs of all series have laid in the range of 55 to 65nm that has confirmed from scanning electron microscope (SEM) images. The EDX confirmed the deposition of all desire materials and display that each element has different reduction potential. The structure analysis

---

---

through XRD at 10V, 12V and 14V are attributed to only fundamental reflection peaks that display B2-type A2-type called partially disorder and full disorder structure analysis respectively. But at 16V and 18V, the reflection of fundamental along with odd superlattice and even superlattice have been observed that confirmed the formation of full order  $L2_1$  structure of full Heusler  $\text{Co}_2\text{Mn}_{0.5}\text{Fe}_{0.5}\text{Sn}$  alloy NWs. The electrical measurement with four probe hall technique was done without anodic alumina shows the decrement in resistivity from 160 to 40  $\Omega\text{-cm}$  relative to the increment of the deposition potential to confirm the metallicity of our sample. At 18V only full order  $L2_1$  structure has been synthesized without any other phase like Sn, that enhance coercivity sharply from 65 to 245Oe. The half-metallicity (100% spin polarization) due to the origin of band gap at Fermi level is confirmed through DFT measurement by WIEN2k programs of full potential linearized augmented plane wave (FP-LAPW) technique.

Now the spin-dependent properties as half-metallic ferromagnetism is achieved in a more appropriate format by selecting the Fe-based  $\text{Fe}_2\text{CoSn}$  full Heusler alloy. The results from such Heusler alloy has been achieved to synthesize  $\text{Fe}_2\text{CoSn}$  full Heusler alloy NWs. To attain the desired results, 9 to 17V AC-electrodeposition by the difference of 2V has been taken in the same morphological AAO templates. From EDX, it is confirmed that the required ratio of full Heusler alloy 2:1:1 combination has been successfully attained at the deposition voltage of 15 and 17. The full order desired structure  $L2_1$  of  $\text{Fe}_2\text{CoSn}$  Heusler alloy NWs has been obtained at same voltages that contain all fundamental reflection, odd and even superlattice. Whereas A2 and B2-type disorder structure have been observed at 9 to 13V. The increase in intensity and variation of shift w.r.t increase in deposition voltage shows the enhancement of the grain size and decrease of stress (increase in lattice parameter) respectively. From M-H loop, it is clear that coercivity attained sharply to its maximum value (484 Oe) among all samples when deposited at the 17V show the effect of  $L2_1$  structure on its magnetic properties of Heusler alloy NWs. From two probes (I-V) technique, such Heusler alloy NWs illustrate the non-ohmic character and show maximum mobility with the formation of  $L2_1$  order structure. The DFT calculation by WIEN2k program to investigate the half-metallicity in  $\text{Fe}_2\text{CoSn}$  Heusler alloy NWs. Few states of Fe-3d at Fermi level show through the partial density of states (PDOS) contribute very less in conduction compared to minority channel. It also obeys

---

---

Slater-Pauling rule, in which magnetic moment of total spin that proportional linearly to the valance shell electrons in the unit cell of  $\text{Fe}_2\text{CoSn}$  Haussler alloy NWs.

The spin-dependent devices are linearly proportional to the structural and compositional constraints. The advantage of the alloy (Ferro-nonferro) NWs over single elemental (ferromagnetism) NWs can be used to tune the magnetic and transport parameters through morphology and composition ratio. Therefore  $\text{Fe}_{100-x}\text{Cu}_x$  alloy NWs has been fabricated in anodic alumina through the same approach and parameters, only 16V deposition potential remain constant by the variation concentration of FeCu in the electrolyte. First, only Fe-*bcc* peaks are observed in XRD pattern, because of it deposited without Cu contents. Hence Cu contents is progressively added in the Fe-electrolyte solution, which completely suppresses the Fe-*bcc* peaks and has produced the FeCu *bcc* peak along with separate Cu-*fcc* reflection planes also observed. From XRD analysis, the lattice parameter has increased that affects to decrease the lattice strain. Therefore shift was produced towards lower angle. The coercivity show decreasing pattern because of enhancement in the grain size. And the magnetic moment alignments of Fe was suppressed because of the atomic radius of Cu is greater than that of Fe.

The last binary alloy is ferromagnetic material coupling with non-ferromagnetic to synthesize the  $\text{Fe}_{1-x}\text{Mn}_x$  alloy NWs. The Fe-Mn is a biologically (biodegradable) alloying element, as a high ratio of Mn is observed to be not toxic. Keeping in view the last step of this research was to synthesize the FeMn alloy NWs in AAO templates by the same technique AC-electrodeposition at room temperature. The analysis of X-ray diffraction (XRD) pattern shows that the aluminum peak are observed because of such NWs are characterized with the substrate. The XRD patterns exhibited the FeMn NWs were crystallized into body centered cubic (*bcc*) structure. Furthermore, the lattice parameter of FeMn NWs was decreased with addition of Mn content. The grain size shows the increasing order (from 38 to 53nm) w.r.t to increase the concentration of Mn in  $\text{Fe}_{1-x}\text{Mn}_x$  bath solution, that effect to decrease the coercivity. The shape anisotropy is dominated in FeMn alloy NWs. Therefore, it has been attributed the motion of domain walls due to the decrease the magnetic grain boundaries. The four-probe (Hall measurement) technique shows the resistivity has decreased slowly (24 to 75.5  $\Omega\cdot\text{cm}$ ) opposite to that of conductivity by the increment of Mn contents in  $\text{Fe}_{1-x}\text{Mn}_x$  alloy NWs.

---

---

**References**

- [1] R.P. Feynman, There's Plenty of Room at the Bottom, SPIE MILESTONE SERIES MS 182 (2006) 3.
- [2] G. Binnig, H. Rohrer, Scanning tunneling microscopy, IBM Journal of research and development 44(1/2) (2000) 279.
- [3] C. Knoedler, Helium- ion damage and nanowire fabrication in GaAs/AlGaAs heterostructures, Journal of applied physics 68(3) (1990) 1129-1137.
- [4] S. Iijima, T. Ichihashi, Single-shell carbon nanotubes of 1-nm diameter, nature 363(6430) (1993) 603.
- [5] D. Bethune, C.H. Kiang, M. De Vries, G. Gorman, R. Savoy, J. Vazquez, R. Beyers, Cobalt-catalysed growth of carbon nanotubes with single-atomic-layer walls, Nature 363(6430) (1993) 605-607.
- [6] G.E.J. Poinern, N. Ali, D. Fawcett, Progress in nano-engineered anodic aluminum oxide membrane development, Materials 4(3) (2011) 487-526.
- [7] J.W. Diggle, T.C. Downie, C. Goulding, Anodic oxide films on aluminum, Chemical Reviews 69(3) (1969) 365-405.
- [8] M. Lohregel, Thin anodic oxide layers on aluminium and other valve metals: high field regime, Materials Science and Engineering: R: Reports 11(6) (1993) 243-294.
- [9] E. Palibroda, A. Lupsan, S. Pruneanu, M. Savos, Aluminium porous oxide growth. On the electric conductivity of the barrier layer, Thin Solid Films 256(1-2) (1995) 101-105.
- [10] Y.-S. Kim, S.-I. Pyun, S.-M. Moon, J.-D. Kim, The effects of applied potential and pH on the electrochemical dissolution of barrier layer in porous anodic oxide film on pure aluminium, Corrosion science 38(2) (1996) 329-336.
- [11] F. Li, L. Zhang, R.M. Metzger, On the growth of highly ordered pores in anodized aluminum oxide, Chemistry of materials 10(9) (1998) 2470-2480.
- [12] H. Masuda, K. Fukuda, Ordered metal nanohole arrays made by a two-step replication of honeycomb structures of anodic alumina, science 268(5216) (1995) 1466-1468.
- [13] H. Masuda, H. Yamada, M. Satoh, H. Asoh, M. Nakao, T. Tamamura, Highly ordered nanochannel-array architecture in anodic alumina, Applied Physics Letters 71(19) (1997) 2770-2772.

- [14] T.T. Xu, R.D. Piner, R.S. Ruoff, An improved method to strip aluminum from porous anodic alumina films, *Langmuir* 19(4) (2003) 1443-1445.
- [15] Y. Zhao, M. Chen, Y. Zhang, T. Xu, W. Liu, A facile approach to formation of through-hole porous anodic aluminum oxide film, *Materials Letters* 59(1) (2005) 40-43.
- [16] T. Xu, G. Zangari, R.M. Metzger, Periodic holes with 10 nm diameter produced by grazing Ar<sup>+</sup> milling of the barrier layer in hexagonally ordered nanoporous alumina, *Nano Letters* 2(1) (2002) 37-41.
- [17] M. Lillo, D. Losic, Ion-beam pore opening of porous anodic alumina: the formation of single nanopore and nanopore arrays, *Materials letters* 63(3-4) (2009) 457-460.
- [18] J. O'sullivan, G. Wood, The morphology and mechanism of formation of porous anodic films on aluminium, *Proceedings of the Royal Society of London. A. Mathematical and Physical Sciences* 317(1531) (1970) 511-543.
- [19] C.R. Martin, Template synthesis of electronically conductive polymer nanostructures, *Accounts of chemical research* 28(2) (1995) 61-68.
- [20] C.R. Martin, Membrane-based synthesis of nanomaterials, *Chemistry of Materials* 8(8) (1996) 1739-1746.
- [21] H. Asoh, M. Matsuo, M. Yoshihama, S. Ono, Transfer of nanoporous pattern of anodic porous alumina into Si substrate, *Applied physics letters* 83(21) (2003) 4408-4410.
- [22] S. Ono, A. Oide, H. Asoh, Nanopatterning of silicon with use of self-organized porous alumina and colloidal crystals as mask, *Electrochimica acta* 52(8) (2007) 2898-2904.
- [23] S. Shingubara, Y. Murakami, K. Morimoto, T. Takahagi, Formation of aluminum nanodot array by combination of nanoindentation and anodic oxidation of aluminum, *Surface Science* 532 (2003) 317-323.
- [24] G. Cao, D. Liu, Template-based synthesis of nanorod, nanowire, and nanotube arrays, *Advances in colloid and interface science* 136(1-2) (2008) 45-64.
- [25] A. Yamaguchi, K. Hotta, N. Teramae, Optical waveguide sensor based on a porous anodic alumina/aluminum multilayer film, *Analytical chemistry* 81(1) (2008) 105-111.
- [26] F. Trivinho-Strixino, H. Guerreiro, C. Gomes, E. Pereira, F.E.G. Guimarães, Active waveguide effects from porous anodic alumina: An optical sensor proposition, *Applied Physics Letters* 97(1) (2010) 011902.

- [27] R.O. Al-Kaysi, T.H. Ghaddar, G. Guirado, Fabrication of one-dimensional organic nanostructures using anodic aluminum oxide templates, *Journal of Nanomaterials* 2009 (2009) 7.
- [28] H.-B. Xu, H.-Z. Chen, W.-J. Xu, M. Wang, Fabrication of organic copper phthalocyanine nanowire arrays via a simple AAO template-based electrophoretic deposition, *Chemical physics letters* 412(4-6) (2005) 294-298.
- [29] R. Bai, M. Shi, M. Ouyang, Y. Cheng, H. Zhou, L. Yang, M. Wang, H. Chen, Erbium bisphthalocyanine nanowires by electrophoretic deposition: Morphology control and optical properties, *Thin Solid Films* 517(6) (2009) 2099-2105.
- [30] M. Steinhart, R.B. Wehrspohn, U. Gösele, J.H. Wendorff, Nanotubes by template wetting: a modular assembly system, *Angewandte Chemie International Edition* 43(11) (2004) 1334-1344.
- [31] L. Zhao, W. Yang, Y. Ma, J. Yao, Y. Li, H. Liu, Perylene nanotubes fabricated by the template method, *Chemical Communications* (19) (2003) 2442-2443.
- [32] M. Steinhart, J. Wendorff, A. Greiner, R. Wehrspohn, K. Nielsch, J. Schilling, J. Choi, U. Gösele, Polymer nanotubes by wetting of ordered porous templates, *Science* 296(5575) (2002) 1997-1997.
- [33] X.-P. Shen, G. Yin, C. Gao, Z. Xu, Construction and fluorescence of organic nanotube arrays by template-based physical vapor deposition method, *Materials Chemistry and Physics* 113(1) (2009) 202-207.
- [34] G. Kartopu, M. Es-Souni, A. Sapelkin, D. Dunstan, Large-scale, reliable and robust SERS-active nanowire substrates prepared using porous alumina templates, *Journal of nanoscience and nanotechnology* 8(2) (2008) 931-935.
- [35] A. Vaseashta, D. Dimova-Malinovska, Nanostructured and nanoscale devices, sensors and detectors, *Science and Technology of Advanced Materials* 6(3-4) (2005) 312-318.
- [36] P.M. Petroff, A. Lorke, A. Imamoglu, Epitaxially self-assembled quantum dots, *Physics Today* 54(5) (2001) 46-52.
- [37] T. Islam, K.K. Mistry, K. Sengupta, H. Saha, Measurement of gas moisture in the ppm range using porous silicon and porous alumina sensors, *Sensors and Materials* 16(7) (2004) 345-356.



- [38] D. Routkevitch, A. Tager, J. Haruyama, D. Almawlawi, M. Moskovits, J.M. Xu, Nonlithographic nano-wire arrays: fabrication, physics, and device applications, *IEEE transactions on electron devices* 43(10) (1996) 1646-1658.
- [39] P.J. Dobson, *Nanomedicine: Design and Applications of Magnetic Nanomaterials, Nanosensors and Nanosystems*, by Vijay K. Varadan, Linfeng Chen and Jining Xie: Scope: monograph, reference. Level: postgraduate, advanced undergraduate, early career researcher, researcher, engineers, Taylor & Francis, 2012.
- [40] S.M. Thompson, The discovery, development and future of GMR: The Nobel Prize 2007, *Journal of Physics D: Applied Physics* 41(9) (2008) 093001.
- [41] S.S. Parkin, M. Hayashi, L. Thomas, Magnetic domain-wall racetrack memory, *Science* 320(5873) (2008) 190-194.
- [42] R. De Groot, F. Mueller, P. Van Engen, K. Buschow, New class of materials: half-metallic ferromagnets, *Physical Review Letters* 50(25) (1983) 2024.
- [43] G. Schmidt, D. Ferrand, L. Molenkamp, A. Filip, B. Van Wees, Fundamental obstacle for electrical spin injection from a ferromagnetic metal into a diffusive semiconductor, *Physical Review B* 62(8) (2000) R4790.
- [44] P.-C. Hsu, S. Wang, H. Wu, V.K. Narasimhan, D. Kong, H.R. Lee, Y. Cui, Performance enhancement of metal nanowire transparent conducting electrodes by mesoscale metal wires, *Nature communications* 4 (2013) 2522.
- [45] L. Chen, W. Lu, C.M. Lieber, Semiconductor nanowire growth and integration, *Semiconductor Nanowires* (11) (2014) 1.
- [46] D. Han, X. Zhang, Z. Wu, Z. Hua, Z. Wang, S. Yang, Synthesis and magnetic properties of complex oxides  $\text{La}_{0.67}\text{Sr}_{0.33}\text{MnO}_3$  nanowire arrays, *Ceramics International* 42(15) (2016) 16992-16996.
- [47] Z.R. Dai, Z.W. Pan, Z.L. Wang, Novel nanostructures of functional oxides synthesized by thermal evaporation, *Advanced Functional Materials* 13(1) (2003) 9-24.
- [48] A. Fernández-Pacheco, L. Serrano-Ramón, J.M. Michalik, M.R. Ibarra, J.M. De Teresa, L. O'brien, D. Petit, J. Lee, R.P. Cowburn, Three dimensional magnetic nanowires grown by focused electron-beam induced deposition, *Scientific reports* 3 (2013) 1492.
- [49] D. Zagorskiy, V. Korotkov, K. Frolov, S. Sulyanov, V. Kudryavtsev, S. Kruglikov, S. Bedin, Track pore matrixes for the preparation of Co, Ni and Fe nanowires: Electrodeposition and their properties, *Physics Procedia* 80 (2015) 144-147.

- [50] M.J. Treacy, T. Ebbesen, J. Gibson, Exceptionally high Young's modulus observed for individual carbon nanotubes, *Nature* 381(6584) (1996) 678.
- [51] L. O'Brien, D. Petit, E. Lewis, R. Cowburn, D. Read, J. Sampaio, H. Zeng, A.-V. Jausovec, Tunable remote pinning of domain walls in magnetic nanowires, *Physical review letters* 106(8) (2011) 087204.
- [52] J.-V. Kim, Spin-torque oscillators, *Solid State Physics*, Elsevier 2012, pp. 217-294.
- [53] A. Fert, L. Piraux, Magnetic nanowires, *Journal of Magnetism and Magnetic Materials* 200(1-3) (1999) 338-358.
- [54] H. Forster, T. Schrefl, D. Suess, W. Scholz, V. Tsiantos, R. Dittrich, J. Fidler, Domain wall motion in nanowires using moving grids, *Journal of applied physics* 91(10) (2002) 6914-6919.
- [55] J.-M. Hu, T. Yang, K. Momeni, X. Cheng, L. Chen, S. Lei, S. Zhang, S. Trolrier-McKinstry, V. Gopalan, G.P. Carman, Fast magnetic domain-wall motion in a ring-shaped nanowire driven by a voltage, *Nano letters* 16(4) (2016) 2341-2348.
- [56] A. Fert, Nobel lecture: Origin, development, and future of spintronics, *Reviews of Modern Physics* 80(4) (2008) 1517.
- [57] I. Minguez-Bacho, S. Rodriguez-López, M. Vázquez, M. Hernández-Vélez, K. Nielsch, Electrochemical synthesis and magnetic characterization of periodically modulated Co nanowires, *Nanotechnology* 25(14) (2014) 145301.
- [58] N. Lei, T. Devolder, G. Agnus, P. Aubert, L. Daniel, J.-V. Kim, W. Zhao, T. Trypiniotis, R.P. Cowburn, C. Chappert, Strain-controlled magnetic domain wall propagation in hybrid piezoelectric/ferromagnetic structures, *Nature communications* 4 (2013) 1378.
- [59] T. Graf, C. Felser, S.S. Parkin, Simple rules for the understanding of Heusler compounds, *Progress in solid state chemistry* 39(1) (2011) 1-50.
- [60] H. Potter, The X-ray structure and magnetic properties of single crystals of Heusler alloy, *Proceedings of the Physical Society* 41(1) (1928) 135.
- [61] P. Webster, Magnetic and chemical order in Heusler alloys containing cobalt and manganese, *Journal of Physics and Chemistry of Solids* 32(6) (1971) 1221-1231.
- [62] J. Kübler, A. William, C. Sommers, Formation and coupling of magnetic moments in Heusler alloys, *Physical Review B* 28(4) (1983) 1745.
- [63] I. Galanakis, P. Dederichs, N. Papanikolaou, Slater-Pauling behavior and origin of the half-metallicity of the full-Heusler alloys, *Physical Review B* 66(17) (2002) 174429.

- [64] X.-Q. Chen, R. Podloucky, P. Rogl, Ab initio prediction of half-metallic properties for the ferromagnetic Heusler alloys  $\text{Co}_2\text{M}\text{Si}$  ( $\text{M} = \text{Ti}, \text{V}, \text{Cr}$ ), *Journal of applied physics* 100(11) (2006) 113901.
- [65] H.C. Kandpal, G.H. Fecher, C. Felser, Calculated electronic and magnetic properties of the half-metallic, transition metal based Heusler compounds, *Journal of Physics D: Applied Physics* 40(6) (2007) 1507.
- [66] A. Rajanikanth, D. Kande, Y. Takahashi, K. Hono, High spin polarization in a two phase quaternary Heusler alloy  $\text{Co}_2\text{MnAl}_{1-x}\text{Sn}_x$ , *Journal of applied physics* 101(9) (2007) 09J508.
- [67] M. Yamamoto, T. Ishikawa, T. Taira, G.-f. Li, K.-i. Matsuda, T. Uemura, Effect of defects in Heusler alloy thin films on spin-dependent tunnelling characteristics of  $\text{Co}_2\text{MnSi}/\text{MgO}/\text{Co}_2\text{MnSi}$  and  $\text{Co}_2\text{MnGe}/\text{MgO}/\text{Co}_2\text{MnGe}$  magnetic tunnel junctions, *Journal of Physics: Condensed Matter* 22(16) (2010) 164212.
- [68] T. Graf, F. Casper, J. Winterlik, B. Balke, G.H. Fecher, C. Felser, Crystal structure of new Heusler compounds, *Zeitschrift für anorganische und allgemeine Chemie* 635(6-7) (2009) 976-981.
- [69] S. Picozzi, A. Cozzinzenza, A.J. Freeman, Role of structural defects on the half-metallic character of  $\text{Co}_2\text{MnGe}$  and  $\text{Co}_2\text{MnSi}$  Heusler alloys, *Physical Review B* 69(9) (2004) 094423.
- [70] R. Zhang, *Magnetic Interactions in Low-Dimensional Iron Nanostructures*, (2013).
- [71] J.C. Slater, The ferromagnetism of nickel. II. Temperature effects, *Physical Review* 49(12) (1936) 931.
- [72] L. Pauling, The nature of the interatomic forces in metals, *Physical Review* 54(11) (1938) 899.
- [73] M. Darques, A.-S. Bogaert, F. Elhoussine, S. Michotte, J. de la Torre Medina, A. Encinas, L. Piraux, Controlled growth of  $\text{CoCu}$  nanowires and application to multilayered  $\text{CoCu}/\text{Cu}$  nanowires with selected anisotropy, *Journal of Physics D: Applied Physics* 39(23) (2006) 5025.
- [74] R.O. Jones, Density functional theory: Its origins, rise to prominence, and future, *Reviews of modern physics* 87(3) (2015) 897.
- [75] M.-Q. Long, L. Tang, D. Wang, L. Wang, Z. Shuai, Theoretical predictions of size-dependent carrier mobility and polarity in graphene, *Journal of the American Chemical Society* 131(49) (2009) 17728-17729.

- [76] J. Camargo-Martinez, R. Baquero, The band gap problem: the accuracy of the Wien2k code confronted, *Revista mexicana de fisica* 59(5) (2013) 453-459.
- [77] R. Koehler Jr, R. Feigelson, H. Swarts, R. White, Effects of Stoichiometry and Impurities on the Metal- to- Semimetal Transition in NiS, *Journal of Applied Physics* 43(7) (1972) 3127-3131.
- [78] S. Blugel, G. Bihlmayer, Full-potential linearized augmented planewave method, (2006).
- [79] G.D. Sulka, Highly ordered anodic porous alumina formation by self-organized anodizing, *Nanostructured materials in electrochemistry* 1 (2008) 1-116.
- [80] H. Masuda, M. Satoh, Fabrication of gold nanodot array using anodic porous alumina as an evaporation mask, *Japanese Journal of Applied Physics* 35(1B) (1996) L126.
- [81] G. Schwartz, V. Platter, An anodic process for forming planar interconnection metallization for multilevel LSI, *Journal of the Electrochemical Society* 122(11) (1975) 1508-1516.
- [82] F.C. Schaedel, Aluminum anodizing method, Google Patents, 1968.
- [83] G. Sulka, S. Stroobants, V. Moshchalkov, G. Borghs, J.-P. Celis, Synthesis of well-ordered nanopores by anodizing aluminum foils in sulfuric acid, *Journal of the Electrochemical Society* 149(7) (2002) D97-D103.
- [84] K. Shimizu, G. Brown, H. Habazaki, K. Kobayashi, P. Skeldon, G. Thompson, G. Wood, Influence of surface roughness on the depth resolution of GDOES depth profiling analysis, *Surface and Interface Analysis: An International Journal devoted to the development and application of techniques for the analysis of surfaces, interfaces and thin films* 27(3) (1999) 153-156.
- [85] V. Parkhutik, J. Albella, Y.E. Makushok, I. Montero, J. Martinez-Duart, V. Shershulskii, Study of aluminium anodization in sulphuric and chromic acid solutions—I. Kinetics of growth and composition of oxides, *Electrochimica Acta* 35(6) (1990) 955-960.
- [86] M. Nagayama, K. Tamura, Dissolution of the anodic oxide film on aluminium in a sulphuric acid solution, *Electrochimica Acta* 12(8) (1967) 1097-1107.
- [87] C. Brändli, T.F. Jaramillo, A. Ivanovskaya, E.W. McFarland, Automated synthesis and characterization of diverse libraries of macroporous alumina, *Electrochimica Acta* 47(4) (2001) 553-557.

- [88] G. Thompson, Y. Xu, P. Skeldon, K. Shimizu, S. Han, G. Wood, Anodic oxidation of aluminium, *Philosophical Magazine B* 55(6) (1987) 651-667.
- [89] I. Vrublevsky, V. Parkoun, J. Schreckenbach, W.A. Goedel, Dissolution behaviour of the barrier layer of porous oxide films on aluminum formed in phosphoric acid studied by a re-anodizing technique, *Applied surface science* 252(14) (2006) 5100-5108.
- [90] S. Ono, H. Ichinose, N. Masuko, The high resolution observation of porous anodic films formed on aluminum in phosphoric acid solution, *Corrosion science* 33(6) (1992) 841-850.
- [91] R.B. Mason, Factors affecting the formation of anodic oxide coatings in sulfuric acid electrolytes, *Journal of The Electrochemical Society* 102(12) (1955) 671-675.
- [92] G. Wood, P. Skeldon, G. Thompson, K. Shimizu, A model for the incorporation of electrolyte species into anodic alumina, *Journal of the Electrochemical Society* 143(1) (1996) 74-83.
- [93] H. Han, S.-J. Park, J.S. Jang, H. Ryu, K.J. Kim, S. Baik, W. Lee, In situ determination of the pore opening point during wet-chemical etching of the barrier layer of porous anodic aluminum oxide: nonuniform impurity distribution in anodic oxide, *ACS applied materials & interfaces* 5(8) (2013) 3441-3448.
- [94] S.K. Thamida, H.-C. Chang, Nanoscale pore formation dynamics during aluminum anodization, *Chaos: An Interdisciplinary Journal of Nonlinear Science* 12(1) (2002) 240-251.
- [95] A. Li, F. Müller, A. Birner, K. Nielsch, U. Gösele, Hexagonal pore arrays with a 50–420 nm interpore distance formed by self-organization in anodic alumina, *Journal of applied physics* 84(11) (1998) 6023-6026.
- [96] L. Zhang, H. Cho, F. Li, R. Metzger, W. Doyle, Cellular growth of highly ordered porous anodic films on aluminium, *Journal of materials science letters* 17(4) (1998) 291-294.
- [97] K. Nielsch, J. Choi, K. Schwirn, R.B. Wehrspohn, U. Gösele, Self-ordering regimes of porous alumina: the 10 porosity rule, *Nano letters* 2(7) (2002) 677-680.
- [98] H. Masuda, K. Yada, A. Osaka, Self-ordering of cell configuration of anodic porous alumina with large-size pores in phosphoric acid solution, *Japanese Journal of Applied Physics* 37(11A) (1998) L1340.
- [99] G. Patermarakis, C. Pavlidou, Catalysis over porous anodic alumina catalysts, *Journal of catalysis* 147(1) (1994) 140-155.

- [100] G. Patermarakis, K. Moussoutzanis, N. Nikolopoulos, Investigation of the incorporation of electrolyte anions in porous anodic Al<sub>2</sub>O<sub>3</sub> films by employing a suitable probe catalytic reaction, *Journal of solid state electrochemistry* 3(4) (1999) 193-204.
- [101] G. Patermarakis, J. Chandrinos, K. Moussoutzanis, Interface physicochemical processes controlling sulphate anion incorporation in porous anodic alumina and their dependence on the thermodynamic and transport properties of cations, *Journal of Electroanalytical Chemistry* 510(1-2) (2001) 59-66.
- [102] G. Patermarakis, P. Lenas, C. Karavassilis, G. Papayiannis, Kinetics of growth of porous anodic Al<sub>2</sub>O<sub>3</sub> films on Al metal, *Electrochimica acta* 36(3-4) (1991) 709-725.
- [103] G. Patermarakis, Transformation of the overall strict kinetic model governing the growth of porous anodic Al<sub>2</sub>O<sub>3</sub> films on aluminium to a form applicable to the non-stirred bath film growth. *Electrochimica acta* 41(16) (1996) 2601-2611.
- [104] G. Patermarakis, K. Moussoutzanis, Mathematical Models for the Anodization Conditions and Structural Features of Porous Anodic Al<sub>2</sub>O<sub>3</sub> Films on Aluminum, *Journal of the Electrochemical Society* 142(3) (1995) 737-743.
- [105] G. Patermarakis, Development of a theory for the determination of the composition of the anodizing solution inside the pores during the growth of porous anodic Al<sub>2</sub>O<sub>3</sub> films on aluminium by a transport phenomenon analysis, *Journal of Electroanalytical Chemistry* 447(1-2) (1998) 25-41.
- [106] G. Patermarakis, K. Moussoutzanis, Formulation of a criterion predicting the development of uniform regular and non-uniform abnormal porous anodic alumina coatings and revealing the mechanisms of their appearance and progress, *Corrosion science* 43(8) (2001) 1433-1464.
- [107] G. Patermarakis, K. Moussoutzanis, Electrochemical kinetic study on the growth of porous anodic oxide films on aluminium, *Electrochimica acta* 40(6) (1995) 699-708.
- [108] G. Patermarakis, K. Moussoutzanis, J. Chandrinos, Discovery by kinetic studies of the latent physicochemical processes and their mechanisms during the growth of porous anodic alumina films in sulfate electrolytes, *Journal of Solid State Electrochemistry* 6(1) (2001) 39-54.
- [109] D.D. Macdonald, The point defect model for the passive state, *Journal of the Electrochemical Society* 139(12) (1992) 3434-3449.

- [110] D.D. Macdonald, S.R. Biaggio, H. Song, Steady- State Passive Films Interfacial Kinetic Effects and Diagnostic Criteria, *Journal of the Electrochemical Society* 139(1) (1992) 170-177.
- [111] D.D. Macdonald, On the formation of voids in anodic oxide films on aluminum, *Journal of the Electrochemical Society* 140(3) (1993) L27-L30.
- [112] S.-K. Hwang, S.-H. Jeong, H.-Y. Hwang, O.-J. Lee, K.-H. Lee, Fabrication of highly ordered pore array in anodic aluminum oxide, *Korean Journal of Chemical Engineering* 19(3) (2002) 467-473.
- [113] G. Sulka, K. Parkoła, Temperature influence on well-ordered nanopore structures grown by anodization of aluminium in sulphuric acid, *Electrochimica Acta* 52(5) (2007) 1880-1888.
- [114] F. Heusler, F. Heusler, *Verh. Dtsch. Phys. Ges.* 5, 219 (1903), *Verh. Dtsch. Phys. Ges.* 5 (1903) 219.
- [115] C. Felser, G.H. Fecher, B. Balke, Spintronics: a challenge for materials science and solid- state chemistry, *Angewandte Chemie International Edition* 46(5) (2007) 668-699.
- [116] S. Wurmehl, H.C. Kandpal, G.H. Fecher, C. Felser, Valence electron rules for prediction of half-metallic compensated-ferrimagnetic behaviour of Heusler compounds with complete spin polarization, *Journal of Physics: Condensed Matter* 18(27) (2006) 6171.
- [117] J. Pierre, R. Skolozdra, J. Tobola, S. Kaprzyk, C. Hordequin, M. Kouacou, I. Karla, R. Currat, E. Lelievre-Berna, Properties on request in semi-Heusler phases, *Journal of alloys and compounds* 262 (1997) 101-107.
- [118] D. Jung, H.-J. Koo, M.-H. Whangbo, Study of the 18-electron band gap and ferromagnetism in semi-Heusler compounds by non-spin-polarized electronic band structure calculations, *Journal of Molecular Structure: THEOCHEM* 527(1-3) (2000) 113-119.
- [119] W. Al-Sawai, H. Lin, R. Markiewicz, L. Wray, Y. Xia, S.-Y. Xu, M. Hasan, A. Bansil, Topological electronic structure in half-Heusler topological insulators, *Physical Review B* 82(12) (2010) 125208.
- [120] D. Xiao, Y. Yao, W. Feng, J. Wen, W. Zhu, X.-Q. Chen, G.M. Stocks, Z. Zhang, Half-Heusler compounds as a new class of three-dimensional topological insulators, *Physical review letters* 105(9) (2010) 096404.
- [121] S. Ishida, S. Fujii, S. Kashiwagi, S. Asano, Search for half-metallic compounds in  $\text{Co}_2\text{MnZ}$  ( $Z = \text{IIIb, IVb, Vb}$  element), *Journal of the Physical Society of Japan* 64(6) (1995) 2152-2157.
- [122] W.E. Pickett, J.S. Moodera, Half metallic magnets, *Physics Today* 54(5) (2001) 39-45.

- [123] M. Yoshikawa, E. Kitagawa, T. Nagase, T. Daibou, M. Nagamine, K. Nishiyama, T. Kishi, H. Yoda, Tunnel Magnetoresistance Over 100% in MgO-Based Magnetic Tunnel Junction Films With Perpendicular Magnetic L1  $\text{FePt}$  Electrodes, *IEEE Transactions on Magnetics* 44(11) (2008) 2573-2576.
- [124] K. Inomata, N. Ikeda, N. Tezuka, R. Goto, S. Sugimoto, M. Wojcik, E. Jedryka, Highly spin-polarized materials and devices for spintronics, *Science and Technology of Advanced Materials* 9(1) (2008) 014101.
- [125] T. Nakatani, N. Hase, H. Goripati, Y. Takahashi, T. Furubayashi, K. Hono, Co-based Heusler alloys for CPP-GMR spin-valves with large magnetoresistive outputs, *IEEE Transactions on Magnetics* 48(5) (2012) 1751-1757.
- [126] K. Inomata, S. Okamura, R. Goto, N. Tezuka, Large tunneling magnetoresistance at room temperature using a Heusler alloy with the B2 structure, *Japanese journal of applied physics* 42(4B) (2003) L419.
- [127] H. Kubota, J. Nakata, M. Oogane, Y. Ando, A. Sakuma, T. Miyazaki, Large magnetoresistance in magnetic tunnel junctions using Co-Mn-Al full Heusler alloy, *Japanese journal of applied physics* 43(7B) (2004) L984.
- [128] Y. Sakuraba, J. Nakata, M. Oogane, Y. Ando, H. Kato, A. Sakuma, T. Miyazaki, H. Kubota, Magnetic tunnel junctions using B2-ordered  $\text{Co}_2\text{MnAl}$  Heusler alloy epitaxial electrode, *Applied physics letters* 88(2) (2006) 022503.
- [129] S. Okamura, A. Miyazaki, S. Sugimoto, N. Tezuka, K. Inomata, Large tunnel magnetoresistance at room temperature with a  $\text{Co}_2\text{FeAl}$  full-Heusler alloy electrode, *Applied Physics Letters* 86(23) (2005) 232503.
- [130] N. Tezuka, N. Ikeda, A. Miyazaki, S. Sugimoto, M. Kikuchi, K. Inomata, Tunnel magnetoresistance for junctions with epitaxial full-Heusler  $\text{Co}_2\text{FeAl}_{0.5}\text{Si}_{0.5}$  electrodes with B2 and L21 structures, *Applied physics letters* 89(11) (2006) 112514.
- [131] D. Ebke, J. Schmalhorst, N.-N. Liu, A. Thomas, G. Reiss, A. Hütten, Large tunnel magnetoresistance in tunnel junctions with  $\text{Co}_2\text{MnSi}/\text{Co}_2\text{FeSi}$  multilayer electrode, *Applied physics letters* 89(16) (2006) 162506.
- [132] N. Hase, T. Nakatani, S. Kasai, Y. Takahashi, T. Furubayashi, K. Hono, Effect of NiAl underlayer and spacer on magnetoresistance of current-perpendicular-to-plane spin valves using  $\text{Co}_2\text{Mn}(\text{Ga}_{0.5}\text{Sn}_{0.5})$  Heusler alloy, *Journal of Magnetism and Magnetic Materials* 324(4) (2012) 440-444.



- [133] Y. Takahashi, A. Srinivasan, B. Varaprasad, A. Rajanikanth, N. Hase, T. Nakatani, S. Kasai, T. Furubayashi, K. Hono, Large magnetoresistance in current-perpendicular-to-plane pseudospin valve using a Co<sub>2</sub>Fe(Ge<sub>0.5</sub>Ga<sub>0.5</sub>) Heusler alloy, *Applied physics letters* 98(15) (2011) 152501.
- [134] T. Kubota, Y. Miura, D. Watanabe, S. Mizukami, F. Wu, H. Naganuma, X. Zhang, M. Oogane, M. Shirai, Y. Ando, Magnetoresistance effect in tunnel junctions with perpendicularly magnetized D022-Mn<sub>3</sub>- $\delta$ Ga electrode and MgO barrier, *Applied physics express* 4(4) (2011) 043002.
- [135] H. Chik, J. Xu, Nanometric superlattices: non-lithographic fabrication, materials, and prospects, *Materials Science and Engineering: R: Reports* 43(4) (2004) 103-138.
- [136] G.D. Sulka, K.G. Parkoła, Anodising potential influence on well-ordered nanostructures formed by anodisation of aluminium in sulphuric acid, *Thin Solid Films* 515(1) (2006) 338-345.
- [137] L. Zaraska, G.D. Sulka, M. Jaskuła, The effect of n-alcohols on porous anodic alumina formed by self-organized two-step anodizing of aluminum in phosphoric acid, *Surface and Coatings Technology* 204(11) (2010) 1729-1737.
- [138] K. Choudhari, P. Sudheendra, N. Udayashankar, Fabrication and high-temperature structural characterization study of porous anodic alumina membranes, *Journal of Porous Materials* 19(6) (2012) 1053-1062.
- [139] P. Chowdhury, K. Raghuvaran, M. Krishnan, H.C. Barshilia, K. Rajam, Effect of process parameters on growth rate and diameter of nano-porous alumina templates, *Bulletin of Materials Science* 34(3) (2011) 423-427.
- [140] G. Huang, X. Wu, L.W. Yang, X. Shao, G. Siu, P. Chu, Dependence of blue-emitting property on nanopore geometrical structure in Al-based porous anodic alumina membranes, *Applied Physics A* 81(7) (2005) 1345-1349.
- [141] G. Huang, X. Wu, Y. Xie, F. Kong, Z. Zhang, G. Siu, P.K. Chu, Photoluminescence from 8-hydroxy quinoline aluminum embedded in porous anodic alumina membrane, *Applied Physics Letters* 87(15) (2005) 151910.
- [142] J. Montero-Moreno, M. Sarret, C. Müller, Self-ordered porous alumina by two-step anodizing at constant current: Behaviour and evolution of the structure, *Microporous and Mesoporous Materials* 136(1-3) (2010) 68-74.

- [143] W.J. Stępniewski, Z. Bojar, Synthesis of anodic aluminum oxide (AAO) at relatively high temperatures. Study of the influence of anodization conditions on the alumina structural features, *Surface and Coatings technology* 206(2-3) (2011) 265-272.
- [144] G.D. Sulka, W.J. Stępniewski, Structural features of self-organized nanopore arrays formed by anodization of aluminum in oxalic acid at relatively high temperatures, *Electrochimica Acta* 54(14) (2009) 3683-3691.
- [145] Z.-H. Yuan, S.-Q. Sun, Y.-Q. Duan, D.-J. Wang, Fabrication of densely packed AlN nanowires by a chemical conversion of Al<sub>2</sub>O<sub>3</sub> nanowires based on porous anodic alumina film, *Nanoscale research letters* 4(10) (2009) 1126.
- [146] L. Zaraska, W.J. Stępniewski, G.D. Sulka, E. Ciepiela, M. Jaskuła, Analysis of nanopore arrangement and structural features of anodic alumina layers formed by two-step anodizing in oxalic acid using the dedicated executable software, *Applied Physics A* 114(2) (2014) 571-577.
- [147] L. Zaraska, W.J. Stępniewski, E. Ciepiela, G.D. Sulka, The effect of anodizing temperature on structural features and hexagonal arrangement of nanopores in alumina synthesized by two-step anodizing in oxalic acid, *Thin Solid Films* 534 (2013) 155-161.
- [148] E. Palibroda, Le mécanisme du développement de l'oxyde poreux de l'aluminium II. L'oxyde poreux et la tension électrique de la couche barrière, *Surface technology* 23(4) (1984) 341-351.
- [149] V. Parkhutik, V. Shershulsky, Theoretical modelling of porous oxide growth on aluminium, *Journal of Physics D: Applied Physics* 25(8) (1992) 1258.
- [150] F. Keller, MS hunter and DL Robinson, *J. electrochem. Soc* 100 (1953) 411.
- [151] K. Ebihara, Structure and density of anodic oxide films formed on aluminum in oxalic acid solutions, *Journal of The Surface Finishing Society of Japan* 34 (1983) 548-553.
- [152] P. Sheasby, S. Wernick, R. Pinner, *Surface treatment and finishing of aluminum and its alloys. Volumes 1 and 2*, (1987).
- [153] N. Yakovleva, A. Yakovlev, E. Chupakhina, Structural analysis of alumina films produced by two-step electrochemical oxidation, *Thin Solid Films* 366(1-2) (2000) 37-42.
- [154] O. Jessensky, F. Müller, U. Gösele, Self-organized formation of hexagonal pore structures in anodic alumina, *Journal of the Electrochemical Society* 145(11) (1998) 3735-3740.

- [155] J. Fernandes, R. Picciochi, M.D.C. Belo, T.M. e Silva, M. Ferreira, I. Fonseca, Capacitance and photoelectrochemical studies for the assessment of anodic oxide films on aluminium, *Electrochimica acta* 49(26) (2004) 4701-4707.
- [156] Y. Du, W. Cai, C. Mo, J. Chen, L. Zhang, X. Zhu, Preparation and photoluminescence of alumina membranes with ordered pore arrays, *Applied Physics Letters* 74(20) (1999) 2951-2953.
- [157] L. Li, AC anodization of aluminum, electrodeposition of nickel and optical property examination, *Solar energy materials and solar cells* 64(3) (2000) 279-289.
- [158] Y. Yamamoto, N. Baba, S. Tajima, Coloured materials and photoluminescence centres in anodic film on aluminium, *Nature* 289(5798) (1981) 572.
- [159] X. Zhou, G. Thompson, G. Potts, Effects of chromic acid anodizing of aluminium on adhesion and durability of bonded joints, *Transactions of the IMF* 78(6) (2000) 210-214.
- [160] K. Shimizu, K. Kobayashi, P. Skeldon, G. Thompson, G. Wood, An atomic force microscopy study of the corrosion and filming behaviour of aluminium, *Corrosion science* 39(4) (1997) 701-718.
- [161] S. Ono, M. Saito, H. Asoh, Self-ordering of anodic porous alumina formed in organic acid electrolytes, *Electrochimica Acta* 51(5) (2005) 827-833.
- [162] M. Wu, I.-C. Leu, M.-H. Hon, Effect of polishing pretreatment on the fabrication of ordered nanopore arrays on aluminum foils by anodization, *Journal of Vacuum Science & Technology B: Microelectronics and Nanometer Structures Processing, Measurement, and Phenomena* 20(3) (2002) 776-782.
- [163] K. Bordo, Nanoporous thin film templates for the fabrication of nanowires and nanotubes, Syddansk Universitet, 2011.
- [164] O. Jessensky, F. Müller, U. Gösele, Self-organized formation of hexagonal pore arrays in anodic alumina, *Applied physics letters* 72(10) (1998) 1173-1175.
- [165] Z. Su, G. Hähner, W. Zhou, Investigation of the pore formation in anodic aluminium oxide, *Journal of Materials Chemistry* 18(47) (2008) 5787-5795.
- [166] M.A. Kashi, A. Ramazani, The effect of temperature and concentration on the self-organized pore formation in anodic alumina, *Journal of Physics D: Applied Physics* 38(14) (2005) 2396.

- [167] M.A. Kashi, A. Ramazani, M. Rahmandoust, M. Noormohammadi, The effect of pH and composition of sulfuric–oxalic acid mixture on the self-ordering configuration of high porosity alumina nanohole arrays, *Journal of Physics D: Applied Physics* 40(15) (2007) 4625.
- [168] A. Belwalkar, E. Grasing, W. Van Geertruyden, Z. Huang, W. Misiolek, Effect of processing parameters on pore structure and thickness of anodic aluminum oxide (AAO) tubular membranes, *Journal of membrane science* 319(1-2) (2008) 192-198.
- [169] A. Rauf, M. Mehmood, M.A. Rasheed, M. Aslam, The effects of electropolishing on the nanochannel ordering of the porous anodic alumina prepared in oxalic acid, *Journal of Solid State Electrochemistry* 13(2) (2009) 321-332.
- [170] D. Ma, S. Li, C. Liang, Electropolishing of high-purity aluminium in perchloric acid and ethanol solutions, *Corrosion Science* 51(4) (2009) 713-718.
- [171] M. Mata-Zamora, J. Saniger, Thermal evolution of porous anodic aluminas: a comparative study, *Revista mexicana de fisica* 51(5) (2005) 502-509.
- [172] Y. Jia, H. Zhou, P. Luo, S. Luo, J. Chen, Y. Kuang, Preparation and characteristics of well-aligned macroporous films on aluminum by high voltage anodization in mixed acid, *Surface and Coatings Technology* 201(3-4) (2006) 513-518.
- [173] R.H. Rico, J.-P. Celis, B. Du Bois, C. Van Hoof, A. Witvrouw, W. Ruythooren, Alumina porous membranes obtained by one-step anodizing process in H<sub>2</sub>SO<sub>4</sub> for MEMS Packaging, *ECS Transactions* 3(9) (2006) 75-83.
- [174] G. Ding, M. Zheng, W. Xu, W. Shen, Fabrication of controllable free-standing ultrathin porous alumina membranes, *Nanotechnology* 16(8) (2005) 1285.
- [175] M.H. Wang, K.R. Hebert, An electrical model for the cathodically charged Aluminum electrode, *Journal of The Electrochemical Society* 143(9) (1996) 2827-2834.
- [176] N. Ahmad, S. Khan, W. Li, M. Saddique, S.A. Shah, J. Iqbal, A. Majid, X. Han, Potential dependent tuning of magnetic and structural properties of electrodeposited NiZn nanowires in Al<sub>2</sub>O<sub>3</sub> templates, *Journal of Magnetism and Magnetic Materials* 441 (2017) 696-701.
- [177] X. Zhao, S.-K. Seo, U.-J. Lee, K.-H. Lee, Controlled electrochemical dissolution of anodic aluminum oxide for preparation of open-through pore structures, *Journal of the Electrochemical Society* 154(10) (2007) C553-C557.
- [178] W. Xu, H. Chen, M. Zheng, G. Ding, W. Shen, Optical transmission spectra of ordered porous alumina membranes with different thicknesses and porosities, *Optical Materials* 28(10) (2006) 1160-1165.

- [179] T. Hoar, J. Yahalom, The initiation of pores in anodic oxide films formed on aluminum in acid solutions, *Journal of the Electrochemical Society* 110(6) (1963) 614-621.
- [180] J. Siejka, C. Ortega, An O18 Study of Field- Assisted Pore Formation in Compact Anodic Oxide Films on Aluminum, *Journal of The Electrochemical Society* 124(6) (1977) 883-891.
- [181] Y. Xu, G. Thompson, G. Wood, B. Bethune, Anion incorporation and migration during barrier film formation on aluminium, *Corrosion science* 27(1) (1987) 83-102.
- [182] G. Thompson, Porous anodic alumina: fabrication, characterization and applications, *Thin solid films* 297(1-2) (1997) 192-201.
- [183] G.D. Sulka, A. Brzózka, L. Liu, Fabrication of diameter-modulated and ultrathin porous nanowires in anodic aluminum oxide templates, *Electrochimica Acta* 56(14) (2011) 4972-4979.
- [184] L. Vivas, Y.P. Ivanov, D. Trabada, M. Proenca, O. Chubykalo-Fesenko, M. Vázquez, Magnetic properties of Co nanopillar arrays prepared from alumina templates, *Nanotechnology* 24(10) (2013) 105703.
- [185] G.E. Possin, A method for forming very small diameter wires, *Review of Scientific Instruments* 41(5) (1970) 772-774.
- [186] I. Žutić, I. Žutić, J. Fabian, and S. Das Sarma, *Rev. Mod. Phys.* 76, 323 (2004), *Rev. Mod. Phys.* 76 (2004) 323.
- [187] A. Hirohata, K. Takanashi, Future perspectives for spintronic devices, *Journal of Physics D: Applied Physics* 47(19) (2014) 193001.
- [188] C. Felser, B. Heitkamp, F. Kronast, D. Schmitz, S. Cramm, H. Dürr, H. Elmers, G. Fecher, S. Wurmehl, T. Block, Investigation of a novel material for magnetoelectronics:  $\text{Co}_2\text{Cr}_0.6\text{Fe}_0.4\text{Al}$ , *Journal of Physics: Condensed Matter* 15(41) (2003) 7019.
- [189] R. De Groot, RA de Groot, FM Mueller, PG van Engen, and KHJ Buschow, *Phys. Rev. Lett.* 50, 2024 (1983), *Phys. Rev. Lett.* 50 (1983) 2024.
- [190] L. Berger, Emission of spin waves by a magnetic multilayer traversed by a current, *Physical Review B* 54(13) (1996) 9353.
- [191] J.C. Slonczewski, Current-driven excitation of magnetic multilayers, *Journal of Magnetism and Magnetic Materials* 159(1-2) (1996) L1-L7.

- [192] A.L. Kwilu, M. Oogane, H. Naganuma, M. Sahashi, Y. Ando, Intrinsic Gilbert damping constant in epitaxial  $\text{Co}_2\text{Fe}_{0.4}\text{Mn}_{0.6}\text{Si}$  Heusler alloys films, *Journal of Applied Physics* 117(17) (2015) 17D140.
- [193] H. Huang, X. Ma, Z. Liu, C. Zhao, L. Chen, Micromagnetic simulation of high-power spin-torque oscillator in half-metallic Heusler alloy spin valve nanopillar, *AIP Advances* 3(3) (2013) 032132.
- [194] T. Block, C. Felser, G. Jakob, J. Enslin, B. Mühlhng, P. Gütlich, R. Cava, Large negative magnetoresistance effects in  $\text{Co}_2\text{Cr}_{0.6}\text{Fe}_{0.4}\text{Al}$ , *Journal of Solid State Chemistry* 176(2) (2003) 646-651.
- [195] N. Ahmad, M. Awais, S.A. Shah, I. Ahmed, N. Jabeen, A. Majid, J. Iqbal, Influence of voltage variation on structure and magnetic properties of  $\text{Co}_{1-x}\text{Sn}_x$  ( $X=0.3-0.7$ ) nanowire alloys in alumina by electrochemical deposition, *Applied Physics A* 123(1) (2017) 65.
- [196] M. Law, L. Greene, J. Johnson, R. Saykally, P. Yang, *Nature Mater.* 4, 455 (2005), 2006.
- [197] P. Blaha, K. Schwarz, G.K. Madsen, D. Kvasnicka, J. Luitz, wien2k, An augmented plane wave+ local orbitals program for calculating crystal properties (2001).
- [198] J.P. Perdew, JP Perdew and Y. Wang, *Phys. Rev. B* 45, 13244 (1992), *Phys. Rev. B* 45 (1992) 13244.
- [199] N. Ahmed, J. Nisar, R. Kouser, A.G. Nabi, S. Mukhtar, Y. Saeed, M. Nasim, Study of electronic, magnetic and optical properties of  $\text{KMS}_2$  ( $M= \text{Nd, Ho, Er and Lu}$ ): first principle calculations, *Materials Research Express* 4(6) (2017) 065903.
- [200] K. Özdoğan, B. Aktaş, I. Galanakis, E. Şaşıoğlu, Influence of mixing the low-valent transition metal atoms ( $Y, Y^*= \text{Cr, Mn, Fe}$ ) on the properties of the quaternary  $\text{Co}_2[\text{Y}_{1-x}\text{Y}^*_x]\text{Z}$  ( $Z= \text{Al, Ga, Si, Ge, or Sn}$ ) Heusler compounds, *Journal of Applied Physics* 101(7) (2007) 073910.
- [201] J. De Boeck, W. Van Roy, V. Motsnyi, Z. Liu, K. Dessein, G. Borghs, Hybrid epitaxial structures for spintronics, *Thin Solid Films* 412(1-2) (2002) 3-13.
- [202] I. Galanakis, Orbital magnetism in the half-metallic Heusler alloys, *Physical Review B* 71(1) (2005) 012413.
- [203] I. Galanakis, I. Galanakis, PH Dederichs, and N. Papanikolaou, *Phys. Rev. B* 66, 174429 (2002), *Phys. Rev. B* 66 (2002) 174429.

- [204] S. Gao, Y. Liu, X. Kou, Effect of electrolyte pH and deposition time on the microstructure and magnetic properties of electrodeposited Fe<sub>2</sub>CoSn Heusler alloy, *International Journal of Electrochemical Science* 10 (2015) 8727-8737.
- [205] A. Ayuela, J. Enkovaara, K. Ullakko, R. Nieminen, Structural properties of magnetic Heusler alloys, *Journal of Physics: Condensed Matter* 11(8) (1999) 2017.
- [206] T. Gasi, A.K. Nayak, M. Nicklas, C. Felser, Structural and magnetic properties of the Heusler compound Fe<sub>2</sub>MnGa, *Journal of Applied Physics* 113(17) (2013) 17E301.
- [207] M. Zhang, E. Brück, F.R. de Boer, G. Wu, Electronic structure, magnetism, and transport properties of the Heusler alloy Fe<sub>2</sub>CrAl, *Journal of magnetism and magnetic materials* 283(2-3) (2004) 409-414.
- [208] R. Vivas, S. Pedro, C. Cruz, J. Tedesco, A. Coelho, A.M.G. Carvalho, D. Rocco, M. Reis, Multifunctional Heusler alloy: experimental evidences of enhanced magnetocaloric properties at room temperature and half-metallicity, *arXiv preprint arXiv:1508.01828* (2015).
- [209] L. Tian, J. Xu, S. Xiao, The influence of pH and bath composition on the properties of Ni-Co coatings synthesized by electrodeposition, *Vacuum* 86(1) (2011) 27-33.
- [210] C. Li, Q. Wu, M. Yue, H. Xu, S. Palaka, K. Elkins, J. Ping Liu, Manipulation of morphology and magnetic properties in cobalt nanowires, *AIP Advances* 7(5) (2017) 056229.
- [211] C. Chisholm, E. Kuzmann, S. Stichleitner, Z. Homonnay, A. Vertes, Electrodeposition of Sn-Fe alloys using gluconate electrolytes and X-ray diffractometry and Mössbauer studies of the deposits, *Materials Chemistry and Physics* 120(2-3) (2010) 558-565.
- [212] C.-C. Chen, Y. Bisrat, Z. Luo, R. Schaak, C. Chao, D. Lagoudas, Fabrication of single-crystal tin nanowires by hydraulic pressure injection, *Nanotechnology* 17(2) (2005) 367.
- [213] C. Sousa, D. Leitao, M. Proenca, J. Ventura, A. Pereira, J. Araujo, Nanoporous alumina as templates for multifunctional applications, *Applied Physics Reviews* 1(3) (2014) 031102.
- [214] B. Malaman, G. Le Caër, B. Costa, B2 long-range order in mechanically alloyed Fe<sub>53.3-0.6x</sub>Co<sub>46.7-0.4x</sub>Sn<sub>x</sub> (2 ≤ x ≤ 26) annealed at moderate temperatures, *Journal of Materials Science* 51(12) (2016) 5775-5790.
- [215] Y. Takamura, T. Sakurai, R. Nakane, Y. Shuto, S. Sugahara, Epitaxial germanidation of full-Heusler Co<sub>2</sub>FeGe alloy thin films formed by rapid thermal annealing, *Journal of Applied Physics* 109(7) (2011) 07B768.

- [216] J. Duan, X. Kou, Effect of current density on the microstructure and magnetic properties of electrodeposited Co<sub>2</sub>FeSn Heusler alloy, *Journal of The Electrochemical Society* 160(10) (2013) D471-D475.
- [217] L. Liu, H. Li, S. Fan, J. Gu, Y. Li, H. Sun, Fabrication and magnetic properties of Ni–Zn nanowire arrays, *Journal of Magnetism and Magnetic Materials* 321(20) (2009) 3511-3514.
- [218] U. Chaitra, D. Kekuda, K.M. Rao, Dependence of solution molarity on structural, optical and electrical properties of spin coated ZnO thin films, *Journal of Materials Science: Materials in Electronics* 27(7) (2016) 7614-7621.
- [219] J. González, P. Fernandes, G. Ribeiro, A. Abelenda, E. Viana, P. Salomé, A. Da Cunha, Influence of the sulphurization time on the morphological, chemical, structural and electrical properties of Cu<sub>2</sub>ZnSnS<sub>4</sub> polycrystalline thin films, *Solar Energy Materials and Solar Cells* 123 (2014) 58-64.
- [220] K. Buschow, P. Van Engen, Magnetic and magneto-optical properties of Heusler alloys based on aluminium and gallium, *Journal of Magnetism and Magnetic Materials* 25(1) (1981) 90-96.
- [221] J. Moodera, X. Hao, G. Gibson, R. Meservey, Electron-spin polarization in tunnel junctions in zero applied field with ferromagnetic EuS barriers, *Physical review letters* 61(5) (1988) 637.
- [222] Q. Cai, J. Zhang, X. Chen, Z. Chen, W. Wang, G. Mo, Z. Wu, L. Zhang, W. Pan, Structural study on Ni nanowires in an anodic alumina membrane by using in situ heating extended x-ray absorption fine structure and x-ray diffraction techniques, *Journal of Physics: Condensed Matter* 20(11) (2008) 115205.
- [223] K.S. Leschkies, R. Divakar, J. Basu, E. Enache-Pommer, J.E. Boercker, C.B. Carter, U.R. Kortshagen, D.J. Norris, E.S. Aydil, Photosensitization of ZnO nanowires with CdSe quantum dots for photovoltaic devices, *Nano letters* 7(6) (2007) 1793-1798.
- [224] M. Czerner, B.Y. Yavorsky, I. Mertig, Fully relaxed magnetic structure of transition metal nanowires: First-principles calculations, *Physical Review B* 77(10) (2008) 104411.
- [225] B. Camacho-Flores, O. Martínez-Álvarez, M. Arenas-Arrocena, R. Garcia-Contreras, L. Argueta-Figueroa, J. De La Fuente-Hernández, L. Acosta-Torres, Copper: synthesis techniques in nanoscale and powerful application as an antimicrobial agent, *Journal of Nanomaterials* 16(1) (2015) 423.



- [226] K. Nielsch, R. Wehrspohn, J. Barthel, J. Kirschner, U. Gösele, S. Fischer, H. Kronmüller, Hexagonally ordered 100 nm period nickel nanowire arrays, *Applied Physics Letters* 79(9) (2001) 1360-1362.
- [227] L. Piraux, J. George, J. Despres, C. Leroy, E. Ferain, R. Legras, K. Ounadjela, A. Fert, Giant magnetoresistance in magnetic multilayered nanowires, *Applied Physics Letters* 65(19) (1994) 2484-2486.
- [228] A. Blondel, J.P. Meier, B. Doudin, J.P. Ansermet, Giant magnetoresistance of nanowires of multilayers, *Applied Physics Letters* 65(23) (1994) 3019-3021.
- [229] M. Tanase, D. Silevitch, A. Hultgren, L. Bauer, P. Searson, G. Meyer, D. Reich, Magnetic trapping and self-assembly of multicomponent nanowires, *Journal of applied physics* 91(10) (2002) 8549-8551.
- [230] J. Sun, M. He, X. Liu, N. Gu, Optimizing colloidal dispersity of magnetic nanoparticles based on magnetic separation with magnetic nanowires array, *Applied Physics A* 118(2) (2015) 569-577.
- [231] H. Xu, D.-H. Qin, Z. Yang, H.-L. Li, Fabrication and characterization of highly ordered zirconia nanowire arrays by sol-gel template method, *Materials chemistry and physics* 80(2) (2003) 524-528.
- [232] A. Huczko, Template-based synthesis of nanomaterials, *Applied Physics A* 70(4) (2000) 365-376.
- [233] S. Shingubara, Fabrication of nanomaterials using porous alumina templates, *Journal of Nanoparticle Research* 5(1-2) (2003) 17-30.
- [234] T. Whitney, P. Searson, J. Jiang, C. Chien, Fabrication and magnetic properties of arrays of metallic nanowires, *Science* 261(5126) (1993) 1316-1319.
- [235] D. Sellmyer, M. Zheng, R. Skomski, Magnetism of Fe, Co and Ni nanowires in self-assembled arrays, *Journal of Physics: Condensed Matter* 13(25) (2001) R433.
- [236] H. Khan, K. Petrikowski, Magnetic and structural properties of the electrochemically deposited arrays of Co and CoFe nanowires, *Journal of Magnetism and Magnetic Materials* 249(3) (2002) 458-461.
- [237] X. Zhang, G. Wen, Y. Chan, R. Zheng, X. Zhang, N. Wang, Fabrication and magnetic properties of ultrathin Fe nanowire arrays, *Applied physics letters* 83(16) (2003) 3341-3343.

- [238] M. Ananth, N. Parthasarathy, Influence of plating variables on the electrocatalytic behavior of Ni-Mn electrocoated cathodes for alkaline water electrolysis, *Bulletin of Electrochemistry* 6(01) (1990) 40-41.
- [239] S. Anitha, I. Jayakumari, Synthesis and Analysis of Nanocrystalline Fe<sub>2</sub>Mn<sub>2</sub>Ni<sub>0.5</sub>Zn<sub>1.5</sub>O<sub>9</sub> at Different Treating Temperatures, *Journal of Nanoscience and Technology* (2015) 26-31.
- [240] K. Maleki, S. Sanjabi, Z. Alemipour, DC electrodeposition of NiGa alloy nanowires in AAO template, *Journal of Magnetism and Magnetic Materials* 395 (2015) 289-293.
- [241] C. Wayman, On memory effects related to martensitic transformations and observations in  $\beta$ -brass and Fe<sub>3</sub>Pt, *Scripta Metallurgica* 5(6) (1971) 489-492.
- [242] T. Jurgeleit, L. Jessen, E. Quandt, C. Zamponi, Magnetron-Sputtered, Biodegradable FeMn Foils: The Influence of Manganese Content on Microstructure, Mechanical, Corrosion, and Magnetic Properties, *Materials* 11(4) (2018) 482.
- [243] M. Formentini, S. Lenci, An innovative building envelope (kinetic façade) with Shape Memory Alloys used as actuators and sensors, *Automation in Construction* 85 (2018) 220-231.
- [244] J. Franken, H. Swagten, B. Koopmans, Shift registers based on magnetic domain wall ratchets with perpendicular anisotropy, *Nature nanotechnology* 7(8) (2012) 499.
- [245] B. Dieny, V.S. Speriosu, S.S. Parkin, B.A. Gurney, D.R. Wilhoit, D. Mauri, Giant magnetoresistive in soft ferromagnetic multilayers, *Physical Review B* 43(1) (1991) 1297.
- [246] B. Balamurugan, D.J. Sellmyer, G.C. Hadjipanayis, R. Skomski, Prospects for nanoparticle-based permanent magnets, *Scripta Materialia* 67(6) (2012) 542-547.
- [247] C. Feng, B.-H. Li, J. Teng, Y. Jiang, G.-H. Yu, Influence of antiferromagnetic FeMn on magnetic properties of perpendicular magnetic thin films, *Thin Solid Films* 517(8) (2009) 2745-2748.
- [248] J. Emsley, *The elements*, Clarendon Press ; Oxford University Press, Oxford; New York, 1998.
- [249] C.L. Keen, J.L. Ensunsa, M.S. Clegg, Manganese metabolism in animals and humans including the toxicity of manganese, *Metal ions in biological systems*, CRC Press 2000, pp. 137-170.
- [250] D. McGregor, R. Baan, C. Partensky, J. Rice, J. Wilbourn, Evaluation of the carcinogenic risks to humans associated with surgical implants and other foreign bodies—a report of an IARC Monographs Programme Meeting, *European journal of cancer* 36(3) (2000) 307-313.

- [251] M. Aschner, T.R. Guilarte, J.S. Schneider, W. Zheng, Manganese: recent advances in understanding its transport and neurotoxicity, *Toxicology and applied pharmacology* 221(2) (2007) 131-147.
- [252] R.A. Cloyd, S.A. Koren, J.F. Abisambra, Manganese-Enhanced Magnetic Resonance Imaging: Overview and Central Nervous System Applications With a Focus on Neurodegeneration, *Frontiers in aging neuroscience* 10 (2018).
- [253] J. Crossgrove, W. Zheng, Manganese toxicity upon overexposure, *NMR in Biomedicine: An International Journal Devoted to the Development and Application of Magnetic Resonance In Vivo* 17(8) (2004) 544-553.
- [254] D.L. Fischman, M.B. Leon, D.S. Baim, R.A. Schatz, M.P. Savage, I. Penn, K. Detre, L. Veltri, D. Ricci, M. Nobuyoshi, A randomized comparison of coronary-stent placement and balloon angioplasty in the treatment of coronary artery disease, *New England Journal of Medicine* 331(8) (1994) 496-501.
- [255] P.W. Serruys, P. De Jaegere, F. Kiemeneij, C. Macaya, W. Rutsch, G. Heyndrickx, H. Emanuelsson, J. Marco, V. Legrand, P. Materne, A comparison of balloon-expandable-stent implantation with balloon angioplasty in patients with coronary artery disease, *New England Journal of Medicine* 331(8) (1994) 489-495.
- [256] H. Hermawan, A. Purnama, D. Dube, J. Couet, D. Mantovani, Fe–Mn alloys for metallic biodegradable stents: degradation and cell viability studies, *Acta biomaterialia* 6(5) (2010) 1852-1860.
- [257] K. Attenborough, H. Boeve, J. De Boeck, G. Borghs, J.-P. Celis, Electrodeposited spin valves on n-type GaAs, *Applied physics letters* 74(15) (1999) 2206-2208.
- [258] H. Yu, S. Granville, D. Yu, J.-P. Ansermet, Evidence for thermal spin-transfer torque, *Physical review letters* 104(14) (2010) 146601.

## Turnitin Originality Report

Thesis by **Suleman Khan**

From FinalThesis (Repository)



- Processed on 02-Apr-2019 14:13 PKT
- ID: 1104391289
- Word Count: 30710

## Similarity Index

11%

## Similarity by Source

## Internet Sources:

4%

## Publications:

8%

## Student Papers:

3%

## sources:

- 1% match (publications)  
Ladislav Galoun, Victor Vega, Zuzana Vargova, Enrique D. Barrio-Castro, Carlos Luna Rastislav Varga, Victor M. Prida. "Intermetallic Co-Fe-In Heusler Alloy Nanowires for Spintronic Applications." *ACS Applied Nano Materials*. 2018
- 1% match (student papers from 22-Feb-2016)  
Class: Repository  
Assignment: FinalThesis  
Paper ID: 635192474
- 1% match (publications)  
Naseem Ishaq, Suleman Khan, M. I. U. Mubhammad, Santanu, Santanu A. Ghosh, Javed Ishaq  
~~https://doi.org/10.1039/C8NR00002A~~ ~~https://doi.org/10.1039/C8NR00002A~~  
*Materials*. 2018
- 1% match (Internet from 27-Sep-2016)  
[https://issuu.com/dagudocs/nan\\_0470033517](https://issuu.com/dagudocs/nan_0470033517)
- 1% match (publications)  
K. Matek, S. Sanjabi, Z. Alemraj, "DC electrocrystallization of NiCo alloy nanowires in AAC mode." *Journal of Materials: The Malaysian Materials*. 2016
- < 1% match (publications)  
Grzegorz D. Sulka. "Highly Ordered Anodic Porous Alumina Formation by Self-Organized Anodizing." *Nanostructured Materials in Electrochemistry*. 02/02/2008
- < 1% match (student papers from 22-Jan-2015)
- < 1% match (publications)  
Chenglin Li, Qiong Wu, Ming Yue, Huanhuan Xu, Subhashini Palaka, Kevin Ekins, J. Ping Liu  
"Manipulation of morphology and magnetic properties in cobalt nanowires." *AP Advances*  
2017
- < 1% match (publications)  
*Handbook of Spintronics*. 2016.
- < 1% match (publications)
- < 1% match (publications)  
K. Benkacour, A. Chaher, A. Amar, H. Rozale, A. Laketa, O. Benhelal, A. Sayane. "First-principles study of structural, elastic, thermodynamic, electronic and magnetic properties for the quaternary Heusler alloys CoRuFeZrZr = Sn, Ge, Sn." *Journal of Alloys and Compounds*. 2016
- < 1% match (publications)